Medicine Authentication using Nuclear Quadrulope Resonance

Kyriakidou, Georgia

Awarding institution:
King's College London

MEDICINES AUTHENTICATION USING NUCLEAR QUADRUPOLE RESONANCE

A thesis submitted to the King's College London
for the degree of Doctor of Philosophy
in the Faculty of Natural and Mathematical Sciences

2016

By
Georgia Kyriakidou
Department of Informatics

Abstract

Nuclear Quadrupole Resonance (NQR) is a radio-frequency (RF) spectroscopic technique, that allows the detection of solid-state compounds containing quadrupolar nuclei; a property of the majority of pharmaceutical products. This thesis investigates the application of NQR in medicines authentication, where accurate "fingerprints" of the examined materials must be obtained, in response to the global threat of low quality and counterfeit medicines. In practice, a complete NQR system contains a database with profiles of commercial medicines, built using characteristic features of the NQR signals. However, several issues including the weak NQR signals, prolonged measurement times and the evident variability among medicines can influence the accuracy of the profiles and limit the current use of NQR in the field. The expected signal amplitude is often affected by the uncertainty regarding the compound's temperature, which may cause the signal-to-noise ratio (SNR) to be substantially reduced; this phenomenon is commonly known as *off-resonance* effects. An extended echo-train signal data model is introduced, which exploits the dependence of the signal amplitude on the off-resonance excitation frequency and temperature. Herein, the Cramér-Rao lower bound, able to efficiently determine conditions for optimised detection, is derived. The stability and degradation of medicines is influenced by several factors. Being able to determine the variability between medicines produced by the same manufacturer is crucial in medicines authentication. Herein, the investigation of batch-to-batch variability of analgesic paracetamol of the same producer is presented, with the findings pointing out the need for long term monitoring of a product's "fingerprint". Last, a study is presented that focuses on versatile methodologies which can reduce the measurement times by identifying limits in the accuracy of the estimation parameters. The results indicate that these proposed solutions can help optimising the utility of the applied signal processing method.

Contents

Abstract **1**

Declaration **11**

Acknowledgements **12**

Dedication **14**

Acronyms **15**

Notational Conventions **17**

1 Introduction **18**
1.1 NQR spectroscopy 19
1.2 Challenges in NQR 21
1.3 The threat of counterfeit medicines 23
1.4 NQR in medicines authentication 24
1.5 Challenges of NQR in medicines authentication 27
1.6 Thesis Outline and Contributions 29

2 Background Theory **32**
2.1 Principles of Nuclear Magnetic Resonance 32
2.2 Quadrupolar Moment 35
2.2.1 Hamiltonian of the Quadrupole Interaction 36
2.3 Spin-1: Energy Levels and Resonance Frequencies 37
2.4 Radio Frequency Excitation 40
2.4.1 Rotating Frame of Reference 41
2.4.2 Flip Angle 42
2.5 Nuclear Relaxation 45

2.6 NQR Signals . . . 48
2.6.1 Hahn Echo . . . 48
2.6.2 Pulsed Spin-Lock Sequence . . . 49
2.7 NQR characteristic parameters . . . 52
2.7.1 Temperature Effects . . . 53
2.7.2 Off-resonance excitation . . . 55
2.8 Overview of Advanced Signal Processing in NQR . . . 56
2.8.1 Signal Models . . . 56
2.8.2 Detection algorithms . . . 58

3 Experimental **61**
3.1 Outline of the NQR hardware . . . 61
3.1.1 Transmitter Part . . . 61
3.1.2 Receiver Part . . . 63
3.1.3 Quality Factor . . . 64
3.2 Temperature Monitoring . . . 65
3.3 Experimental Equipment . . . 68

4 Exploiting Off-resonance Effects **70**
4.1 Introduction . . . 70
4.2 NQR data model . . . 72
4.3 The ODETAML Detector . . . 77
4.3.1 Frequency Selective ODETAML . . . 79
4.4 Cramér Rao Lower Bound . . . 81
4.5 Experimental Procedure . . . 83
4.5.1 Sodium Nitrite . . . 84
4.5.2 Metformin Hydrochloride . . . 85
4.5.3 Aniracetam . . . 88
4.6 Numerical Results . . . 89
4.7 Conclusions . . . 100

5 Discrimination of Paracetamol Batches **103**
5.1 Introduction . . . 103
5.2 Experimental Procedure . . . 106
5.2.1 NQR . . . 106
5.2.2 X-ray Diffraction . . . 109

5.3 Results . . . 109
5.3.1 NQR – Hypothesis: Within batches variability . . . 109
5.3.2 NQR – Hypothesis: Between batches variability . . . 114
5.3.3 X-ray Diffraction Results . . . 120
5.4 Conclusion . . . 121

6 Optimising data processing **124**
6.1 Introduction . . . 124
6.2 Sinusoidal damping constant and acquisition time . . . 128
6.2.1 Experimental Procedure . . . 128
6.2.2 Results and Discussion . . . 129
6.3 Echo damping constant and number of echoes . . . 132
6.3.1 Experimental Procedure . . . 132
6.3.2 Results and Discussion . . . 133
6.4 Conclusions . . . 137

7 Conclusions **140**
7.1 Summary and Future Work . . . 142

Collaborative Related Work: Publications **147**

A Cramér-Rao Lower Bound **172**

B Multivariate Analysis of Variance **174**

C Powder X-ray Diffraction **177**

List of Tables

4.1 The temperature shifting function constants for the NQR transition lines of sodium nitrite. 84
4.2 PSL experimental parameters – Sodium nitrite. 86
4.3 ^{14}N NQR frequencies, asymmetry parameters and quadrupole coupling constants of metformin hydrochloride (T = 295 K). 86
4.4 Spin lattice relaxation constant for the ν_+ transition lines (T = 295 K). 86
4.5 The temperature shifting function constants for the ν_+ NQR transition lines. 87
4.6 PSL experimental parameters – Metformin hydrochloride. 87
4.7 ^{14}N NQR frequencies, asymmetry parameter and quadrupole coupling constant of aniracetam (T = 283 K). 88
4.8 PSL experimental parameters – Aniracetam. 91

5.1 PSL experimental parameters 108
5.2 MANOVA: within batches comparison. 113
5.3 MANOVA: between batches comparison. 115
5.4 Univariate ANOVAs: between batches comparison – Wilks's λ. . . 115
5.5 Tukey's Post-Hoc Test for the β variable. 116
5.6 Tukey's Post-Hoc Test for the η variable. 117
5.7 Tukey's Post-Hoc Test for the ρ variable. 117

6.1 PSL experimental parameters. 129
6.2 PSL experimental parameters for all the examined materials (T = 297 K). 134
6.3 The echo damping constant estimates for each of the examined material. 136

List of Figures

1.1 ^{14}N NQR signal lineshape of powder paracetamol of two different manufacturers ($\nu = 2.563$ MHz, T= 295 K); Galpharm and Panadol. 26
1.2 Simple block diagram of NQR in a medicines authentication application. 27

2.1 Quantum energy levels for nuclear spin $I = \frac{1}{2}$ (left) and $I = \frac{3}{2}$ (right) in a magnetic field B_0. 33
2.2 Nuclear electric quadrupole moment. 36
2.3 Quadrupole energy levels and transitions for nuclear spin $I = 1$. . 40
2.4 Precession of magnetic dipole moment $\boldsymbol{\mu}$ about the $+z$ direction of $\mathbf{B}_0$ field. 41
2.5 The rotating frame of reference. 42
2.6 Flip angle. 43
2.7 Free Induction Decay. 45
2.8 Measurement of T_1 relaxation constant using the Inversion-recovery pulse sequence. 46
2.9 Formation of the Hahn Echo. 48
2.10 The NQR signal formed using a PSL sequence. 50

3.1 Block diagram of the standard NQR hardware. 62
3.2 Matching and tuning circuitry. 63
3.3 (a) Infrared temperature sensor and (b) diagram of pin (top view) description of the MLX90614 sensor. 67
3.4 Temperature measurements from the IR MLX90614 sensor. 67
3.5 NQR laboratory at King's College London. 69
3.6 Fixed pitch cylindrical solenoid. 69

4.1 Theoretical amplitude (4.9) as a function of the off-resonance frequency, $\Delta\omega = 2\pi\Delta\nu$, for the 3.5 MHz NQR spectral line of sodium nitrite. 76
4.2 The molecular structure of sodium nitrite. 84
4.3 Resonance frequency versus temperature for the ν_+, ν_- and ν_0 NQR spectral lines of powder sodium nitrite; linear fit using $\omega = a - bT$ ($\omega = 2\pi\nu$). 85
4.4 The molecular structure of metformin hydrochloride. 85
4.5 Resonance frequency versus temperature for the $\nu+$ NQR spectral lines of metformin hydrochloride; linear fit using $\omega = a - bT$ ($\omega = 2\pi\nu$). 87
4.6 Fourier transformed NQR signal from metformin hydrochloride caplets. 88
4.7 The molecular structure of aniracetam. 89
4.8 Resonance frequency versus temperature for the $\nu+$ NQR spectral line of aniracetam; linear fit using $\omega = a - bT$ ($\omega = 2\pi\nu$) where $a = 2.564$ MHz and $b = 0.040$ kHz/K. 90
4.9 Fourier transformed signal of powdered aniracetam. 90
4.10 Comparison of the theoretical and experimental NQR signal intensities of sodium nitrite ($\nu_- = 3615$ kHz), as a function of the off-resonance excitation frequency; periodicity $1/t_c = 1.171$ kHz. 92
4.11 Comparison of the theoretical and experimental NQR signal intensities of metformin hydrochloride, as a function of the off-resonance excitation frequency; periodicity $1/t_c = 0.906$ kHz; (a) $\nu_{+1} = 2834$ kHz and (b) $\nu_{+2} = 2821$ kHz. 92
4.12 Comparison of the theoretical and experimental NQR signal intensities of aniracetam ($\nu_+ = 2553.1$ kHz), as a function of the off-resonance excitation frequency; periodicity $1/t_c = 0.804$ kHz. . 93
4.13 Comparison of experimental and theoretical NQR signal intensities, for sodium nitrite, as a function of the off-resonance excitation frequency, $\Delta\nu$, for a range of echo spacings (2τ). 94
4.14 The NRMSE obtained by the ODFETAML algorithm, compared with the respective CRLB for the T, β, η and ρ parameters when $\Delta\nu = 0$ Hz; evaluation over $P = 1500$ Monte Carlo simulations. . 96

4.15 The NRMSE obtained by the ODFETAML algorithm, compared with the respective CRLB for the T, β, η and ρ parameters when $\Delta\nu = 1.7$ kHz; evaluation over $P = 1500$ Monte Carlo simulations. 97
4.16 The NRMSE obtained by the ODFETAML algorthm, compared with the respective CRLB, for the T, β, η and ρ parameters when $\Delta\nu = 2.2$ kHz; evaluation over $P = 1500$ Monte Carlo simulations. 98
4.17 Estimation accuracy (99%) as determined using the CRLB of the signal intensities at various temperature uncertainties (ΔT). Comparison of the theoretical bounds and measurements for ν_- = 3615 kHz frequency line of sodium nitrite. 100
4.18 Estimation accuracy (99%) as determined using the CRLB of the signal intensities at various temperature uncertainties (ΔT). Comparison of the theoretical bounds and measurements for (a) ν_{+1} = 2834 kHz and (b) ν_{+2} = 2821 kHz frequency lines of metformin hydrochloride. 101
4.19 Estimation accuracy (99%) as determined using the CRLB of the signal intensities at various temperature uncertainties (ΔT). Comparison of the theoretical bounds and measurements for ν_+ = 2553.1 kHz frequency line of aniracetam. 101

5.1 The molecular structure of paracetamol (acetaminophen). 106
5.2 (a) Packs of analgesic paracetamol tablets; (b) Setup of one batch of paracetamol tablets within the coil. 107
5.3 Resonance frequency versus temperature for the $\nu+$ NQR spectral line of analgesic paracetamol tablets; linear fit using $\omega = a - bT$ ($\omega = 2\pi\nu$). 108
5.4 Mean values of (a) β, (b) η , (c) ρ with respect to samples for the batch September 2014. Error bars represent $\pm$ the standard deviations. 111
5.5 Mean values of (a) β, (b) η , (c) ρ with respect to samples for the batch August 2016. Error bars represent $\pm$ the standard deviations. 111
5.6 Mean values of (a) β, (b) η , (c) ρ with respect to samples for the batch April 2015. Error bars represent $\pm$ the standard deviations. 112
5.7 Mean values of (a) β, (b) η , (c) ρ with respect to samples for the batch August 2014. Error bars represent $\pm$ the standard deviations. 112

5.8 Mean values of (a) β, (b) η , (c) ρ with respect to samples for the batch July 2014. Error bars represent ± the standard deviations. 112
5.9 Mean values of (a) β, (b) η , (c) ρ with respect to samples for the batch October 2014. Error bars represent ± the standard deviations. 113
5.10 Mean values of (a) β, (b) η , (c) ρ with respect to six batches; (1) September 2014, (2) August 2016, (3) April 2015, (4) August 2014, (5) July 2014 and (6) October 2014. Error bars represent ± the standard deviations. 114
5.11 Scatter plot of β with respect to η dependent variable for the six different batches of paracetamol, with their corresponding marginal histograms. 115
5.12 Pairwise combinations versus mean differences for (a) β, (b) η and (c) ρ parameters, obtained from the Tukey's post hoc test. 118
5.13 Absolute age difference versus the associated absolute β deviations from the reference/newest batch (red crosses). For illustration purposes, a possible exponential fit is shown (blue curve). 119
5.14 Scatter plot of β vs η variables for two batches (Sep 2014 and Oct 2014), along with their corresponding CRLB ellipses for two values of S/Ns. 120
5.15 Powder X-ray diffraction patterns. 122

6.1 Simple block diagram emphasising the basic steps in medicines authentication using NQR. 125
6.2 NQR lineshapes of paracetamol (a) caplets (T_2^*=0.164 ms) and (b) capsules (T_2^*=0.510 ms) of the same brand (Panadol); 2τ = 2286 µs and acquisition time = 1536 µs. 129
6.3 T_2^* estimates with respect to the acquisition time, for both paracetamol caplets and capsules. 130
6.4 Coefficient of variation versus acquisition time for paracetamol caplets, of the sinusoidal damping constant (β) estimates; for caplets, T_2^* = 0.164 ms. 131
6.5 Coefficient of variation versus acquisition time for paracetamol capsules, of the sinusoidal damping constant (β) estimates; for capsules, T_2^* = 0.510 ms. 131
6.6 The molecular structure of ampicillin (trihydrate). 133
6.7 The molecular structure of sulfadiazine. 133

6.8 The time domain echo trains obtained from five different samples. 135
6.9 Simple illustration of merging the adjacent echoes within an echo train; in every iteration, N doubles are merged with $2\tau' = N \times 2\tau$ and $M' = M/N$ changing correspondingly. 136
6.10 The echo damping estimates versus the number of echoes (M') within the echo train, with the tolerance levels of $\pm 1\%$ and $\pm 2\%$. 139

7.1 The estimated echo damping parameter versus the off-resonance excitation frequency, for the $\nu = 3.615$ MHz spectral line of powder sodium nitrite (283 K); $t_{\mathrm{pw}} = 40$ µs, $2\tau = 418$ µs. 143
R.1 The rectangular cross section RF coils; left: fixed, middle: variable based on Leifer equations and right: optimised variable pitch coils. 148
R.2 Mean echo signal intensity versus number of analgesic paracetamol pills; (a) fixed and (b) variable pitch coils. 149
R.3 ^{14}N NQR spectra of genuine (red/higher peaks) and suspect counterfeit (green/lower peaks) of antimalarial medicine Metakelfin. . . 150

C.1 Simple diagram of the constructive interference of an X-ray scattered from two planes. 178

Declaration

No portion of the work referred to in this thesis has been submitted in support of an application for another degree or qualification of this or any other university or other institute of learning.

Acknowledgements

"Keep Ithaka always in your mind. Arriving there is what you are destined for. But do not hurry the journey at all."

Constantinos C. Cavafy, Poet

I have finished and am elated. But unlike God, I didn't do it alone. Before I rest, I would like to thank several people who have helped me get here sanely.

I would like to give special thanks, beginning with Prof. Kaspar Althoefer who provided me with this opportunity, trusted me in undertaking my chosen path, and also truly thank him for constantly motivating me.

My deepest gratitude goes to Prof. Andreas Jakobsson; his exceptional guidance, understanding, caring and concern, made me feel I did not only have a mentor in the area of signal processing but also a friend. He understood my times of pressure and patiently provided insight and direction. For his valuable time and for remaining a supporter all the way to the end, I cannot thank him enough.

The patience, advice and valuable mentoring in the NQR field of Dr. Jamie Barras cannot go unnoted; the academic support and input are greatly appreciated. I would also like to express my most heartfelt thanks and appreciation to the late Prof. Smith for his invaluable advice and providing his expertise in the field of NQR.

My gratitude is also extended to Dr. Michael D. Rowe, Dr. Iain J. Poplett, and Dr. Erik Gudmundson who have known the answer to every question I've ever asked, for unfailingly advising and answering my emails, for their help and, foremost, patience.

Many thanks to my office friends; thank you for the endless talks, lunches, your warm and friendly hearts and whatever else helped keep things light. Further, my gratitude is extended to all my Cypriot friends for their constant love,

encouragement and personal cheering; I will be forever grateful for crying, laughing and cursing together, thank you, my girls.

These acknowledgements would not be complete if I did not mention my family; parents and sister. Throughout my doctoral program, they have been constantly sending supporting vibes, emails, messages and various edible Cypriot delights. Their weeklong visits the last few years have been invaluable. They have re-energised and given me a much-needed reprieve from studying and imprinted infinite wonderful memories on my heart. Yiannakis and Emily I adore you, I am grateful for both of you and for the things you taught me.

Last, but certainly not least, I must acknowledge with tremendous and deep thanks my partner-turned-fiance, Andreas. Thanks to our loving relationship I have been happier, calmer, and more content. Through his love, patience, support and unwavering belief in me, I've been able to complete this long dissertation journey. My biggest fan and supporter, he has given me so many beautiful and unforgettable memories throughout this journey. Andreas has been central to my completion of this study as he has given me confidence and motivated me in so many ways. There are no words that can express my gratitude and appreciation for all you've done and been for me. This thesis is dedicated to you.

Dedication

To Andreas

Acronyms

AML	approximate maximum likelihood
ANOVA	analysis of variance
API	active pharmaceutical ingredient
AR	autoregressive
CPMG	Carr-Purcell-Meiboom-Gill
CRLB	Cramér-rao lower bound
EFG	electric field gradient
ETAML	echo train approximate maximum likelihood
ET-CAPA	echo train Capon APes average
FETAML	frequency selective echo train approximate maximum likelihood
FFT	fast Fourier transform
FHETAML	frequency selective hybrid echo train approximate maximum likelihood
FID	free induction decay
FIM	Fisher information matrix
FLSETAML	frequency selective least squares echo train approximate maximum likelihood
FODETAML	frequency selective offset dependent echo train approximate maximum likelihood
FRETAML	frequency selective robust echo train approximate maximum likelihood
FSAML	frequency selective approximate maximum likelihood
FT	Fourier transform
GLRT	generalised likelihood ratio test
HETAML	hybrid echo train approximate maximum likelihood
HPLC	high performance liquid chromatography

IR	infrared
LSETAML	least squares echo train approximate maximum likelihood
MANOVA	multivariate analysis of variance
MS	mass spectrometry
NIR	near-infrared
NMR	nuclear magnetic resonance
NQR	nuclear quadrupole resonance
ODETAML	offset dependent echo train approximate maximum likelihood
PAS	principal axis frame
PETN	pentaerythritol tetranitrate
PNT	paranitrotoluene
PSL	pulse spin-locking
QCC	quadrupole coupling constant
RDX	research department composition X (cyclotrimethylene trinitramine)
RETAML	robust echo train approximate maximum likelihood
REMIQS	robust estimation of multiple polymoprh QR signals
RESPEQ	robust evaluation using subspace-based methods of polymorphic quadrupole signals
RF	radio frequency
RFI	radio frequency interference
SEAQUER	subspace-based evaluation of quadrupole resonance signals exploiting robust methods sNQR
SLSE	spin-lock spin echo
SNR	signal-to-noise ratio
SQUID	superconducting quantum interference device
TLC	thin-layer chromatography
TNT	trinitrotoluene
XRD	X-ray diffraction
WHO	World Health Organisation

Notational Conventions

$X, x, \ldots$	non-bold letters denote scalars
$\mathbf{X}, \mathbf{Y}, \ldots$	bold upper case letters denote matrices
$\mathbf{x}, \mathbf{y}, \ldots$	bold lower case letters denote vectors
$\hat{X}, \hat{\mathbf{x}}, \hat{\mathbf{X}}, \ldots$	*hat* denotes an estimate
$E\{\cdot\}$	expectation operator
$(\cdot)^T$	transpose
$(\cdot)^*$	Hermitian (or conjugate) transpose
$(\cdot)^\dagger$	Moore-Penrose pseudoinverse
$\odot$	Schur-Hadamard elementwise product
$\lfloor x \rfloor$	the integer part of the scalar x
$\mathrm{diag}\{\mathbf{x}\}$	the square diagonal matrix whose main diagonal elements are the elements of the vector $\mathbf{x}$
$\triangleq$	defined as
$\|\cdot\|_2$	the two-norm
$\mathrm{Re}\{x\}$	the real part of the x
$[\mathbf{X}]_{i,j}$	the component of matrix $\mathbf{X}$ in the i^{th} row and j^{th} column
$\lvert x \rvert$	the absolute value of scalar x
$\arg\min_x f(x)$	the value of x that minimises $f(x)$
$\arg\max_x f(x)$	the value of x that maximises $f(x)$

Chapter 1

Introduction

This thesis aims to improve on signal processing and pulse sequence systems using Nuclear Quadrupole Resonance (NQR) spectroscopy, in order to overcome a series of problems associated with medicine authentication. Over the last several years, the global threat from the counterfeit medicines crime has grown dramatically. It is accepted that about 10% of medicines worldwide are counterfeit, while exact figures still remain unclear [Martino et al., 2010]. The inherent dangers associated with this problem demand the implementation of techniques to detect and remove falsified products before penetrating into the legitimate supply chain. The fight against counterfeit drugs involves governments, healthcare organisations and the police. It is reported that counterfeit medicines worth of approximately £51.6 million have been seized globally, with nearly £16 million worth of medicines being taken in UK only [Gallagher, 2015].

The current technologies range from simple evaluation of the packaging to sophisticated analytical methods for generating "chemical fingerprints". In NQR technique, the physical and chemical properties of a compound can be uniquely identified, enabling the generation of characteristic "fingerprints". This thesis presents a complete study to address several issues which often influence the accuracy of these spectral profiles.

The present chapter serves as an introduction to the main topics considered in this thesis, and is organised as follows: Section 1.1 provides a brief description of the phenomenon of NQR and some of its possible applications are highlighted. A short review on the general challenges of NQR and the several approaches followed to overcome them, are discussed in Section 1.2. An overview to the global threat of low quality and counterfeit medicines is provided in Section 1.3.

Next, Section 1.4 provides a short discussion on the current analytical techniques for NQR in medicines authentication. In Section 1.5, the main issues of NQR in medicines authentication are addressed. Finally, Section 1.6 provides an outline of the content and main contributions in this thesis.

1.1 NQR spectroscopy

Nuclear quadrupole resonance (NQR) spectroscopy is a radio frequency (RF) technique that examines uniquely polycrystalline compounds containing quadrupolar nuclei, whose spin quantum number is $I > \frac{1}{2}$. Nearly 50% of atoms in the periodic table fulfil this requirement. Examples of commonly used quadrupolar nuclei include the 99.635% naturally abundant ^{14}N and 75.4% abundant ^{35}Cl [1] nuclei [Smith, 1971]. The energy splittings in NQR, are mainly attributable to electrostatic interactions between nuclear and electron charge distributions. In contrast to the closely related technique, nuclear magnetic resonance (NMR), the signal is generated from the interaction of the electric field gradient (EFG) from the surrounding charge distribution and the quadrupole moment of the nucleus [Latosińska, 2007a; Smith, 1986]. Therefore, the absence of an external static magnetic field [2], justifies the low cost and portability of a NQR system. Application of RF radiation excites transitions between the energy levels, and the NQR signal is acquired. The method is non-invasive and non-destructive, with the RF radiation passing through materials, such as plastic and cardboard, without attenuation; therefore, there is no sample preparation required during a typical NQR measurement, since the sample under study can be analysed within its original packaging. The magnitude of the NQR signals is equivalent to the abundance of quadrupolar nuclei within the substance, illustrating the quantitative nature of this technique and ability to examine bulk quantities [Tate et al., 2009; Balchin et al., 2005; Barras et al., 2012a; Perez et al., 2005]. Moreover, NQR is able to distinguish among solids that occur in more than one polymorphic forms [Latosińska, 2007a; Perez et al., 2005; Tate et al., 2009]. Due to the extreme sensitivity to dynamical alterations within the solid substance, NQR is amenable in several applications, which can be broadly classified as either detection or pharmaceutical analysis applications.

[1] Nitrogen-14 (^{14}N) and Chlorine-35 (^{35}Cl).

[2] In NMR, energy splittings are governed by interactions of the magnetic dipole moments of the nuclei with the effective field generated by an external static magnetic field [Slichter, 2013].

The ability and distinct potential of NQR to verify uniquely the presence of a target compound has attracted attention in the areas of explosives and narcotics detection; this is because most explosives and narcotics contain quadrupolar nuclei. NQR has been shown to detect a wide range of nitrogen-containing bulk explosives, such as trinitrotoluene (TNT) [Gregorovič and Apih, 2009c; Marino and Connors, 1983; Garroway et al., 1994a], cyclotrimethylene trinitramine (RDX) [Smith et al., 2011; Rudakov et al., 1997] , pentaerythritol tetranitrate (PETN) [Garroway et al., 1994a] and other ammonium nitrate based explosives [Miller, 2007; Barras et al., 2004; Miller and Barrall, 2005]. With an intrinsically very low probability of false alarm, explosives detection has been exploited in applications such as baggage screening [Garroway et al., 1994b], landmine detection [Smith et al., 2003; Tantum et al., 1999; Miller and Barrall, 2005], vehicle [Barras et al., 2004] and personnel screening [Miller, 2007]. Cardona et al. [2015] describe the development of a portable NQR system for remote detection of ammonium nitrate. Furthermore, narcotics such as heroin [Balchin et al., 2004; Pati et al., 1998], cocaine [Yesinowski et al., 1995], opium [Grechishkin and Sinyavskii, 1997] and methamphetamine [Shinohara et al., 2012a] have been detected and analysed using pure ^{14}N NQR.

In recent years, NQR has been established as a powerful technique in pharmaceutical applications [Hammond, 1955; Latosińska, 2007a; Perez et al., 2005; Balchin et al., 2005; Blinc et al., 2006]. Almost 90% of commercially available pharmaceuticals are administered in solid forms; therefore, NQR can analyse and detect the active pharmaceutical ingredient (API) from a broad range of medicines. The most useful quadrupolar nuclei in pharmaceutical studies include ^{14}N, ^{35}Cl, ^{79}Br and ^{127}I [3]. Even though the abundance of the common ^{14}N is higher, the generated signals are in low frequency range (order of $0.4 - 6$ MHz), whereas, for instance, the less common ^{35}Cl nucleus produces signals in much higher frequencies (order of 40 MHz) [Smith, 1971]. The NQR signals are obtained from medicines within their blister packs, packets or bottles, and coils can therefore be designed in any preferable geometry in order to fit the sample [Barras et al., 2012b; Kyriakidou et al., 2015]. The EFG is a characteristic property of the crystal; thus, there is a signature quadrupolar frequency for every compound. One aspect of the pharmaceutical applications of NQR is for drug development which includes identification of samples whose API exists in different solid forms

[3] Bromine-79 (^{79}Br) and Iodine-127 (^{127}I).

(polymorphs, amorphous), detection of impurities, characterisation of the drug's structure and thermal stability [Latosińska and Latosińska, 2011; Luźnik et al., 2014]. Moreover, the excipients or coating material do not interfere and cause no modifications in the final spectrum; a benefit over other techniques such as powder X-ray Diffraction (XRD), Fourier transform near infrared (FT-NIR) or Raman spectroscopies which may be hampered due to the tablet coating, packaging and fluorescence signals [Sacré et al., 2010; Eliasson and Matousek, 2007]. The versatility of the use of NQR in the pharmaceutical industry is not limited. An extensive amount of research suggests the potential of NQR for quality control of pharmaceutical products, both during the manufacturing process or storage, with the characteristic signal parameters being used for monitoring purposes [Limandri et al., 2011; Latosińska, 2007a; Gregorovič, 2015].

This thesis focuses on the potential application of NQR in medicines *authentication*.

1.2 Challenges in NQR

Much of the active research in NQR focuses in the development and improvement of techniques to overcome several challenges. While the majority of the work refers to explosives detection, the reported progress in *signal creation methods*, *hardware design*, and *signal processing techniques*, is equivalently applied in detection of medicines. NQR suffers from inherently weak signals. Repeated measurements are commonly performed and the signals are added coherently for signal intensity enhancement; however, at the expense of prolonged experimental durations. This occurs because the signal-to-noise (SNR) is proportional to the square root of the number of signal averages. The design of different patterns of RF pulses (i.e., pulse sequences) has been thoroughly studied to improve detection efficiency in NQR [Mikhaltsevitch and Rudakov, 2004; Osokin, 1982; Rudakov et al., 1997; Rudakov and Mikhaltsevich, 2003; Meiboom and Gill, 1958; Rudakov and Belyakov, 1998]. Some of those approaches include the sample excitation with multiple frequencies [Sauer et al., 2001; Mozzhukhin et al., 2012], single pulse echoes due to their lower power demands [Prescott et al., 2008], and double resonance measurements [Prescott, 2010; Prescott et al., 2012; Blinc et al., 2006]. Moreover, cross polarisation techniques successfully demonstrate an increase in SNR, with a static magnetic field being applied prior to the NQR

experiment in order to polarise protons (spin $I = \frac{1}{2}$), and the energy is then transferred to the quadrupolar system via coupling of magnetic dipoles [Rudakov, 2012; Blinc et al., 2006; Kim et al., 2014; Gregorovič and Apih, 2008]. From the hardware perspective, improved coil designs [4] have been developed to maximise sensitivity and field homogeneity [Cardona et al., 2015; Shinohara et al., 2012a; Tate et al., 2009; Barras et al., 2012b; Mikhaltsevitch et al., 2007; Mozzhukhin et al., 2005; Gregorovič and Apih, 2009a; Shinohara et al., 2012b]. Depending on the application, the coils may vary in shape and size (e.g., cylindrical or rectangular solenoids, flat loops of wire). Moreover, alternative to conventional coils, several studies report on the use of magnetometers such as the superconducting quantum interference devices (SQUIDs) [Yesinowski et al., 1995; Augustine et al., 1998; Tachiki et al., 2007] and atomic magnetometers [Lee et al., 2006], which are more sensitive at low resonance frequencies [Miller, 2007].

In detection applications, the NQR system may be corrupted by external radio frequency interference (RFI), especially for unshielded coils. For instance, in explosives detection, most of the resonance frequencies in NQR, lie in the region of $0.5 - 5$ MHz [Miller, 2007], and often overlap with the submarine communications, AM and short wave broadcast [Miller and Barrall, 2005]. An extensive research work has been undertaken for the development of novel parametric signal processing detection algorithms to fulfil RFI suppression and SNR improvement (see Section 2.8.2). The two main approaches used to overcome RFI in NQR detection are the use of gradiometer coils [Suits, 2004; Itozaki, 2013] and reference antennas that capture noise only data, which can then be subtracted from the NQR signal [Somasundaram et al., 2009; Butt and Jakobsson, 2011]. Recent advances in signal processing methods enabled parametric modelling, based on exploiting the rich structure of the NQR signal [Jakobsson et al., 2005a; Butt et al., 2008b; Somasundaram et al., 2007].

The occurrence of spurious signals, such as piezoelectric [Choi and Yu, 1989] and magnetoacoustic [Miller, 2007] ringing, caused by quartz or small magnetic particles in the material, may result in signal contamination. Typically, phase cycling pulse sequences such as the spin-lock spin echo (SLSE) sequence (see Section 2.6.2) are implemented prior to processing to largely eliminate those effects

[4] In NQR, the hardware requirements are relatively simple; a transmitter part to generate the RF field, and a receiver for detection. The conventional coils are based on Faraday detection.

[Mikhaltsevitch et al., 2004a; Latosińska, 2007a; Balchin et al., 2005]. Also, further hardware improvements such as low impedance coils may be used to reduce piezoelectric signals [Suits, 2004].

Finally, it is important to note that NQR cannot be used for the detection of liquid substances. NQR signals are generated from quadrupolar nuclei within solid materials. Due to molecular motion in liquids, the local magnetic fields will be averaged out, and thus, no signal will be observed.

1.3 The threat of counterfeit medicines

The spread of the crime of counterfeit pharmaceuticals is threatening public health globally, especially in developing countries where there is weak pharmacovigilance and regulatory oversight. The prevalence of this emerging and complex problem has serious health consequences, including treatment failure, drug resistance, severe drug reactions including death, as well as undermining of consumers' confidence [Fernandez et al., 2008; Kovacs et al., 2014; Wertheimer and Norris, 2009]. Consequently, there is an increase in healthcare costs with the reputation and credibility being jeopardised [Martino et al., 2010]. Unfortunately, exact figures on the degree of this problem remain inaccurate due to lack of robust data and information on counterfeit incidents [Martino et al., 2010]. However, published reports show that the threat is severe and has grown significantly over the years [UN, 2013; NABP, 2011]. According to the Pharmaceutical Security Institute, the number of incidents has been increased almost by 100% for the period of 2005 and 2014, with 2,177 incidents being documented in 2014 [PSI, 2014; Mackey et al., 2015; Nayyar et al., 2015]. It is generally accepted that 10% of medicines around the world are counterfeit, with this percentage fluctuating from country to country [Fernandez et al., 2008; WHO, 2012; Martino et al., 2010]. The online market is the easiest and major source of counterfeit medicines which targets unsuspecting and vulnerable individuals. In fact, more than 50% of online "pharmacies" are suspected of selling fake drugs [Nayyar et al., 2015; Fernandez et al., 2008; Martino et al., 2010].

The World Health Organization (WHO) definition refers to a counterfeit medicine as a "product that is deliberately and fraudulently mislabelled with respect to identity and/or source. Counterfeiting can apply to both branded and generic products. Those may include products with the correct active ingredients,

or with the wrong ingredients, without active ingredients, with insufficient active ingredients, or with fake packaging" [WHO, 2012]. Substandard products also pose an additional challenge. The WHO describes those medicines as substances produced without a deliberate misrepresentation, but as low-quality products with possibly the wrong dosage of active pharmaceutical ingredient (API) that do not meet the quality assurance standards, or being degraded because of bad transport or poor storage conditions [WHO, 2012; Newton et al., 2011; Kyriakidou et al., 2015; Martino et al., 2010]. Low quality drugs can often be detected in developed countries [Holzgrabe and Malet-Martino, 2011]; for instance, substandard Viagra® products were reported in the United Kingdom [Deisingh, 2005]. Fake products span a wide range of expensive treatment and lifestyle medicines. Some examples include steroids, hormones, fat reduction and anticancer drugs [Deisingh, 2005; Gostin et al., 2013; Hajjou et al., 2015]. However, counterfeiters also target low cost products such as simple painkillers and antibiotics; in Newton et al. [2010], Newton et al. [2006], Holzgrabe and Malet-Martino [2011], the authors refer to a case where almost 500 children died due to ingestion of fake paracetamol that contained renal toxin. Perhaps the most disappointing and disturbing figures are the incidents of counterfeit life-threatening medicines, that are used to cure diseases such as malaria and AIDS [Cockburn et al., 2005], with the latter being the most widely targeted, particularly in developing countries [Newton et al., 2011; Dondorp et al., 2004; Nayyar et al., 2012b].

1.4 NQR in medicines authentication

Controlling the penetration of counterfeit medicines into the legitimate supply chain is essential, and demands implementation of techniques to investigate the content of those products, before reaching the patient. Typically, a standard workflow for tackling counterfeit drugs starts with careful visual inspection of packaging characteristics, as well as physical appearance of tablets. Pharmaceutical manufacturers develop authentic ways to fight counterfeit products, with security print features such as unique watermarks, holograms, chemical tracers, and barcodes [Dondorp et al., 2004; Deisingh, 2005]. In some cases, fake packaging can be easily identified [Newton et al., 2011]. Counterfeiters can often replicate almost accurately the originality of the genuine packaging, and evade

the visual tests; therefore, this demands the implementation of sophisticated analytical techniques to generate "chemical fingerprints". The key features that determine the suitability and applicability of several approaches in developed, and especially in low or middle income countries include: sample preparation, sensitivity, specificity, speed of analysis, cost, level of operator's skills, portability, comprehensiveness and ease of data analysis [Kovacs et al., 2014; Fernandez et al., 2008]. The ultimate aim of analytical methods is to determine the correct amount of API (quantitative analysis) and assess the drug's quality and degradation during storage and handling in the field, at all points of the supply chain [Fernandez et al., 2008]. Among these techniques, thin-layer chromatography (TLC) [Martino et al., 2010], colorimetric methods [Deisingh, 2005], high performance liquid chromatography (HPLC) [Deconinck et al., 2013], mass spectrometry (MS) [Culzoni et al., 2014], powder X-ray diffraction (XRD) [Maurin et al., 2007], NMR [Holzgrabe and Malet-Martino, 2011], near-infrared (NIR) [Rodionova and Pomerantsev, 2010; De Peinder et al., 2008] and Raman spectroscopy [Eliasson and Matousek, 2007; Neuberger and Neusüß, 2015; Dégardin et al., 2011] have been effectively applied to analyse fake medicines. Unfortunately, from the aforementioned methods, it is difficult to select a single best method that could potentially be applied to all tasks and cases. For instance, TLC and colorimetric methods are widely used in developing countries because of the low costs associated with them, ease of use and portability, but both are invasive and destructive since sample preparation is required. Moreover, the sophisticated HPLC is considered as the gold standard method in drug analysis [Martino et al., 2010]; it provides destructive quantitative drug profiling, but the expense and complexity of laboratory skills hinders its use in the field, especially in poorer countries with less resources [Martino et al., 2010]. NIR and Raman spectroscopic methods are also successfully employed as they are portable, relatively fast, mainly qualitative and non-destructive techniques which require minimum training [Martino et al., 2010; Nayyar et al., 2015].

All of the aforementioned methods are in some extent invasive since they are best-suited in analysing individual pills. Although relatively "fresh" in this application, NQR can be another promising technique in medicines authentication, to fight against the problem of fake drugs [Barras et al., 2012a; Blinc et al., 2006; Barras et al., 2013, 2012b; Kyriakidou et al., 2015; Seliger et al., 2010; Lužnik

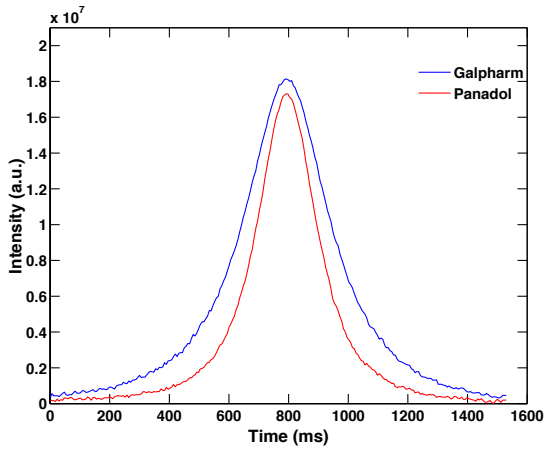

Figure 1.1: ^{14}N NQR signal lineshape of powder paracetamol of two different manufacturers ($\nu = 2.563$ MHz, T= 295 K); Galpharm and Panadol.

et al., 2013; Luźnik et al., 2014]. Barras et al. [2012a] illustrate the application of NQR to generate "fingerprints" of genuine medicines, by exploiting the characteristic features of the NQR signals under specific experimental conditions. NQR provides accurate quantification of the API of medicines, with no sample preparation and complex chemometric analysis [Tate et al., 2009]. Moreover, due to its high sensitivity and specificity, the time constants, which describe the signals, are indicators of the manufacturing process and type of formulation [Lužnik et al., 2013; Kyriakidou et al., 2015]; i.e., distinguish among capsules, caplets and powders. As described by Lužnik et al. [2013] and Latosińska [2007a], one of the NQR signal parameters, the signal lineshape, serves as an identification feature of medicines produced from several manufacturers. Figure 1.1 presents an example based on two analgesic paracetamol samples from two different manufacturers; Galpharm and Panadol. In Lužnik et al. [2013], the authors have related the change in the spectral linewidth with the compacting pressure of the paracetamol tablets' preparation. Moreover, Barras et al. [2013] report on the detection of a suspected counterfeit antimalarial drug via quantitative comparison with its genuine version. NQR was able to accurately determine the amount of API in the suspected batch, which was lower than the expected dosage. Therefore, because of the high sensitivity in crystalline fluctuations, the NQR phenomenon enables the exact profiling of the physical and chemical properties of the material and relates any changes of the signal parameters in the processing of the API. Moreover, several NQR research groups demonstrated hardware advances of NQR systems, highlighting the portable and inexpensive features of the method

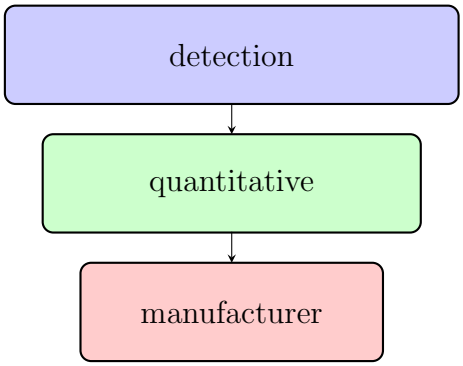

Figure 1.2: Simple block diagram of NQR in a medicines authentication application.

and its capabilities in field applications [Cardona et al., 2015; Beguš et al., 2014; Barras et al., 2012a; Zhang et al., 2014; Barras et al., 2004]. For instance, Beguš et al. [2014] report on the development of a light and battery-operated miniaturised NQR spectrometer, where with the aid of a planar coil, the detection of various materials (medicines and explosives) was feasible. Also, the NQR group at King's College London, demonstrated the development of two portable NQR systems for medicines authentication; the first allowed the screening of medicines within their packets using conventional low cost coils [5], whereas the second implemented a hand-held antenna for complete non-invasive authentication [6] [Barras et al., 2012a; Conphirmer, 2011].

1.5 Challenges of NQR in medicines authentication

In medicines authentication, one simply needs to answer the question: "do the contents of this medicine match its label?". In practice, a system will contain a database of accurate "fingerprints" of medicines generated under specified experimental conditions and protocols. Figure 1.2 shows a simple block diagram of what a NQR system needs to answer in an authentication scenario. The series

[5] In 2010, the NQR group at King's College London (KCL) was awarded by the UK healthcare charity, Wellcome Trust, to develop a prototype of a portable NQR device for medicines authentication, focusing on field applications in developing countries [Barras et al., 2012a].

[6] In 2011, KCL was the coordinator of the CONPHIRMER consortium which developed a hand-held portable NQR device, tested both in the laboratory and real environment [Conphirmer, 2011].

of realistic questions could be: "Is the correct API present (detection)?" "Does it contain the expected amount of API (quantitative)?" "Is it made under the prescribed quality control standards and processing (manufacturer)?"

Despite the numerous benefits of NQR in medicines authentication, several factors might influence the accuracy of the pharmaceutical "fingerprints" and hamper its real application in the field. The following bullets summarise the main issues:

- A major challenge is the weak SNR caused by the low resonance frequencies.
- Depending on the level of authentication, the duration of an experiment can be prohibitively long.
- Imprecise knowledge of the compound's temperature, may lead to an unexpected weakening of the signal amplitude.
- Significant variability appearing between batches of medicines produced by the same company and under exact processing conditions. Several factors contribute in the product's stability and degradation.

This thesis improves upon the aforementioned issues by proposing an improved NQR signal data model and signal processing algorithm, introducing versatile approaches for the optimised use of data processing methods, and investigating the signals from several medicines.

1.6 Thesis Outline and Contributions

Here, an outline of the content and the main contributions of each chapter included in this thesis are briefly described.

Chapter 2 – Background Theory

This chapter provides an overview of the scientific fundamentals of the NQR phenomenon, with a brief introduction on the quantum mechanical approach which describes the interaction that gives rise to distinct energy levels and the effects of the applied RF pulses on the NQR system. The commonly used conventional pulse sequences, the types of NQR signals and the relaxation mechanisms that describe these signals are explained. Moreover, a short overview of the factors influencing the NQR signal characteristic parameters is provided, which emphasises on the influence of the sample temperature. Finally, a summary on the current state-of-the-art NQR signal models and advanced parametric signal processing algorithms is provided.

Chapter 3 – Experimental

The experimental chapter begins with a short introduction on the basic hardware used in NQR spectroscopy, followed by a description of the experimental equipment and pulse sequence that are used to obtain the data in this thesis. The procedure followed to stabilise and monitor the temperature of the medicines during the measurements is also provided.

Chapter 4 – Exploiting Off-resonance Effects

Chapter 4 focuses on exploiting the dependence of the signal amplitude on the *off-resonance effects*. Uncertainties in the temperature during a measurement, generate off-resonance effects, which render the expected signal amplitude to vary significantly. A previously proposed theoretical model that describes the dependence of the signal amplitude on these effects is exploited and implemented in the NQR echo train model. Current detectors did not exploit this dependency [Somasundaram et al., 2007; Jakobsson et al., 2006] . Herein, the current state-of-the-art signal processing algorithm, echo train approximate maximum likelihood (ETAML) is extended to incorporate the improved signal model. This forms the

offset dependent echo train approximate maximum likelihood (ODETAML) detector and its frequency selective counterpart, FODETAML. Derivation of the corresponding Cramér-Rao lower bound (CRLB) reveals the statistical efficiency of the FODETAML detector. Such improved bounds allow the determination of experimental conditions for optimised detection and authentication; significant contribution in quantitative NQR analysis. Chapter 4 is based on [Kyriakidou et al., 2014]:

G. Kyriakidou, A. Jakobsson, E. Gudmundson, A. Gregorovic, J. Barras, and K. Althoefer. Improved modelling and bounds for NQR spectroscopy signals. In *2014 Proceedings of the 22nd European Signal Processing Conference* (EUSIPCO 2014), pp 2325–2329. Institute of Electrical and Electronics Engineers: Piscataway, NJ, 2014.

G. Kyriakidou, A. Jakobsson, E. Gudmundson, J. Barras, and K. Althoefer. Exploiting off-resonance effects in Nuclear Quadrupole Resonance. *Analytical Chemistry*, 2016.; *under review.*

Chapter 5 – Discrimination of Paracetamol Batches

NQR has been proved extremely sensitive in crystalline modifications, allowing the detection and authentication of medicines produced by different manufacturers. The variability among medicines of the same formulation and manufacturer might affect the outcome of an authentication test. This issue can cause problems when testing for counterfeit medicines; especially, when one deals with "high-quality" fake medicines that may contain the correct or similar chemical composition but differ in terms of excipients, API, and manufacturing conditions. The batch-to-batch variability is examined, from batches of analgesic paracetamol tablets with varying use-by dates. The difference among medicines is determined through the variability of their estimated damping constants. Furthermore, the outcome highlights NQR as a possible indicator of the influence of ageing in medicines' degradation, and the necessity of the long term monitoring of their "fingerprints". Chapter 5 is based on [Kyriakidou et al., 2015]:

G. Kyriakidou, A. Jakobsson, K. Althoefer, and J. Barras. Batch-specific discrimination using nuclear quadrupole resonance spectroscopy. *Analytical Chemistry*, 87(7), pp: 3806–3811, 2015.

Chapter 6 – Optimising the Utility of Signal Processing Methods Through Pulse Sequence Design

A "fingerprint" of a medicine is generated using the characteristic parameters of the NQR signal. The estimation accuracy can be influenced either by a low SNR or by the choice of the signal acquisition parameters. In Chapter 6, flexible approaches that seek to identify limits in the estimation accuracy of the damping parameters are proposed. Being able to determine such limits, the utility of the applied detection algorithm (here, the FODETAML) is optimised through conditions that help to design the desired pulse sequence.

G. Kyriakidou, A. Jakobsson, J. Barras, and K. Althoefer. Optimising signal processing methods in medicines authentication using Nuclear Quadrupole Resonance. *Analytical Chemistry*, 2016.; *under review.*

Chapter 7 – Conclusions

In Chapter 7, the conclusions, thesis contributions as well as a discussion on future perspectives are drawn.

Collaborative Related Work

In addition to the publications listed above, the author has collaborated and contributed in two research studies which focused on medicines authentication using NQR through experimental analysis and hardware design. These publications are the following: [Barras et al., 2013, 2012b]:

J. Barras, D. Murnane, K. Althoefer, S. Assi, M. D. Rowe, I. J. Poplett, G. Kyriakidou, and J. A. Smith. Nitrogen-14 nuclear quadrupole resonance spectroscopy: A promising analytical methodology for medicines authentication and counterfeit antimalarial analysis. *Analytical Chemistry*, 85(5), pp: 2746–2753, 2013.

J. Barras, S. Katsura, H. Sato-Akaba, H. Itozaki, G. Kyriakidou, M. D. Rowe, K. A. Althoefer, and J. A. Smith. Variable-pitch rectangular cross-section radio frequency coils for the nitrogen-14 nuclear quadrupole resonance investigation of sealed medicines packets. *Analytical Chemistry*, 84(21), pp: 8970–8972, 2012.

Chapter 2

Background Theory

The aim of this chapter is to present an overview of the basic principles of NQR spectroscopy, highlight the factors influencing the NQR characteristic parameters and provide an overview of the current state-of-the-art signal processing detection algorithms in NQR. Since NQR spectroscopy is a branch of NMR spectroscopy, the chapter begins with Section 2.1 containing the basic scientific fundamentals of NMR. In Section 2.2, the quantum mechanical approach that describes the interaction of the electric quadrupole moment and the electric field gradient from the surrounding charges, giving rise to distinct energy levels, is provided. In this thesis, measurements on several medicines containing ^{14}N nuclei of spin $I = 1$ were conducted. Therefore, Section 2.3 provides an overview of the quantum mechanical treatment of the quadrupole energy levels and resonance frequencies for those nuclei. Application of RF radiation drives transitions between the energy levels, creating the observed NQR signal; this process is described in Section 2.4. Furthermore, Section 2.5 follows with a description of the relaxation processes in the NQR system. Section 2.6 describes the types of NQR signals and the pulse sequence commonly used in several NQR applications. In Section 2.7, a short overview of the factors influencing the NQR parameters is given. Finally, Section 2.8 provides an overview of the current state-of-the-art advanced parametric signal processing algorithms used in NQR.

2.1 Principles of Nuclear Magnetic Resonance

In NMR spectroscopy, the energy splittings are mainly due to magnetostatic interactions between the nuclear magnetic moments and an externally applied

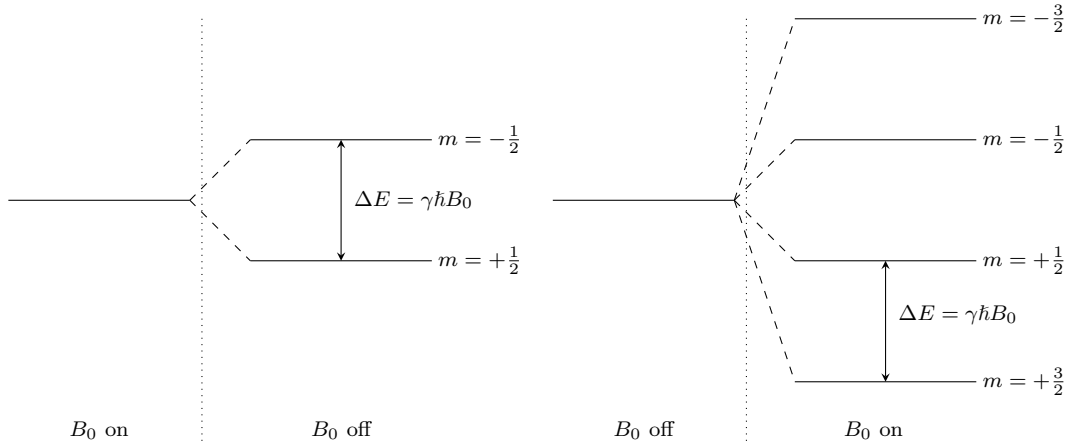

Figure 2.1: Quantum energy levels for nuclear spin $I = \frac{1}{2}$ (left) and $I = \frac{3}{2}$ (right) in a magnetic field B_0.

magnetic field. Nuclei that possess an overall spin, $I \geq \frac{1}{2}$, are associated with a nuclear magnetic moment, $\boldsymbol{\mu}$. Characteristically, when the mass number, M ($M = Z + N$, with the atomic number Z being the number of protons, and N, the number of neutrons), of a nucleus is odd, $I = \frac{n}{2}$, whereas, for a nucleus of even mass number, $I = n$, with n denoting an integer number. Zero-spin nuclei, $I = 0$, occur when both Z and N are even [Darbeau, 2006]. In quantum mechanics, the magnetic moment is expressed in terms of the nuclear angular momentum, according to

$$\boldsymbol{\mu} = \mathbf{I}\gamma\hbar, \tag{2.1}$$

with $\mathbf{I}$, γ and $\hbar$ denoting the dimensionless angular momentum operator, with $I(I+1)$ eigenvalues, the "gyromagnetic ratio" and Planck constant, respectively. In the absence of a static magnetic field, the nuclear magnetic moments precess in a random orientation. When the NMR nuclei are exposed to an external magnetic field, $\mathbf{B}_0$, their magnetic dipole moments precess about the field, aligning in $2I+1$ possible quantum states. In each spin state, the spin vector will have a different orientation, such that the component of $\mathbf{I}$, parallel to the applied field has $m\hbar$ values, with $m = -I, -I+1, \ldots, +I$ [Slichter, 2013; Freeman, 1998; Cowan, 2005]. Thus, for a spin $I = \frac{1}{2}$ nucleus, the values of m are $\pm\frac{1}{2}$, and similarly, for a nucleus of spin $I = \frac{3}{2}$, $m = -\frac{3}{2}, -\frac{1}{2}, +\frac{1}{2}, +\frac{3}{2}$. This phenomenon is illustrated in Figure 2.1. Examples of spin–$\frac{1}{2}$ nuclei include ^{1}H, ^{3}He, and ^{13}C; for spin–$\frac{3}{2}$ nuclei, ^{7}Li, ^{23}Na

and ^{35}Cl [1] [Cowan, 2005]. From quantum mechanics, the energy generated from the interaction between the magnetic dipole moment and the applied magnetic field, is described by the simple Hamiltonian, [Slichter, 2013],

$$\mathbf{H} = -\boldsymbol{\mu}\cdot\mathbf{B}_0. \tag{2.2}$$

In NMR, the static magnetic field is chosen to lie parallel to the z-direction of the coordinate system, referred to as the *laboratory frame* of reference [Lee, 2002]. Thus, the energy can be expressed as

$$\mathbf{H} = -\gamma\hbar B_0 I_z, \tag{2.3}$$

with the solutions of this Hamiltonian being only multiples of the I_z eigenvalues, and the allowed energies are given by

$$E_m = \gamma\hbar B_0 m. \tag{2.4}$$

Irradiation of the sample by electromagnetic radiation at a particular angular frequency, ω (resonance condition), will cause transitions between the energy levels, with the energy difference between the ground and the excited nuclear Zeeman energies expressed as

$$\Delta E = \gamma\hbar B_0, \tag{2.5}$$

and

$$\omega = \gamma B_0. \tag{2.6}$$

with γ being different among various nuclei [Slichter, 2013]. While in NMR an experimentalist controls the main interacting field (normally based in a laboratory), in NQR the fields responsible for the nuclear interactions are created at the molecular and nuclear levels [Lee, 2002]. The static nature of the external applied field allows the existence of the energy splittings even in the case of molecular motions. Thus, the fundamental Hamiltonian – Zeeman Hamiltonian – in NMR is

[1] Hydrogen-1 (^{1}H), Helium-3 (^{3}He), Carbon-13 (^{13}C), Lithium-7 (^{7}Li), Sodium-23 (^{23}Na) and Chlorine-35 (^{35}Cl).

independent on the molecular properties of the material. In contrast, quadrupolar nuclei are highly sensitive, even at slight changes in their surrounding electric charge distributions.

2.2 Quadrupolar Moment

NQR exploits the interaction between the electric quadrupole moment (Q) of the nucleus, and the EFG, created by the surrounding electric charges. The origin of this interaction is based on the quadrupolar nature of the nucleus. Quadrupolar nuclei have spin quantum number $I > \frac{1}{2}$, with a non-spherically symmetric charge distribution. Such a distribution is classically represented by an ellipsoid, derived from a *compressed* or *extended* sphere along a preferred direction [Smith, 1971, 1986; Slichter, 2013]. The charge distribution may be compared with that of two adjacent and antiparallel electric dipoles, that possesses an electric "quadrupole moment" Q, defined as

$$eQ = \int e\rho(3z^2 - r^2)dV, \tag{2.7}$$

where the non-zero scalar, eQ, denotes the electric quadrupole moment (e: elementary unit of charge) which reflects the deviations from spherically symmetric distributions, and ρ [2] is the nuclear charge density in a volume element dV. A simple illustration of the quadrupolar nucleus is shown in Figure 2.2. The quadrupole moment is expressed in units of cm^2, and can be positive if the ellipsoid is prolate (extended) and negative if it is oblate (compressed); for a symmetric spheroid, the integral in (2.7) will be zero. When a quadrupolar nucleus is exposed in a non-zero EFG, it responds to a turning torque generated by the two anti-parallel dipoles by precessing about the direction of the maximum EFG; a phenomenon that is similar to a magnetic moment in an applied magnetic field. The precessional frequency is proportional to the quadrupole coupling constant (see Section 2.2.1) and it is orientation dependent [Smith, 1971]. Quadrupole resonance interactions are measured directly in crystalline solids, where their rigid molecular lattice enables the nuclei to be fixed in rigid positions within the substance. Nearly 130 isotopes contain quadrupolar nuclei [Latosińska, 2007a]. A few examples include

[2] Conventionally, in the definition of the quadrupole moment, ρ denotes the nuclear charge density. In the rest of the thesis, ρ will denote a scaling due to the SNR. Chapter 4 contains further information.

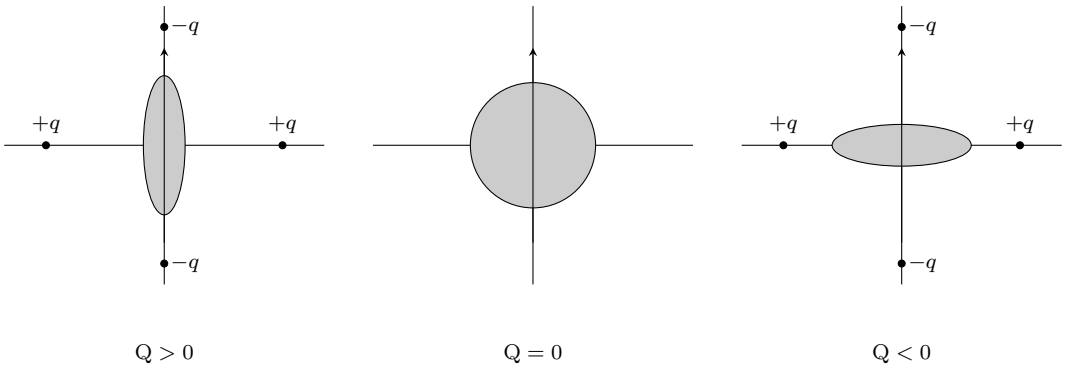

Figure 2.2: Nuclear electric quadrupole moment.

the nearly 100% abundant ^{14}N, ^{35}Cl and ^{17}O isotopes [3], with $I = 1$, $I = \frac{3}{2}$ and $I = \frac{5}{2}$, respectively [Suits, 2006; Smith, 1971]. Due to rapid molecular motion, the EFGs at the nuclear sites are averaged to zero in liquid substances, causing loss of the quantum energy splittings [Lee, 2002].

2.2.1 Hamiltonian of the Quadrupole Interaction

In NQR, the EFG can be described by the spatial derivatives of the electrostatic potential energy V, evaluated at the origin of the coordinate system of the nucleus. This tensorial quantity is given by,

$$V_{ij} = \frac{\partial^2 V}{\partial r_i \partial r_j} = q_{ij}, \tag{2.8}$$

where $r_i = x, y, \text{or } z$ and $r_j = x, y, \text{or } z$, with nine total components [Smith, 1971, 1986]. Using characteristic properties of tensors, the coordinate system in NQR is defined as the *principal axis system* (PAS) frame, in which the partial cross-derivatives are zero, and only the q_{xx}, q_{yy} and q_{zz} components are finite. These components are conventionally given as $|q_{zz}| \geq |q_{yy}| \geq |q_{xx}|$, with q_{zz} (also denoted by q) being the largest principal component of the EFG. Thus, the EFG is a diagonal, traceless tensor of second rank, and symmetric since $\partial^2 V/\partial r_i \partial r_j = \partial^2 V/\partial r_j \partial r_i$. Using Laplace's equation in electrostatics,

$$q_{xx} + q_{yy} + q_{zz} = 0. \tag{2.9}$$

[3] Oxygen-17 (^{17}O).

The quantum mechanical expression of the interaction energy, quadrupolar Hamiltonian, is thus given by the quantum mechanical operators $\hat{\mathbf{V}}_{ij}$ and $\hat{\mathbf{Q}}_{ij}$ (see (2.7)), so that,

$$\begin{aligned}\mathbf{H}_Q &= \frac{1}{6}\sum_{ij}\hat{\mathbf{V}}_{ij}\hat{\mathbf{Q}}_{ij} \\ &= \frac{e^2qQ}{4I(2I-1)}\left\{3\hat{I}_z^2 - I(I+1) + \frac{\eta}{2}(\hat{I}_+^2 + \hat{I}_-^2)\right\}, \end{aligned} \tag{2.10}$$

where $\hat{I}_z$ is the z-component of the angular momentum operator, and $\hat{I}_+$ and $\hat{I}_-$ are the raising and lowering operators, expressed in terms of the x and y components [Smith, 1986; Meriles, 2001]. These operators are defined as $\hat{I}_\pm = \hat{I}_x \pm i\hat{I}_y$, corresponding to the magnetic selection rule $\Delta m = \pm 1$. Therefore, the appropriate eigenvalues of the Hamiltonian in (2.10) will give $2I+1$ energy levels, from which transitions are computed at the sample's characteristic frequencies. The interested reader is referred to Slichter [2013] and Das and Hahn [1958] for details on the derivation of the quadrupolar Hamiltonian. Since only two components are required to characterise the principal components of the EFG tensor, one defines the asymmetry parameter, η, as

$$\eta = \frac{q_{xx} - q_{yy}}{q_{zz}}, \tag{2.11}$$

which is a dimensionless positive number varying between zero and unity. The asymmetry parameter measures the departure of the EFG at the nucleus from axial symmetry. Analogously, the quadrupole coupling constant (QCC) is a measure of the magnitude of quadrupolar interactions, in units of Hertz, defined as

$$\text{QCC} = \frac{e^2qQ}{h}, \tag{2.12}$$

where $q = q_{zz}$. The NQR frequencies depend on both the QCC and η parameters.

2.3 Spin-1: Energy Levels and Resonance Frequencies

In this thesis, measurements on materials with ^{14}N quadrupolar nucleus were obtained. This section considers the solutions of the quadrupolar Hamiltonian for

spin-1 nuclei. Using the expression in (2.10), one selects $I = 1$ with eigenvalues $m = -1, 0, +1$. There are three eigenfunctions of the angular moment operators, $\hat{I}$. Thus, the quantum states, $|I, m\rangle$, are given by $|1, +1\rangle$, $|1, 0\rangle$, $|1, -1\rangle$, such as

$$|1, +1\rangle = \begin{pmatrix} 1 \\ 0 \\ 0 \end{pmatrix} \quad |1, 0\rangle = \begin{pmatrix} 0 \\ 1 \\ 0 \end{pmatrix} \quad |1, -1\rangle = \begin{pmatrix} 0 \\ 0 \\ 1 \end{pmatrix}. \tag{2.13}$$

As described in Lee [2002], using the angular momentum operators in spherical matrix basis, the quadrupolar Hamiltonian may be presented in the matrix form,

$$\mathbf{H} = \frac{e^2qQ}{h} \begin{bmatrix} 1 & 0 & \eta \\ 0 & -2 & 0 \\ \eta & 0 & 1 \end{bmatrix} \tag{2.14}$$

Solutions are determined by diagonalising the Hamiltonian matrix and this is achieved by selecting the linear combinations of the appropriate magnetic spin wavefunctions defined as [Smith, 1986],

$$\begin{aligned} \Psi_+ = \Psi_y &= \frac{1}{\sqrt{2}}(|+1\rangle + |-1\rangle) \\ \Psi_- = \Psi_x &= \frac{1}{\sqrt{2}}(|+1\rangle - |-1\rangle) \\ \Psi_0 = \Psi_z &= |0\rangle. \end{aligned} \tag{2.15}$$

Since the quadrupolar Hamiltonian is an energy operator that defines the quadrupolar interaction, its expectation value at the eigenstate $|I, m\rangle$ can be used to compute the energy levels. This quantity is defined as,

$$\langle H_Q \rangle = \frac{\langle I, m|H_Q|I, m\rangle}{\langle I, m|l, m\rangle}. \tag{2.16}$$

Evaluating (2.16) using (2.10) and (2.15), the three quadrupole energy levels can be computed as

$$\begin{aligned} E_+ = E_y &= \frac{\langle \Psi_+ | H_Q | \Psi_+ \rangle}{\langle \Psi_+ | \Psi_+ \rangle} \\ &= \frac{1}{4}(e^2qQ)(1+\eta) \end{aligned} \tag{2.17}$$

$$\begin{aligned} E_- = E_x &= \frac{\langle \Psi_- | H_Q | \Psi_- \rangle}{\langle \Psi_- | \Psi_- \rangle} \\ &= \frac{1}{4}(e^2qQ)(1-\eta) \end{aligned} \tag{2.18}$$

$$\begin{aligned} E_0 = E_z &= \frac{\langle \Psi_0 | H_Q | \Psi_0 \rangle}{\langle \Psi_0 | \Psi_0 \rangle} \\ &= -\frac{1}{2}(e^2qQ). \end{aligned} \tag{2.19}$$

For spin-1 nuclei and asymmetry parameter $\eta \neq 0$, three transition frequencies are allowed and derived as [Smith, 1986],

$$\begin{aligned} \nu_+ = \nu_x &= \frac{3}{4}\left(\frac{e^2qQ}{h}\right)\left(1+\frac{\eta}{3}\right) \\ \nu_- = \nu_y &= \frac{3}{4}\left(\frac{e^2qQ}{h}\right)\left(1-\frac{\eta}{3}\right) \\ \nu_0 = \nu_z &= \frac{1}{2}\left(\frac{e^2qQ}{h}\right)\eta. \end{aligned} \tag{2.20}$$

Figure 2.3 illustrates the quadrupole energy levels and allowed transitions for spin-1 nuclei. In the case of axial symmetry (i.e., $\eta = 0$), the energy is doubly degenerated and only one transition is observed with frequency $\nu = \frac{3}{4}\frac{e^2qQ}{h}$. In contrast, when the energy levels are not degenerated (i.e., non-axial symmetric EFG, $\eta \neq 0$), there are three distinct possible transitions. Such a case is observed in the commonly used quadrupolar nucleus, ^{14}N. As mentioned before, these energy splittings are mainly attributable to the interaction of the nuclear quadrupole moment and the EFG created at a molecular level; thus, NQR is highly sensitive to any structural or dynamical changes within the crystal, leading to unique and characteristic parameters for each material. These parameters include the QCC,

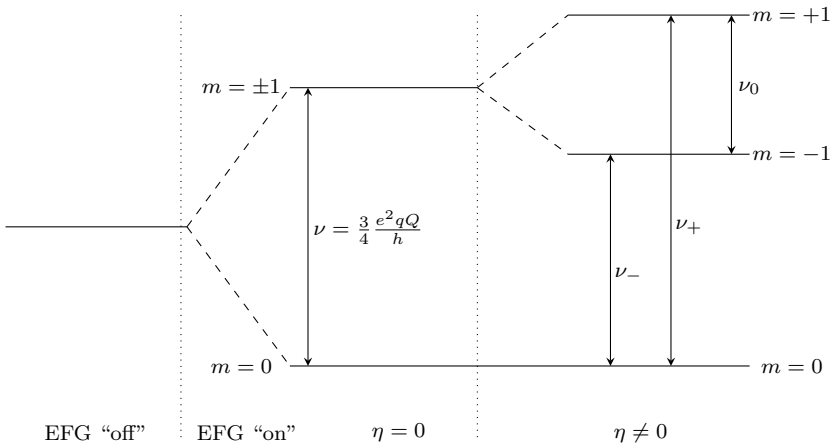

Figure 2.3: Quadrupole energy levels and transitions for nuclear spin $I = 1$.

η and the resonance frequencies [4]. When the EFG parameters are known, the resonance frequencies can be obtained using (2.20). However, in the typical case where the QCC and η parameters are not known, one may have to search to locate the unknown NQR spectral line. The resonance frequencies may infer significant information on the crystalline structure and dynamical properties of the sample. Furthermore, the EFG parameters can be calculated from theoretical derivations [Tate, 2007]. As in NMR, RF radiation is applied to create transitions between the energy levels. This concept is discussed in the following section.

2.4 Radio Frequency Excitation

As in NMR, in a typical NQR measurement, transitions between the energy levels are created from the coupling of the nuclear magnetic moment with a resonant time-dependent magnetic field. That is, the quadrupolar nuclei must be perturbed from their degenerate equilibrium state. Simply, when the sample is enclosed within a solenoid, it experiences a RF oscillating magnetic field of a particular angular frequency. A simple classical view of the effects of RF radiation on the NQR system is described in order to provide an intuitive understanding of the RF excitation. The quantum mechanical approach is beyond the scope of this thesis; however, the principal derivations are included, where appropriate.

[4]Note that η in this Chapter denotes the asymmetry parameter as defined in (2.11).

2.4.1 Rotating Frame of Reference

In the presence of a magnetic field, the nuclear spins tend to precess along its direction with a fixed angle; a precession similar to a gyroscope. A simple illustration of the precession of the nuclear magnetization vector, M, or equivalently, the magnetic moment, $\boldsymbol{\mu}$, is shown in Figure 2.4. This motion is known as the

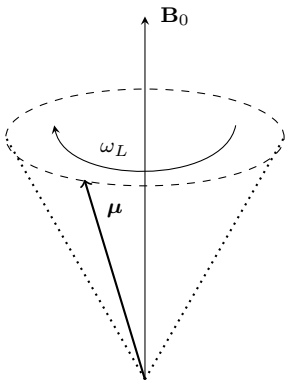

Figure 2.4: Precession of magnetic dipole moment $\boldsymbol{\mu}$ about the $+z$ direction of $\mathbf{B}_0$ field.

Larmor precession and it is controlled by the frequency $\omega_L = \gamma B_0$. Adding all the individual moments, a net component will be created and referred to as the bulk nuclear magnetisation. When other external magnetic fields, such as RF excitation, are applied in the laboratory frame of reference, the motion of the nuclear magnetisation is far more complicated. Thus, the concept of the *rotating frame* of reference is introduced. Let the Cartesian principal axes of the EFG in the stationary laboratory frame, presented by the coordinate axis system $\{x, y, z\}$, with x and y being perpendicular to z and to each other. The rotating coordinate frame will be equivalently denoted as $\{x', y', z'\}$ where $z' = z$. In this frame, x' and y' rotate about the z' axis at an angular frequency ω_{exc}, as illustrated in Figure 2.5. Due to the rotation of the coordinate system, the nuclear spins will experience an effective frequency, $\omega_L - \omega_{\text{exc}}$, where ω_L is the Larmor frequency. The residual field is then given by

$$\Delta B = \frac{\omega_L - \omega_{\text{exc}}}{\gamma}. \tag{2.21}$$

Consequently, when on-resonance (i.e., $\omega_L = \omega_{\text{exc}}$), the B_0 field and the net magnetisation vector, will appear stationary and the effect of this field will be "unseen" ($\Delta B = 0$). Now consider the application of RF radiation. The applied

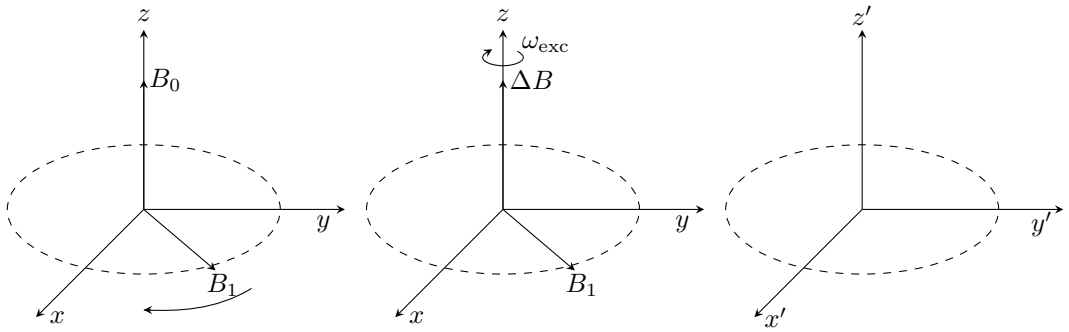

Figure 2.5: The rotating frame of reference.

RF field is linearly polarised and decomposed into two circularly polarised components [Freeman, 1998; Carr and Purcell, 1954]. From these two fields, only one has the effective properties to interact with the nuclear spins. If a RF field, B_1, is applied in short intense pulses of length t_{pw} and rotate about z and along (for instance) the x axis through an angle α, the effective field in the rotating frame is expressed as [Cowan, 2005; Freeman, 1998],

$$B_{\mathrm{eff}} = \sqrt{\Delta B^2 + B_1^2}. \tag{2.22}$$

At exact resonance, the nuclear magnetisation will precess about the effective field at an angular frequency

$$\omega_1 = \gamma B_1. \tag{2.23}$$

This precession may be referred to as *nutation*. The nutation frequency is given by ω_1.

2.4.2 Flip Angle

Following the RF excitation, the nuclear magnetisation rotates towards the $x'y'$ plane, in the rotating frame of reference. The angle between the magnetisation and the z' axis is known as the *flip angle*. A simple diagram is illustrated in Figure 2.6. In NMR or single crystal NQR, the flip angle is expressed as

$$\alpha = \gamma B_1 t_{\mathrm{pw}} = \omega_1 t_{\mathrm{pw}}. \tag{2.24}$$

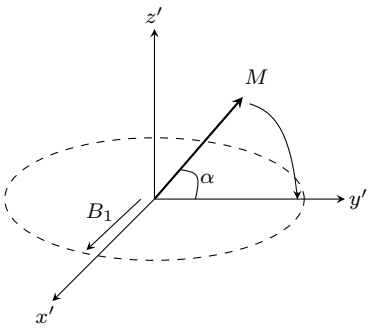

Figure 2.6: Flip angle.

and depends on the intrinsic gyromagnetic ratio of each sample, the B_1 field and the duration of the RF pulse, t_{pw} [Cordier et al., 2005; Canet et al., 2006; Freeman, 1998]. When the RF pulse is turned off, the nuclear spins return to their thermal equilibrium state via the so-called *relaxation processes* (see Section 2.5).

The magnetisation, $M_{x'y'}$, induces a decaying signal in the coil, known as the *free induction decay* (FID) which is governed by the spin-phase memory decay time constant, T_2^*. The maximum intensity of the signal is achieved at an optimum flip angle. Exploiting B_1 and t_{pw} in (2.24) can be one way of determining the optimum value of the nutation angle. In practice, one plots the signal intensity with respect to a range of pulse durations and the observed periodic function (known as the *nutation curve*) is used to obtain the optimum flip angle that maximises the SNR. In a single crystal scenario and under the on-resonance condition, the nutation curve follows a sinusoidal function with maximum signal intensity at an angle of 90°. However, in a polycrystalline sample, the transitions depend on the relative orientation of the B_1 field and its crystalline structure. That is, the RF field and the NQR signal may vary with the orientation of each crystallite axis. Thus, the NQR signal is given by integration over all possible orientations. In a polycrystalline sample, the nutation curve follows a Bessel function with maximum and minimum values at particular pulse durations [Lee, 2002; Cordier et al., 2005; Canet et al., 2006; Youlin and Chahohui, 1996]. In NQR, the optimum flip angle is conventionally referred to as 90°_{eff}. Canet et al. [2006] and Cordier et al. [2005] present the theoretical expressions of the nutation curves in spin-1 nuclei, in the cases of an axially symmetric and arbitrary EFG tensor. Deriving a model of the signal evolution using the density operator [Cantor and Waugh, 1980; Osokin, 1983; Lee, 2002], the nutation curves for the

three transitions of an asymmetric EFG can be expressed as

$$S_x(\omega_{\text{exc}}, t_{\text{pw}}) = A_x \int_0^{\pi} \int_0^{2\pi} \sin\left[\sin\theta\cos\varphi \text{sinc}((\omega_x - \omega_{\text{exc}})t_{\text{pw}})B_1 t_{\text{pw}}\right] \times \sin^2\theta \sin\varphi d\theta d\varphi \quad (2.25)$$

$$S_y(\omega_{\text{exc}}, t_{\text{pw}}) = A_y \int_0^{\pi} \int_0^{2\pi} \sin\left[\sin\theta\cos\varphi \text{sinc}((\omega_y - \omega_{\text{exc}})t_{\text{pw}})B_1 t_{\text{pw}}\right] \times \sin^2\theta \sin\varphi d\theta d\varphi \quad (2.26)$$

$$S_z(\omega_{\text{exc}}, t_{\text{pw}}) = A_z \int_0^{\pi} \sin\left[\cos\theta \text{sinc}((\omega_z - \omega_{\text{exc}})t_{\text{pw}})B_1 t_{\text{pw}}\right] \times \sin\theta\cos\theta d\theta, \quad (2.27)$$

where θ is the angle between the particular principal axis of EFG and the coil axis, and the coefficients A_x, A_y and A_z depend on instrumental factors. The term $\sin\theta\cos\varphi$ defines the coil's orientation with respect to the principal axis system of a crystallite [Canet et al., 2006]. Numerical evaluations of the nutations curves in (2.25) - (2.27), give a maximum signal for a flip angle $\alpha_{\text{eff}} \approx 119°$ [Canet et al., 2006; Rowe and Smith, 1996; Lee, 2002; Miller, 2007]. In some studies however, the optimum flip angle of a refocussing RF pulse [5] has been found to be near 150° [Miller et al., 2009; Sauer and Klug, 2006; Malone et al., 2011]. For every material, the optimum flip angle may vary depending on the distribution of the NQR frequencies (i.e., line broadening) caused either due to EFG inhomogeneities or dipolar interactions [Sauer and Klug, 2006]. Since for a polycrystalline sample, the $\{x, y, z\}$ directions play the same role, the flip angle is the same for the three transitions for a certain value of pulse length and RF power. Furthermore, one can derive the nutation curve for the case of axial symmetry with $\eta = 0$ and $\varphi = 0$ [Canet et al., 2006]. This yields,

$$S_{\eta=0}(\omega_{\text{exc}}, t_{\text{pw}}) = A_0 \int_0^{\pi} \sin[\sin\theta \text{sinc}((\omega_{\text{exc}} - \omega)t_{\text{pw}})B_1 t_{\text{pw}}] \sin^2\theta d\theta. \quad (2.28)$$

In this case, the maximum signal intensity occurs at $\alpha_{\text{eff}} \approx 101°$, for spin-1 nuclei. Equations (2.25) - (2.27) illustrate the dependence of the signal intensity on the parameters B_0, t_{pw}, and off-resonance frequency $\Delta\omega = \omega_q - \omega_{\text{exc}}$. Accurate knowledge of those parameters enable the accurate estimation of the expected

[5] A refocussing RF pulse of the pulsed spin-locking (PSL) sequence (see Section 2.6.2).

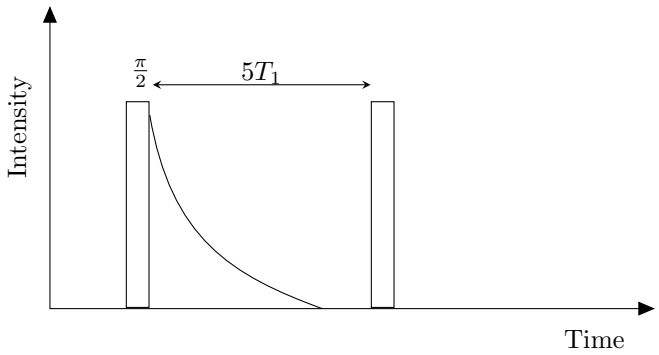

Figure 2.7: Free Induction Decay.

signal intensity. A significant part of this thesis focuses in optimising the detection performance in the presence of off-resonance excitation, where in most cases, this is created when the sample temperature is only approximately known. In Chapter 4, a theoretical expression of the signal intensity with respect to the off-resonance frequency is exploited in the current state-of-the-art detection algorithms to improve the performance.

2.5 Nuclear Relaxation

In NQR, several mechanisms contribute to the relaxation of the system. Once the NQR signal is excited by a RF pulse, instead of persisting indefinitely, it deteriorates over time via various relaxation processes. The time constants that describe the consequent incoherence in the spin motion are characteristic for each nucleus, making NQR a perfect candidate for detection applications. During relaxation, energy is exchanged due to either interactions of the spin dipoles with their surrounding environment or with themselves.

When a single RF pulse is used for sample excitation, the resulting signal is a FID. This decay is characterised by the spin-phase memory time constant, T_2^*, and the signal intensity is proportional to e^{-t/T_2^*}. Figure 2.7 illustrates the FID in a single pulse experiment. The inhomogeneous nature of the material due to temperature gradients, sample impurities or imperfections in the crystal lattice, create fluctuations in the EFG throughout the sample which leads to loss of the spins' phase coherence. Fourier transformation of the FID signal (in time domain) yields the spectral lineshape, typically being modelled as a Gaussian or Lorentzian function [Rabbani et al., 1995; Song et al., 2000; Smith et al., 2011; Miller, 2007;

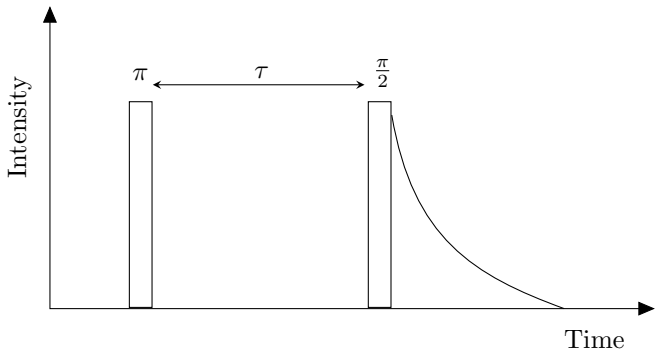

Figure 2.8: Measurement of T_1 relaxation constant using the Inversion-recovery pulse sequence.

Tate, 2007]. [6] However, the use of a more general lineshape model such as a Voigt function, has been shown to be beneficial [Adalbjörnsson and Jakobsson, 2010; Marshall et al., 1997; Malone and Sauer, 2014b]. For the purpose of this thesis, a Lorentzian lineshape is assumed, with full-width-at-half-maximum (FWHM) given by $\Delta\nu_{1/2} = 1/\pi T_2^*$ [Smith et al., 2011; Mikhaltsevitch and Rudakov, 2004]. In a NQR experiment, there is a "dead time" after the excitation of a RF pulse, during which neither a RF pulse is applied, nor the signal is acquired. Signal acquisition immediately after the RF pulse may lead in pulse breakthrough with much greater intensity than the detected signal and thus, saturating the receiver (see Section 3.1.3).

The spin-lattice relaxation describes the return of the nuclei to their thermal equilibrium state and the process is governed by the time constant, T_1. When a RF pulse is applied, the nuclear magnetisation (at Boltzmann equilibrium) along the $+z$-direction, is perturbed [Freeman, 1998]. The interactions of the spins with the crystal lattice produce an exchange of energy within the spin system and the so-called *longitudinal* magnetisation (M_z) relaxes back in thermal equilibrium. In other words, the energy of the spins is transferred into the thermal energy of the molecular and atomic motions in the lattice. In a typical NQR experiment, a wait time between successive RF excitations is necessary to allow the spin system to fully relax and reach thermal equilibrium with the surroundings. By convention, one should wait for a $5T_1$ delay, before applying another RF pulse [Rowe and Smith, 1996; Smith, 1995]. A common method used for measurements of the T_1

[6] In NMR, the *general lineshape theory* is used for determining the spectral lineshape function [Mehring, 2012]. The quantum mechanical description of the FID is beyond the scope of the thesis, but the interested reader is referred to Lowe and Norberg [1957].

relaxation in materials is the Inversion-recovery pulse sequence [Freeman, 1998; Slichter, 2013; Ferrari and Canet, 2009]. A diagram of the inversion-recovery sequence is illustrated in Figure 2.8. The pulse sequence, $(\pi - \tau - \pi/2)$, begins when a 180° pulse rotates the longitudinal magnetisation vector along $-z'$ axis, followed by a period where spin-lattice relaxation occurs. Since the signal is created when the magnetisation is in the $\{x'y'\}$ plane, a 90° pulse is applied before full relaxation, driving the vector into the $\{x'y'\}$ plane. Finally, the magnetisation rotates back to equilibrium and a FID is generated.

Another relaxation process is the spin-spin relaxation, also known as the transverse relaxation. Application of a RF pulse drives the transverse magnetization to rotate about the $\{x'y'\}$ plane. This mechanism is a measure of the true decay of the transverse magnetisation (M_{XY}) [7], and it is governed by the spin-spin relaxation time, T_2. As the name suggests, the energy is transferred from one spin to another, where in solids T_2 is due to dipole-dipole interaction. The relaxation constant, T_2, is measured using a two-pulse method, $(90° - \tau - 180°)$, in which a single echo is formed by reversing the dephased spin isochromats (see Section 2.6.1). Conventionally, T_2 is determined by plotting the echo intensity with respect to an increasing pulse spacing.

Due to the inhomogeneous nature of a sample, broadening of the lineshape may occur as a result of the distribution of EFGs at the nuclei across the crystal. Thus,

$$T_2^* \leq T_2, \tag{2.29}$$

where $T_2^* = T_2$ in a homogeneous pure crystal [Miller, 2007]. Note that one may describe the observed lineshape as a convolution of the inhomogeneous broadening function governed by T_2^*, and the natural broadening governed by T_2. In Smith et al. [2011], the authors assume a Lorentzian lineshape and express this convolution as

$$\frac{1}{T_2^*} = \frac{1}{T_{2(inhom)}} + \frac{1}{T_2}. \tag{2.30}$$

[7] In NMR, the transverse magnetisation is conventionally denoted as M_{XY}. Herein, this quantity is classically obtained in the rotating frame of reference, x', y', z', but as a rule of thumb, the subscript XY is used.

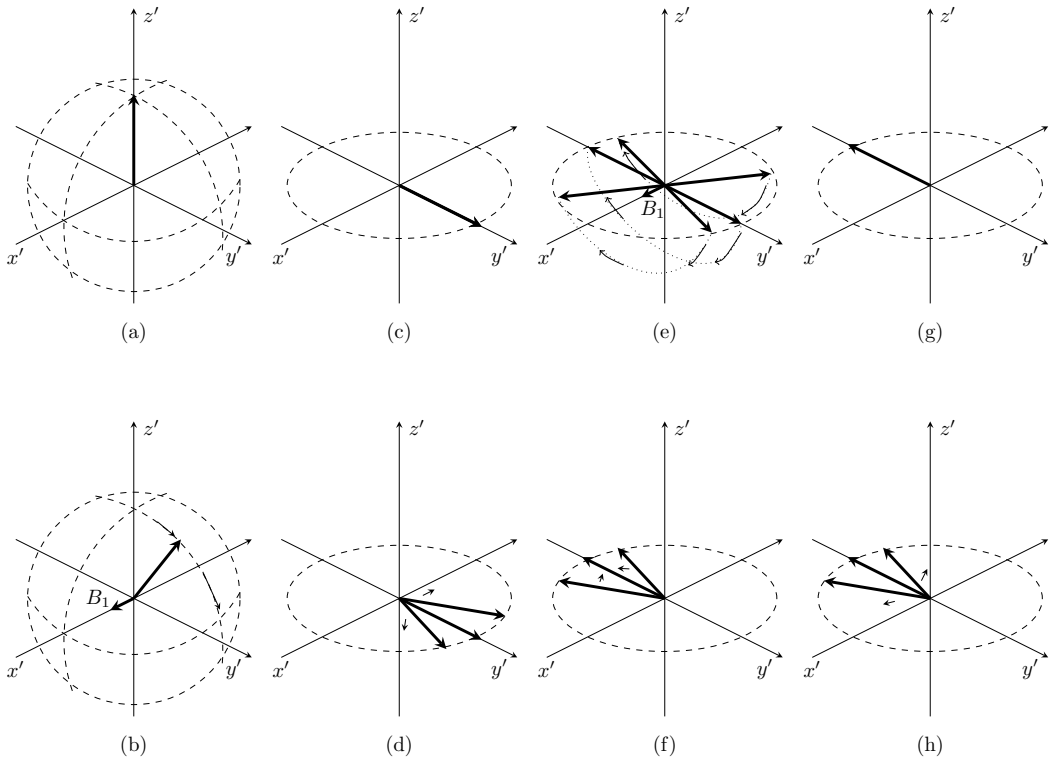

Figure 2.9: Formation of the Hahn Echo.

Exploiting the temperature dependence of the relaxation parameters for a specific material and under a certain temperature range, one may infer important information on the dominating processes in a spin system, at the molecular level.

2.6 NQR Signals

2.6.1 Hahn Echo

The concept of spin echoes was developed in NMR by Hahn [1950]. Application of two RF pulses separated by a duration τ, generates an echo whose peak is detected at 2τ. A classical representation of the spin echo phenomenon is illustrated in Figure 2.9. If a $\pi/2$ pulse is applied along the x' axis, the net magnetisation rotates about the effective field (in z axis) and the spins are tipped in the y' axis (Figure 2.9(a-b)). At the end of the $\pi/2$ pulse, the magnetisation aligns along the $x'y'$ plane (Figure 2.9(c)). Relaxation processes mainly caused by the inhomogeneous nature of the sample, induce a distribution of EFGs and each individual spin experiences a resonance frequency. Thus, the "isochromats" lose their phase

coherence and begin to fan out slowly [Carr and Purcell, 1954] (Figure 2.9(d)). The isochromats with frequencies higher than the mean resonance frequency will rotate ahead of the net magnetisation in the $x'y'$ plane, while those with lower frequencies will fall behind it; that is, the magnetisation of the isochromats precesses away from the net magnetisation. At time τ, a "refocussing" π pulse is applied along the x' axis and the refocused isochromats will be aligned along the $-y'$ axis,. This time, they will precess towards the net magnetisation (Figure 2.9(e-f)). When the isochromats are perfectly reclustered, the peak of an echo is formed at $t = 2\tau$ (Figure 2.9(g)). Then the maximum signal intensity begins to decay as the isochromats lose coherence again (Figure 2.9(h)). Depending on the phase of the refocusing RF pulse, the sign of the formed echo may be positive or negative. For pulses of the same phase, a negative echo is produced. In contrast, pulses with different phases form positive echoes [Rowe and Smith, 1996]. An echo may be seen as two FIDs, back to back.

2.6.2 Pulsed Spin-Lock Sequence

Multiple-pulse sequences are commonly used in NQR measurements due to the significant enhancement of the SNR. In detection applications, excitation of the spin system with consecutive RF pulses generates a series of NQR echoes that can be summed to enhance the signal intensity. A well known multiple pulse sequence was developed by Carr and Purcell, where a preparatory pulse, 90°_{eff}, is applied followed by a series of refocusing pulses, 180°_{eff}, separated by 2τ [Carr and Purcell, 1954]. Peaks of echoes are detected between this period every $n(2\tau)$, with n being an integer. As described in Section 2.6.1, after the end of the first refocusing pulse, the isochromats begin to fan out. Following a 2τ period, another refocusing pulse is applied creating a second echo of lower intensity, and so on. The echo train cannot be sustained indefinitely as magnetisation is lost due to relaxation processes. The Carr-Purcell pulse sequence induces a train of echoes of opposite signs. A modification in this sequence developed by Meiboom and Gill [1958], generates echoes of the same sign (positive) where the preparatory pulse is phase shifted by 90°_{eff} relative to the phase of the 180°_{eff} pulses. The functionality of both sequences is the same and thus, one commonly refers to the Carr-Purcell-Meiboom-Gill (CPMG) pulse sequence.

Marino and Klainer [1977] introduced the concept of multiple pulse sequences that create the so-called "spin-lock" effect. The benefit of this modified pulse

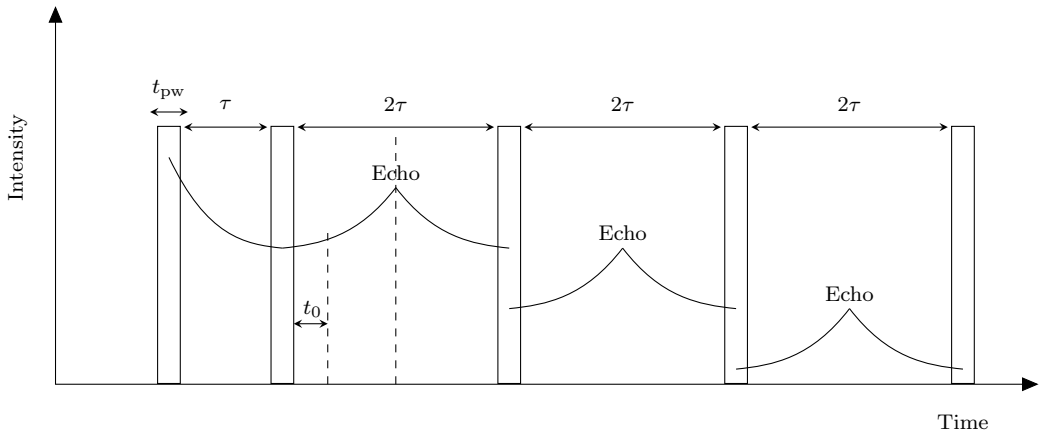

Figure 2.10: The NQR signal formed using a PSL sequence.

sequence – spin-lock spin-echo (SLSE) – is the significant increase in the SNR, as compared with the single spin-echo sequence. In NQR, the pulsed spin-locking approach is often adopted. As in CPMG, by applying a series of RF pulses, the net magnetisation is spin-locked in the effective field and its decay is governed by the effective relaxation time constant $T_{2e} > T_2$, when $\tau \leq T_2$ [Marino and Klainer, 1977]. Originating from the SLSE sequence, several versions that create the same spin-lock effect have been derived. Some examples include the phase cycled sequence [Rudakov and Mikhaltsevich, 2003], the phase alternated pulse sequence [Osokin, 1982] and strong off-resonance comb [Kim et al., 1992; Konnai et al., 2008]. Such a pulse sequence is commonly referred as pulsed spin-locking (PSL) sequence. The T_{2e} constant is usually computed by fitting the decay of the echo peaks at time t, using

$$M(t) = M_0 e^{-t/T_{2e}}. \tag{2.31}$$

The PSL sequence uses 90°_{eff} pulses, with a preparatory pulse $\theta^p_{\angle p}$ being phase shifted by 90° with respect to a train of refocusing pulses, $\theta^r_{\angle r}$. This is simply written as

$$\theta^p_{\angle p} \; - \; (\tau \; - \; \theta^r_{\angle r} \; - \; \tau)_M, \tag{2.32}$$

where M denotes the number of RF pulses or formed echoes. Figure 2.10 is an illustration of the PSL sequence. One must note that T_{2e} is not a fundamental

relaxation time, but it is introduced by the combination of both T_1 and T_2 relaxation constants, due to the fact that the resulting echoes are a mixture of Hahn and stimulated echoes [Smith et al., 2011]. The stimulated echoes are generally created from the application of three or more RF pulses [Burstein, 1996]. Along with the Hahn echoes, a stimulated echo is formed from spins that refocus from the combination of three pulses [Burstein, 1996]. One can choose the appropriate pulse sequence timings in order to isolate and record a stimulated echo. According to Smith et al. [2011], the stimulated echoes introduce the T_1 contribution to T_{2e}.

The choice of the RF refocusing pulse spacing, τ, is important for optimising the SNR in the PSL pulse sequence. The effective relaxation constant depends on τ and it is usually observed to decrease with increasing τ. For a shorter τ, the T_{2e} increases, enabling the acquisition of more echoes and SNR enhancement [8]. A non-ideal short τ requires shorter acquisition times that may result in truncated echoes and reduction of the spectral resolution. Thus, there are limitations in the choice of τ and one should compromise between those parameters. Another factor of consideration is the time required for the resonator to "ring down" after the RF pulses (See Section 3.1.3). One allows a dead time before the echo peak is detected [Miller, 2007]. Several ^{14}N NQR studies report on the dependence of T_{2e} on τ. The study by Marino and Klainer [1977] refers to the $\nu_- = 3757$ kHz line of sodium nitrite at 77 K and under the conditions $\tau \leq T_2$ and $T_2 > T_{2e} > T_1$, then $T_{2e} \propto \tau^{-5}$. Similarly, for the $\nu_+ = 4640$ kHz spectral line of the same material at 295 K, $T_{2e} \propto \tau^{-1.3}$ when $T_2^* \leq 2\tau \leq T_2$ and $2\tau \leq T_2^*$ [Mikhaltsevitch and Rudakov, 2004]. Another study found a different dependence among the three transitions of sodium nitrite ν_+, ν_-, ν_0, such as $T_{2e} \propto \tau^{-0.18}, \tau^{-0.37}$ and $\tau^{-0.33}$, respectively [Malone et al., 2011]. In a PSL sequence, the optimum number of echoes to maximise the SNR is given by [Marino and Klainer, 1977; Gregorovič and Apih, 2008],

$$M_{\text{opt}} = \frac{1.25 T_{2e}}{2\tau}, \tag{2.33}$$

and if one sums the coherent echoes, the SNR is enhanced by a factor

[8] Each echo will be more intense, so the SNR is increased even if the number of echoes is kept the same.

$$\mathrm{SNR}_{\mathrm{opt}} = \frac{0.64\sqrt{\frac{2\tau}{T_{2e}}}}{(1 - e^{-\frac{2\tau}{T_{2e}}})}. \tag{2.34}$$

2.7 NQR characteristic parameters

The NQR signal is characterised by the following parameters:

- resonance frequency
- quadrupole coupling constant
- asymmetry parameter
- signal amplitude
- spectral linewidth
- echo train decay
- spin-spin relaxation constant
- spin lattice relaxation constant

In NQR, every one of those parameters is exploited to infer significant information in several areas including explosives detection, authentication of materials, pharmaceutical analysis such as quality control and detection of polymorphs [Latosińska, 2007a,b; Barras et al., 2012a]. The rich structure of the NQR signal provides unique features that are characteristic to each material. Therefore, it is important to express the dependence of those parameters on the pulse sequence timings and environmental factors for improved detection and authentication performance. Broadening of the spectral linewidth is due to several reasons. These include dipolar coupling, T_2 relaxation and inhomogeneous broadening governed by T_2^*, with the latter being the most dominant [Smith et al., 2011; Gregorovič, 2015; Dolinšek et al., 1994; Malone et al., 2011; Malone and Sauer, 2014b; Song et al., 2000]. The ability to identify the contributions of the linewidth broadening is crucial for detection of substances. Different irregularities, impurities and crystal imperfections lead in inhomogeneous broadening [Youlin and Chahohui, 1996; Ferrari and Canet, 2009; Buess and Caulder, 2004]. The spectral linewidth can therefore provide valuable facts about the crystalline profile of a material. Chapter 5 includes a thorough discussion on the NQR parameters and their contribution in characterising the physico-chemical properties of a crystal.

It is well known that NQR is intrinsically quantitative. The relative areas under the resonance peaks are proportional to the relative abundance of nuclei in

the sample [Tate et al., 2009; Perez et al., 2005; Barras et al., 2012b, 2013; Balchin et al., 2005]. Typically, the approach used to determine the signal amplitude is by integration. The drawbacks of this method is that an interval of integration must be specified for every spectral line and inconsistent choice may induce errors. This is also limited in low SNR scenarios [Somasundaram, 2007]. Previously proposed models of the NQR responses have been derived and used to estimate the complex amplitudes, overcoming the aforementioned issues [Somasundaram et al., 2007; Jakobsson et al., 2006]. However, the estimation accuracy will depend on how realistic the models are. Commonly, frequency modulated pulses are used to ensure an approximately flat excitation over the selected frequency region; in this way, one assumes that the multiple lines of a material are excited equally [Somasundaram, 2007]. Mefed [2015] reports on the effect of random electronic paramagnetic impurities on the signal intensity and relaxation parameters for ^{14}N NQR of RDX and TNT. The main effect of those impurities is the reduction of the nuclei which leads in attenuation of the observed signal; there was no effect on the NQR relaxation parameters. Moreover, the signal amplitude is affected by hardware equipment such as the quality factor of the coil and the bandwidth of the quarter-wave circuitry (see Section 3.1.3). One specifies the hardware requirements wisely to ensure a high enough SNR. Also, many authors note that the generated noise may be well modelled and used as an approach to invert the effect of the receiver hardware [Somasundaram, 2007; Jakobsson et al., 2006]. Another factor that strongly influences the signal amplitudes are the so-called off-resonance effects which are generally induced due to the uncertainty in the sample's temperature. More details are discussed in Sections 2.7.1 and 2.7.2.

One of the most appreciable environmental factor that affects the NQR parameters is temperature. A vast majority of research has been done in determining the dependence of the NQR relaxation parameters and frequencies on temperature.

2.7.1 Temperature Effects

In NQR detection and identification, the quadrupolar frequency is used as the primary signature of the material. However, the frequency dependency on the temperature may cause inaccuracy in estimations if the temperature is not perfectly known. The quadrupolar frequencies are highly sensitive in variations in the crystal structure and molecular dynamics. When the sample temperature

varies, molecular torsional vibrations and hidden rotations are induced, and disturbances to the charge distribution within the nucleus create an averaging of the EFG [Latosińska, 2007a; Ramu et al., 2010]. Thus, shifting of the spectral lines is observed. This dependency is important in a chemical perspective, as one may extract information about the torsional motions of the molecules and phase transitions of polymorphic materials [Perez et al., 2005; Woessner and Gutowsky, 1963; Haas and Marram, 1965; Seliger et al., 2005]. In NQR, the change of the frequency with temperature is often observed to be linear for modest temperature ranges; more precisely, higher temperatures tend to increase the amplitudes of the molecular vibrations leading to a decrease in the frequencies. Equivalently, the QCC and asymmetry parameters follow a linear dependency on the temperature [Ramu et al., 2010; Shinohara et al., 2011; Chihara et al., 1968; Shinohara et al., 2012a]. Several formulae that describe this dependency have been suggested in previous works, such as the exponential dependence based on Bayer [1951] and Kushida et al. [1956]. However, these models are normally approximated by simpler linear formulations [Shinohara et al., 2011, 2012a; Jakobsson et al., 2006].

Temperature variations also influence the NQR relaxation parameters. The vast majority of studies report on the temperature dependence of the spin-lattice relaxation constant due to the high sensitivity in the dynamic structure of a solid material. Measurements of T_1 are useful in the interpretation of the molecular dynamics and relaxation mechanisms [Smith et al., 2011; Latosińska, 2007a; Woessner and Gutowsky, 1963; Chihara and Nakamura, 1980; Smith, 1986]. In a typical analysis, T_1 measurements are plotted against temperature and fitted to an Arrhenius based equation of the form

$$T_1 = Ae^{E_\alpha/RT}, \tag{2.35}$$

where E_α is an activation energy. The logarithmic form of (2.35) is then expressed as

$$\ln(T_1) = \ln(A) + \frac{E_\alpha}{R}\left(\frac{1}{T}\right), \tag{2.36}$$

and the slope of such a plot determines the activation energy over certain temperature ranges from where different molecular mechanisms dominate T_1. Furthermore, spectral line broadening (i.e., shortening of T_2^*) may be observed with

increasing temperature. In the study of Smith et al. [2011], a significant broadening of the linewidth was observed in ^{14}N of RDX for temperatures above 305 K. Similar dependencies are also reported for T_2 and T_{2e} and can also be described by (2.35) and (2.36) [Smith et al., 2011; Mefed, 2015; Woessner and Gutowsky, 1963].

2.7.2 Off-resonance excitation

In general, the maximum signal is detected when the excitation frequency matches the quadrupolar frequency; an effect known as the *on-resonance condition*. This happens when the excitation RF pulse is applied along the x'-axis in the rotating frame of reference, causing the net magnetisation to rotate about the induced effective field and the nuclear spins flip towards the y'-axis, aligning in the $x'y'$ plane. Every time the aforementioned frequencies do not coincide, the so-called *off-resonance effects* occur [Buess et al., 1994; Kim et al., 1992]. Instead of aligning in the $x'y'$ plane, the magnetisation starts to follow a more complicated path. The greater the off-resonance effect (i.e., the bigger the difference between the excitation and quadrupolar frequencies), the less the magnetisation aligns in the $x'y'$ plane, with the spins rotating in various angles with respect to the RF pulse. Thus, the influence of the effective field seen by the nuclear spins is less significant. Also, the amount of rotation of the magnetisation vector depends on the duration of the applied RF pulse (that is, to the RF field strength). If the pulse width is short compared to the offset frequency, the variation in the signal amplitude is reduced. However, high power is required to excite a non-selective broader range of frequencies. This is useful in cases of excitation of multiple frequency lines. In practice, operations at lower power is preferred. In NQR, several studies proposed the application of composite pulses which consist of a group of pulses of different phase and duration, in order to compensate for EFG inhomogeneities and off-resonance effects [Miller, 2007; Guendouz et al., 2012; Mikhaltsevitch et al., 2004b; Ramamoorthy et al., 1993]. Using a PSL sequence, the NQR response varies periodically with the off-resonance frequency with characteristic minima and maxima and with the period depending on the spacing of the refocusing pulses. Further information is discussed in Chapter 4.

2.8 Overview of Advanced Signal Processing in NQR

Over the last decade, several NQR data acquisition techniques and detection algorithms have been proposed. Many approaches aim to overcome many of the limitations that the NQR technique faces. The main concern in NQR is the overall low SNR due to the low frequencies of the quadrupolar nuclei [9], RF interference (RFI) [10] and spurious signals due to piezoelectric and magnetoacoustic ringing. Repeated measurements are commonly performed and the signals are added coherently to increase the SNR.This section provides an overview of some of the current state-of-the-art advanced signal processing algorithms used in conventional NQR for detection and authentication purposes, that fully exploit the rich structure of the NQR signal by implementing more realistic models. Some of the features of the current algorithms include:

- exploit the signal structure
- exploit the temperature dependence of the spectral line
- robustness in uncertainties in the assumed amplitudes
- exploit polymorphic properties of materials
- detect multiple polymorphs
- identify mixtures
- reject and cancel RFI

2.8.1 Signal Models

In Jakobsson et al. [2006] and Malcolm-Lawes et al. [1999], the authors developed a model of the noiseless FID, assumed to be a sum of K damped sinusoids,

$$y(t) = \sum_{k=1}^{K} \alpha_k^f e^{(i\omega_k(T)-\beta_k)t} + \upsilon(t), \tag{2.37}$$

where $t = t_0, \ldots, t_{N-1}$ is the sampling time, starting at $t_0 \neq 0$ to allow for the dead time between the center of the RF pulse (assumed to be at zero time) and

[9] The weakness of the NQR signal depends on the quadrupolar isotope under study. For instance, ^{14}N has a very weak signal, as opposed to ^{35}Cl, ^{79}Br and ^{127}I.

[10] RFI is more pronounced during unshielded NQR measurements.

the first sample. Furthermore, α_k^f, ω_k and β_k [11] denote the complex amplitude, the resonance frequency and the damping constant of the k^{th} spectral line, respectively. The additive coloured noise is denoted as $\upsilon(t)$ and often it can be modelled using a low order autoregressive model [Jakobsson et al., 2006; Tan et al., 2004]. The model includes the dependency of the frequency on the sample's temperature, T; a relation normally modelled as a linear function [12]. Thus, if the temperature shifting functions are known, one uses the temperature as a detection variable [Jakobsson et al., 2006]. A Lorentzian NQR lineshape is assumed which is beneficial as the resonance may be modelled as an exponential damped sinusoid. However, there are cases where a Gaussian or a convolution of both Gaussian and Lorentzian lineshapes occurs, depending on the polycrystalline sample [Rabbani et al., 1995; Adalbjörnsson and Jakobsson, 2010; Malone and Sauer, 2014a].

As discussed in Section 2.6.1, a Hahn echo may be seen as a FID, back to back. Thus, an echo may be well modelled as being symmetric about the echo center, such as [Somasundaram, 2007],

$$y(t) = \sum_{k=1}^{K} \alpha_k e^{-\beta_k |t-\tau| + i\omega_k(T)t} + \upsilon(t), \tag{2.38}$$

with $t = t_0, \ldots, t_{N-1}$ being the echo sampling time. The single echo model in (2.38) does not account for the loss of magnetisation over the entire echo train. Somasundaram et al. [2007] proposed a model for the m^{th} echo obtained using a PSL sequence, expressed as,

$$y(t,m) = \sum_{k=1}^{K} \alpha_k e^{i\omega_k(T)t - \beta_k|t-\tau| - (t+2\tau m)\eta_k} + \upsilon(t), \tag{2.39}$$

where α_k and η_k [13]denote the complex amplitude and echo train damping parameter, respectively.

Furthermore, NQR permits identification of different polymorphic forms of a crystal due to the variations in their crystal lattice [Latosińska, 2007a; Latosińska

[11]The damping constant, β_k, is equivalent to the spin-phase memory decay time constant, T_2^*; $\beta_k = D_w/T_2^*$, where D_w is the dwell time.

[12]More details are included in Chapter 4.

[13]The damping constant, η_k, is equivalent to the effective relaxation time constant, T_{2e}; $\eta_k = D_w/T_{2e}$.

and Latosińska, 2011; Balchin et al., 2005]. The previous proposed models allow detection from a single polymorph. A model that was designed to include the responses from multiple polymorphic forms of the sample was proposed by Somasundaram et al. [2008d] and Butt et al. [2008b], and expressed as

$$y(t,m) = \sum_{p=1}^{P} \gamma_p + y^{(p)}(m,t) + \upsilon(t), \tag{2.40}$$

where γ_p is the proportion of the p^{th} polymorph and $y^{(p)}(m,t)$ is defined as in (2.39).

2.8.2 Detection algorithms

Several parametric algorithms implement the proposed NQR signal models described above, which exploit the maximum amount of prior information about the NQR signal. The echo train approximate maximum likelihood (ETAML) algorithm developed by Somasundaram et al. [2007], is derived using the echo model in (2.39). The output is a generalised likelihood ratio test (GLRT) which when compared to a preset threshold value, it determines the acceptable probability of false alarm. The ETAML algorithm has its foundation in the approximate maximum likelihood (AML) algorithm by Jakobsson et al. [2006], implemented using the echo model in (2.38). Both of those algorithms were extended to form their frequency selective counterparts (i.e., FSAML and FETAML), which consider an expected frequency range for the NQR signal [Somasundaram et al., 2007; Jakobsson et al., 2005b]. In comparison with conventional signal processing methods, such as the Fourier Transform (FT), these algorithms exploit valuable information about the signal; thus, the accuracy of the unknown parameters under certain noise conditions is higher. Moreover, Gregorovič and Apih [2009c] implemented the model in (2.39) along with a matched filter. Note that the AML, FSAML, ETAML and FETAML algorithms assume that the complex signal amplitudes are fully known, to within a multiplicative constant. However, in practice, many factors influence the amplitude during a measurement. The algorithms derived by Somasundaram et al. [2008a] allow an uncertainty in the signal amplitudes. The robust echo train approximate maximum likelihood (RETAML) algorithm incorporates prior knowledge of the complex amplitudes and allows for uncertainties

in this knowledge. The frequency selective version of RETAML is the FRETAML [Somasundaram et al., 2008a]. The least squares echo train approximate maximum likelihood (LSETAML) algorithm is similar to ETAML, but with the additional step of estimating the complex amplitude vector and treating it as fully unknown with no a priori information considered. Again, the frequency selective version of LSETAML is expressed as FLSETAML [Somasundaram, 2007]. Using the model of the polymorphic forms of the NQR signal, the ETAML was extended to utilise the polymorphic structure of the materials. The hybrid echo train approximate maximum likelihood (HETAML) detector and its frequency selective counterpart (FHETAML) were formed [Somasundaram et al., 2008d]. These algorithms allow multiple polymorphs to be exploited even if the compounds are different. The FHETAML algorithm was updated to allow for uncertainties in the assumed signal amplitudes, resulting in the robust estimation of multiple polymorph QR signals (REMIQS) [Butt et al., 2008a]. Another approach in NQR is the so-called stochastic NQR, which as opposed to conventional NQR, it uses a train of low power RF pulses of random phases and amplitudes [Somasundaram et al., 2008c; Barras et al., 2012a]. Stochastic NQR is useful in applications such as humanitarian demining where man-portable and battery-operated detectors are required. Also, the method is suitable in analysing materials hidden on humans due to application of low power radiation. Despite the lower SNR signals, stochastic NQR is less prone to RFI signals. The subspace-based evaluation of quadrupole resonance signals (SEAQUER) detector was developed by Somasundaram et al. [2008c] and it is based on a matched subspace-type and prewhitening approach, where a substantial reduction on RFI could be achieved. In a typical analysis, one needs to obtain initial estimates of the damping constants, thus, a *priori* knowledge is required. Reminiscent to previous non-parametric estimators [Stoica and Sundin, 2001; Gudmundson et al., 2010], the recent echo train Capon APes average (ET-CAPA) algorithm was introduced by Kronvall et al. [2013] using the whole echo train model in (2.39). ET-CAPA estimates the damping constants for every component within the signal even for an unknown material and enables cancellation of the RFI. Moreover, ET-CAPA is used to form initial estimates of the expected echo decay within each echo and the overall echo train decay [Butt et al., 2014]. An alternative method of obtaining initial estimates of the parameters is the ET-ESPRIT estimator [Gudmundson et al., 2012]. ET-ESPRIT exploits the model in (2.39) and it is statistically efficient. It does

not require any prior knowledge of the typical parameter values but only needs the number of NQR spectral lines. Its corresponding theoretical lower limit, the Cramér-Rao lower bound, was also derived [Gudmundson et al., 2012].

One way of fighting the issues of RFI is to use the frequency selective algorithms discussed above. One may avoid the RFI by selecting only a range of possible frequency grid points. Multiple antennas have been incorporated in many studies due to their ability of RFI rejection [Butt et al., 2008a; Tan et al., 2005; Jakobsson and Mossberg, 2007; Butt and Jakobsson, 2011; Stoica et al., 2007]. Simply, one antenna acquires the NQR signal, while the others measure any background noise and interference, and thus improving the detection. Another approach of RFI cancellation is the use of highly efficient projection algorithms. In conventional and stochastic NQR, secondary data (signal-free data) might be available after the end of an echo train. An interference subspace is formed using this information, to which the signal is projected orthogonally in order to remove the strong RFI signals. Such an approached was introduced in [Somasundaram et al., 2008b]. SEAQUER is used as a projection algorithm. In the presence of mixed NQR signals, the SEAQUER algorithm (subspace-based evaluation of quadrupole resonance signals exploiting robust methods sNQR) is limited. Therefore, the generalised robust evaluation using subspace-based methods of polymorphic quadrupole signals (RESPEQ) detector is formed [Rudberg and Jakobsson, 2011].

In this thesis, the signal amplitude dependence on the off-resonance excitation and pulse sequence timings is exploited for several medicines and the theoretical expression can be used as a general extension in those studies.

Chapter 3

Experimental

In this chapter, a description of the experimental equipment which was used to obtain the data sets for this thesis is provided. The pulse sequence settings are included in each relevant chapter. Initially, in Section 3.1, an outline of the standard NQR hardware system is provided. In Section 3.2, the procedure for stabilisation and monitoring of the temperature within the probe is explained. Section 3.3 describes the experimental equipment and pulse sequence, which was employed to conduct the measurements from several medicines.

3.1 Outline of the NQR hardware

Figure 3.1 illustrates a simplified block diagram of the standard NQR apparatus. The basic hardware of NQR is similar to NMR, but without the requirement of a large external static magnetic field. For NQR systems, the spectrometer functions both as the transmitter and the receiver.

3.1.1 Transmitter Part

In the transmitter section, RF pulses are used for sample excitation at the desired quadrupolar frequency, whereas in the receiver section, the generated NQR signals are detected [Rudakov, 2014; Latosińska, 2007a; Suits, 2006; Miller, 2011]. Depending on the NQR application, the transmitter, RF synthesiser and pulse sequencer within the spectrometer, will produce a series of RF pulses with specific characteristics. A computer controls and programs the timings of the pulse sequences. Often, the RF pulses pass through an attenuator that allows the power

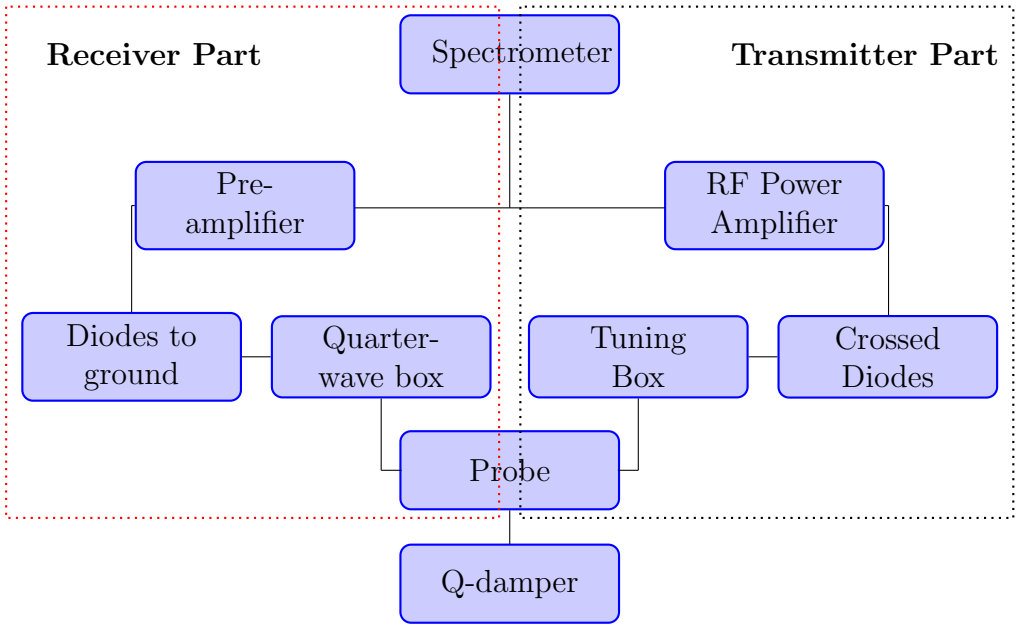

Figure 3.1: Block diagram of the standard NQR hardware.

to be attenuated from 1 – 30 dB, before amplification by the RF power amplifier. Normally, the probe is shielded to eliminate external RFI. For the purpose of this thesis, the data were obtained using a stainless steel lidded shield that enclosed and protected both the RF coil and antenna from any unwanted electric fields. To achieve the optimum SNR, electronics are used to tune the antenna at the correct excitation frequency and match its impedance to the rest of the NQR system. This procedure is carried out prior to a measurement, normally using a signal generator and an oscilloscope. For a tuned system, the amplitude of the reflected power is minimised by adjusting variable capacitors. Figure 3.2 illustrates the circuitry for a variable capacitor in series, another one in parallel and the coil connected to ground, enabling the adjustment of the resonance frequency and impedance of the resonator to be matched for minimal signal loss. The impedance of the coil is given by,

$$Z = \frac{1}{4\pi^2\nu^2 L\, C}, \tag{3.1}$$

where ν (in Hertz), L (in Henries) and C (in Farads) denote the excitation frequency, coil inductance and total capacitance, respectively. As illustrated in Figure 3.1, between the power amplifier and the probe, there is a pair of crossed diodes (in parallel, but in opposite directions), that reduces issues associated with

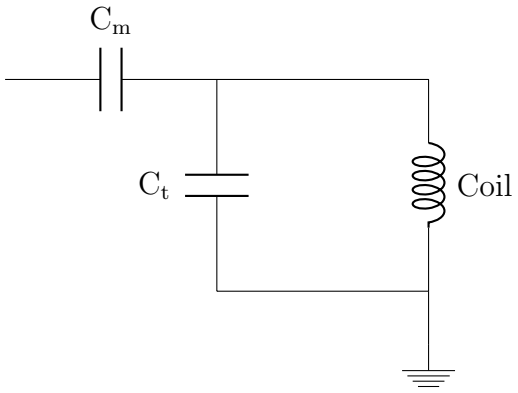

Figure 3.2: Matching and tuning circuitry.

the power amplifier noise. The crossed diodes isolate the probe circuit when the transmission of the RF pulses is off, allowing only the high RF voltages to pass.

3.1.2 Receiver Part

In the receiver part, the RF antenna measures and detects the NQR signals from the materials, followed by signal enhancement at the preamplification stage; this is a crucial step because the signal generated by the magnetisation of the spins is relatively small. In a typical NQR measurement, a single antenna is used to both transmit and receive. The antenna converts the high power of the RF pulses into an excitation energy, which is to be absorbed by the quadrupolar nuclei, while it receives the emitted energy that is measured as a weak voltage. Furthermore, the receiver part consists of cross-diodes to ground and a quarter wavelength ($\lambda/4$) coaxial cable, which are connected between the preamplifier and resonance circuit. Compared to the received NQR signals, the magnitude of the transmitted RF pulses is significantly greater, raising the need to protect the delicate preamplifier during this period. Crossed diodes to ground are employed to satisfy these requirements and act as a good conductor when a RF pulse is transmitted. Meanwhile, the signal current passes directly to the preamplifier when the RF pulse is off. Similarly, the quarter wavelength cable acts as a band pass filter, which allows only the signals with the desired quadrupolar frequencies to pass; thus, the filtering of any unwanted noise protects the preamplifier. This type of transmission lines has a characteristic impedance; in this thesis, $Z_0 = 50$ Ω, which is a typical value in NQR spectroscopy. In designing a quarter wave

box, one may compute the required capacitance for the desired frequencies, using (3.1).

3.1.3 Quality Factor

The form of the NQR coils is typically optimised according to the size and shape of the material of interest. The nature of this technique allows the non-invasive and non-destructive analysis of medicines within the packets. Coils can be built in cylindrical or rectangular geometry, in order for instance, to enclose samples such as standard sized medicine bottles or commercial packets of tablets [Barras et al., 2012b; Tate et al., 2009]. The measurements conducted in this thesis, were obtained using a cylindrical solenoid of fixed pitch. For this solenoid type, the inductance is approximated by

$$L = \frac{\mu_0 \, N^2 \, A}{l}, \tag{3.2}$$

with μ_0, N, A and l denoting the magnetic constant, the number of turns, the cross-sectional area and the solenoid's length. The quality of the coil and its ability to store energy is described by its Quality (Q) factor. The sensitivity of a NQR experiment is correlated to the Q-factor, since the SNR is proportional to $Q^{1/2}$ [Andrew and Jurga, 1987]. In an ideal tuned RF receiver circuit, the Q-factor is defined by

$$Q = \frac{1}{R}\sqrt{\frac{L}{C}} = \frac{2\,\pi\,\nu\,L}{R}, \tag{3.3}$$

were R denotes the resistance (in Ohms) and $\nu = 1/2\,\pi\,\sqrt{L\,C}$. As previously mentioned, the amplitude of the RF excitation pulses is much greater than the generated NQR signals. Thus, the signals are not measured during or immediately after the RF pulse; a *deadtime* is followed while the receiver recovers. This deadtime occurs between the center of the RF pulse and the first acquisition sample. However, for materials with short spin-phase relaxation time, detection of the strongest part of the signal will have been lost during this period. The transmission of the RF pulses stores energy in the coil that dissipates over a period of time; this results in "ringing" that might mask the NQR signal. The time constant associated with the "ring down" of the probe (after the RF pulses), is expressed as [Andrew and Jurga, 1987; Aissani et al., 2014; Tate, 2007; Peshkovsky

et al., 2005]

$$t_r = \frac{Q}{\pi\,\nu_q}, \tag{3.4}$$

with the deadtime given by,

$$t_d = \frac{Q\ln(\frac{A_0}{A_t})}{\pi\,\nu_q} = t_r\ln(\frac{A_0}{A_t}), \tag{3.5}$$

where A_0 and A_t denote the initial voltage and the voltage after the deadtime, respectively. To overcome this problem, one may want to lower the Q-factor of the coil, at the expense of reducing the SNR. The of the Q-factor, improves the SNR, but signals with broader linewidths may not be detected. This phenomenon may occur for samples with low quadrupolar frequencies (order of couple of MHz), with linewidths approaching the bandwidth of the coil. The higher the Q-factor, the narrower the bandwidth, $\Delta\nu$, according to

$$Q = \frac{\nu_q}{\Delta\nu}. \tag{3.6}$$

One strategy to minimise these issues is the use of the so-called Q-damper. It allows the adjustment of the Q-factor for brief and specified periods of time, by employing a fast-controlled switch [Peshkovsky et al., 2005; Somasundaram, 2007]. Furthermore, one way of improving the SNR, is by properly designing the properties of the NQR coil so that the higher the filling factor, the higher the sensitivity. Examples of a Q-damping coil and circuitry are illustrated in Peshkovsky et al. [2005], Tate [2007], and Somasundaram [2007]. For the purpose of the measurements carried out in this thesis, the Q-damping circuity was not required, since this would lower the Q-factor of the coil and reduce the sensitivity. Since the materials of interest lie in a high frequency regime, there is no significant signal loss.

3.2 Temperature Monitoring

Temperature fluctuations during a NQR measurement may lead in significant shifting of the spectral lines. Mismatch of the excitation frequency with the quadrupolar frequency, introduces off-resonance effects (see Section 2.7.2). A big

part of this thesis focuses on the influence of temperature uncertainties on the NQR signal intensity. Therefore, it is essential to create a degree of temperature stability during an experimental procedure. This is achieved with a thermostated probe. In this thesis, the temperature control system used throughout the measurements is based on the system described in Tate [2007]; a control system which is used extensively by the NQR group at King's College London. The system operates as follows: from a temperature controlled bath, silicone oil is flowed through a larger coil of polythene tubing which surrounds the NQR coil within the probe. Using the temperature controller, one could set the temperature at the desired degrees.

Further monitoring of the temperature variations can be achieved using sensitive temperature sensors. An infrared (IF) temperature sensor was manually designed and placed inside the probe, in order to record any significant temperature variability. Figure 3.3(a) shows the IF temperature sensor which was built using one 0.1 µF capacitor, two 4.7 kΩ resistors, an IR sensor 3 V MLX90614 and one Arduino Uno. The MLX90614 IF thermometer, designed by Melexis [2014], allows non contact temperature measurements in the range of -40 to 125° C, with resolution of 0.01° C. The sensor is factory calibrated with a digital PWM and SMBus digital outputs. A diagram of the pins of the sensor is illustrated in Figure 3.3(b) [1]. The IR sensor was positioned to face the area within the probe, and setup to record the temperature (in Celcius) within every second. In order to provide an understanding on how the temperature varies during the replacement of one sample with another, the IR sensor was setup to record measurements of the temperature from the time the lid of the NQR probe is closed. Figure 3.4 illustrates the temperature measurements from the time the lid of the probe was closed, for the duration of 4 hours and 16 minutes. The temperature seems to stabilise within approximately 2 hours and 10 minutes. Therefore, once the sample within the probe is replaced by another one, there must be delay before the activation of the next RF pulse sequence. In Figure 3.4, a small oscillatory behaviour of the temperature is noticed and this is possibly due to the air-conditioning system being switched on and off automatically in the laboratory. The recorded temperature varies within an acceptable ± 0.25 K.

[1] Pin functions; VSS: ground, SCL: serial clock input for two wire communications protocol, PWM (or SDA): digital input/output, and VDD: external supply voltage [Melexis, 2014].

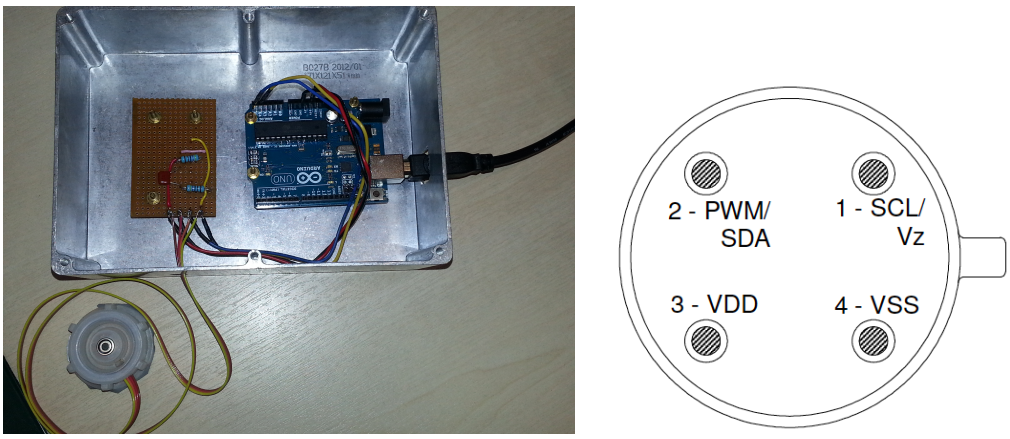

(a) (b)

Figure 3.3: (a) Infrared temperature sensor and (b) diagram of pin (top view) description of the MLX90614 sensor.

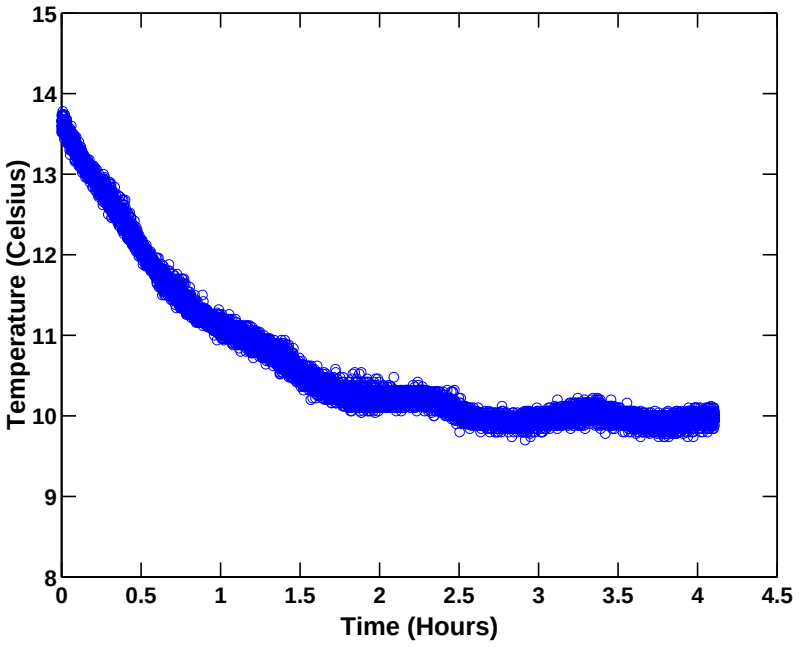

Figure 3.4: Temperature measurements from the IR MLX90614 sensor.

3.3 Experimental Equipment

This section provides the information on the experimental equipment used to obtain the data sets in this thesis. Figure 3.5 shows the NQR laboratory at King's College London, where all the measurements were obtained. A Tecmag Redstone pulsed spectrometer was used to generate the RF pulses, along with a RF Tomco power amplifier (model: BT1000 Alpha-S 1 kW) and a probe. The shielded probe enclosed a cylindrical fixed pitch coil, capable of accommodating standard-sized bottles of medicines and a RF antenna. A separate shielded box was used to house the needed electronics for setting the system to the correct resonance frequency, and matching its impedance with the rest of the electronic devices. The NQR coil was a 100 mm long coil and 55 mm diameter, with 28 turns of Litz wire (see Figure 3.6). The inductance of this coil was measured as $\sim$ L = 33 μH and it was tuned and matched at 50 Ω over the frequency range of $2 - 4.5$ MHz, using the standard $5 - 120$ pF variable capacitors. The Q of the NQR coil was about $180 - 200$, depending on the set resonance frequency. It is important to note that the same coil was used for all the experiments carried on in this thesis, since for the purpose of these measurements, the orientation of the sample within the coil was not relevant. The measurements took several days during which the line frequency was monitored regularly and the temperature of the sample was stabilised as described in Section 3.2. The Tecmag NTNMR software was used to modify and generate the multiple pulse sequences. The measurements in this thesis were obtained using the PSL sequence. As expressed in (2.32), herein, the RF pulse phase cycling was used such as $\angle_p = 0°, 180°, 0°, 180°$ and $\angle_r = 90°, 270°, 270°, 90°$.

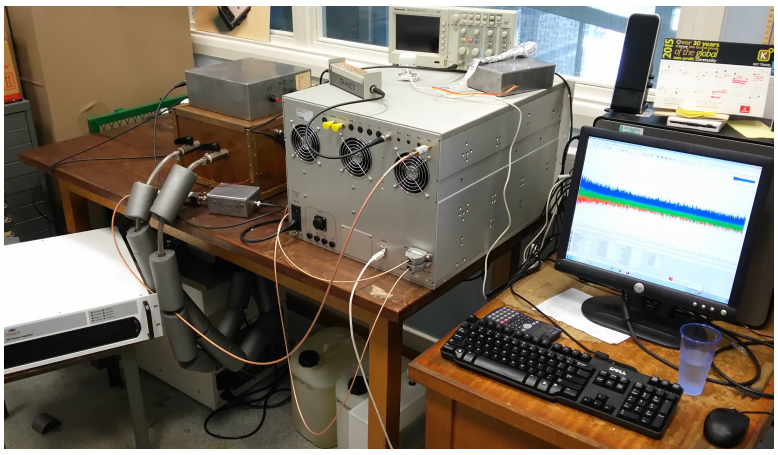

Figure 3.5: NQR laboratory at King's College London.

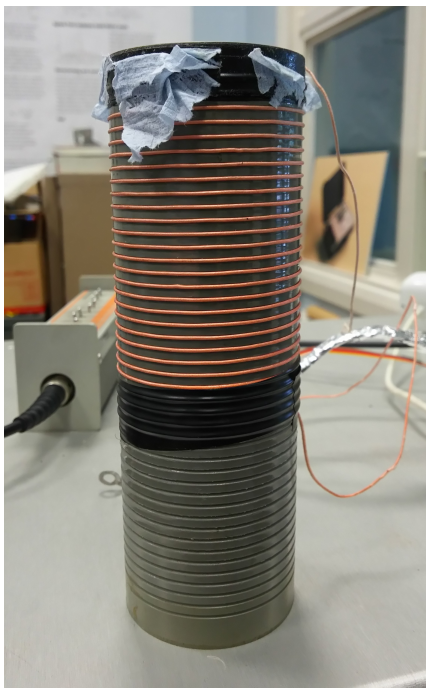

Figure 3.6: Fixed pitch cylindrical solenoid.

Chapter 4

Exploiting Off-resonance Effects

In this chapter, the signal model that exploits the amplitude modulation due to the temperature dependency of the quadrupolar frequency is described. The *off-resonance effects* render the expected signal amplitude to vary significantly. In Section 4.1, an introduction and the motivation for the proposed methodology is given. Sections 4.2, 4.3 and 4.4 introduce the improved NQR signal data model, the offset dependent echo train approximate maximum likelihood (ODETAML) detector and the derivation of the Cramér-Rao lower bound (CRLB), respectively. In Section 4.6, the proposed model is validated from measurements on several medicines. Using simulated NQR data, the performance of the proposed algorithm is evaluated. Finally, the conclusions are drawn in Section 4.7.

4.1 Introduction

The ability to optimise the sensitivity and accurately estimate the NQR signal parameters is essential. The main NQR signal characteristic parameters include the quadrupolar frequency, the spin-phase memory decay time, and the effective relaxation time. In NQR, these parameters are used to build a chemical profile of the examined compound. Factors, including the experimental timings such as the RF pulse width and pulse spacing, influence the NQR parameters. A crucial factor is the temperature variation during the measurement. The dependence of the quadrupolar frequency on temperature variations is reported in several studies [Somasundaram et al., 2007; Gregorovič and Apih, 2008; Ramu et al., 2010; Woessner and Gutowsky, 1963; Mikhaltsevitch and Rudakov, 2004; Jakobsson et al., 2006; Smith et al., 2003]. The frequency shifting functions of

temperature may be well modelled as being linear. An example is illustrated in Somasundaram et al. [2007], for monoclinic TNT in the frequency region of $830-880$ kHz. Even small fluctuations in the temperature may lead in mismatch of the quadrupolar frequency with the excitation frequency. Consequently, the effect of the *off-resonance excitation* is encountered (see Section 2.7.2). Multiple pulse sequences have been proved to substantially improve the effective sensitivity in NQR spectroscopy [Marino and Klainer, 1977; Carr and Purcell, 1954; Gregorovič and Apih, 2008; Rudakov et al., 1997]. As discussed in Section 2.6.2, the benefit of the PSL sequence is the significant increase in the SNR, as compared with the single spin-echo sequence. However, the signal intensity generated by the PSL sequence, exhibits a strong dependence on the off-resonance excitation [Sauer and Klug, 2006; Blauch et al., 1999; Mikhaltsevitch and Rudakov, 2004; Gregorovič and Apih, 2008]. In Mikhaltsevitch and Rudakov [2004], Gregorovič et al. [2009], Osokin [1983] and Gregorovič and Apih [2009b], the authors report on the observed modulation of the amplitude with respect to the off-resonance frequency. In fact, the signal follows a sinc-like function with periodicity due to the RF pulse spacing. Imprecise knowledge of the temperature leads to inaccurate measure of the quadrupolar frequency, ensuring that the expected signal intensity may vary substantially as compared when the on-resonance condition is met. The maximum intensity is achieved once the excitation frequency, ω_{exc}, equals the resonance frequency, ω_k of the k^{th} spectral line. Otherwise, due to finite RF power, the signal intensity decreases when

$$\Delta\omega_k = \omega_k - \omega_{\text{exc}} \neq 0. \tag{4.1}$$

This chapter exploits the theoretical expression of the amplitude modulation as introduced by Gregorovič et al. [2009]. This function is here implemented as an extension to the earlier detection algorithms presented in Jakobsson et al. [2006], Jakobsson et al. [2005b] and Somasundaram et al. [2007]; thus improving the achievable identification performance in the typical case where the temperature of the sample under study is approximately known. In Gregorovič et al. [2009], the model of the steady state amplitude modulation was validated from measurements on the non-explosive compound paranitrotoluene (PNT), and trinitrotoluene (TNT), using ^{14}N NQR and the PSL sequence. PNT has been chosen as a model of TNT, since both materials share the main NQR characteristics. Their major difference is the number of non-equivalent nitrogen nuclei; in the

solid-state, TNT has two crystalline forms or polymorphs, each yielding six non-equivalent nitrogen environments, whereas PNT consists of one nitrogen nucleus.

The earlier detectors, AML and ETAML, and their frequency selective counterparts, FSAML and FETAML, assume the complex amplitudes of the NQR frequency lines to be fully known (see Section 2.8) [Jakobsson et al., 2006, 2005b]. The amplitude modulation function is incorporated as a "feature" in the existing algorithms, forming the offset dependent detection algorithms. An extension upon the earlier presented CRLB in Gudmundson et al. [2012] is introduced to the new data model, allowing one to determine suitable experimental conditions for optimised detection performance, under a given experimental setup and temperature uncertainty. Using real data, the proposed signal model is evaluated. Measurements were obtained from powder sodium nitrite, generic metformin hydrochloride caplets and powder aniracetam. To the best knowledge of the author, no previous data have been previously published on ^{14}N NQR, for metformin hydrochloride and aniracetam. ^{1}H nuclear magnetic resonance spectrometry has been used to detect signals from metformin hydrochloride in commercial tablets [El-Khateeb et al., 1988; Gadape and Parikh, 2011]. The author thanks Dr. Iain Poplett and Dr. Jamie Barras of the King's College London NQR group, for providing information on the ^{14}N NQR resonance frequencies and relaxation parameters of metformin hydrochloride and aniracetam.

4.2 NQR data model

As discussed in Somasundaram et al. [2007], the m^{th} echo of an echo-train signal resulting from a PSL sequence (Figure 2.10) may be modelled as

$$y_{m,t} = x_{m,t} + \upsilon_{m,t}, \tag{4.2}$$

where $\upsilon_{m,t}$ denotes an additive coloured Gaussian noise, often being modelled using a low order autoregressive (AR) model [Jakobsson et al., 2006; Kyriakidou et al., 2014]

$$x_{m,t} = \rho \sum_{k=1}^{K} s_k(\boldsymbol{\psi})\, e^{i\phi_k}\, e^{i\omega_k(T)t - \beta_k|t-\tau| - (t+2\tau m)\eta_k}, \tag{4.3}$$

with $m = 0, ..., M-1$ being the number of echoes and $t = t_0, ..., t_{N-1}$ is the echo sampling time, which is measured with respect to the center of the refocusing RF pulse and starting at $t_0 \neq 0$ to allow for the dead time between the excitation pulse and the first measured sample. Moreover, K is the number of NQR spectral lines and τ denotes the duration between the center of the preparatory pulse and the center of the first refocusing pulse. In a PSL sequence, the echo spacing is equal to 2τ (Figure 2.10). Furthermore, ρ, $s_k(\boldsymbol{\psi})$ and ϕ_k denote a common scaling constant due to the SNR, the (normalised) signal amplitude and the argument of the signal amplitude respectively. The damping constants characterizing the echo train are given by β_k and η_k. For simplicity, the spin-phase relaxation time of the k^{th} spectral line, T_2^*, is given by the sinusoidal damping constant $\beta_k = \frac{D_w}{T_2^*}$, with D_w being the dwell time. Similarly, the spin echo decay time, T_{2e}, can be expressed as $\eta_k = \frac{D_w}{T_{2e}}$, denoting the echo train damping constant. The quadrupolar frequency of the k^{th} NQR spectral line is denoted as $\omega_k(T)$ and it depends on the *unknown* temperature, T, of the sample under study. The frequency shifting functions of materials are assumed to be known and can be beneficially exploited in detection applications. For NQR signals, the frequency shifting functions may be well modelled as a linear function of temperature,

$$\omega_k(T) = a_k - b_k T, \tag{4.4}$$

where a_k and b_k are the known temperature coefficients of the material. The linear dependency of the TNT resonance frequencies on temperature is clearly illustrated in Somasundaram et al. [2007], Jakobsson et al. [2006] and Jakobsson et al. [2005c]. Another example includes the linear frequency shifting function of analgesic paracetamol tablets as presented in Kyriakidou et al. [2015]. As described in Jakobsson et al. [2006], the additive noise may be well described as an approximative low order autoregressive (AR) model. Thus, one may form the pre-whitened data model as

$$z_{m,t} = \sum_{k=1}^{K} \bar{C}\, \alpha_k\, e^{i\phi_k}\, e^{i\omega_k(T)t - \beta_k|t-\tau| - (t+2\tau m)\eta_k} + e_{m,t}, \tag{4.5}$$

where $e_{m,t}$ is an additive *white* Gaussian noise, α_k denotes the (complex) amplitude and

$$\bar{C} = \begin{cases} C(\lambda_k) & \text{for} \lfloor t - \tau \rfloor < 0 \\ C(\tilde{\lambda}) & \text{otherwise,} \end{cases} \tag{4.6}$$

with

$$\begin{aligned} \lambda_k &= e^{[i\omega_k(T)+\beta_k-\eta_k]} \\ \tilde{\lambda}_k &= e^{[i\omega_k(T)-\beta_k-\eta_k]}, \end{aligned} \tag{4.7}$$

and $C(\lambda_k)$ denoting the AR pre-whitening filter [Somasundaram et al., 2007; Jakobsson et al., 2006, 2005c].

Herein, the theoretical function of the complex amplitude, $s_k(\boldsymbol{\psi})$, is incorporated in the echo-train model in (4.3). The amplitude modulation function depends on both the experimental setup and the temperature of the examined material, i.e.,

$$\boldsymbol{\psi} = \begin{bmatrix} T & \tau & t_{\text{pw}} & \omega_{\text{exc}} & \omega_{\text{nf}} & \cos\theta \end{bmatrix}^T, \tag{4.8}$$

where $(\cdot)^T$ denotes the transpose. The parameters t_{pw}, ω_{exc} and ω_{nf} denote the pulse duration, excitation frequency and nutation frequency, respectively. Furthermore, θ is the angle between the RF field and the coil's axis [Gregorovič et al., 2009]. The theoretical expression of $s_k(\boldsymbol{\psi})$ is assumed to be a known function of the parameters in (4.8). From those parameters, some are known and some are assumed to be unknown; for instance, the temperature of the substance may not be accurately known [Somasundaram et al., 2007]. Gregorovič and Apih [2008], considered the theory of two spin interactions for a polycrystalline material with nuclei of spin $I = 1$; the quadrupole Hamiltonian, H_Q, and the RF Hamiltonian, H_{rf}, due to the external interaction of the RF field. The expression of the steady state amplitude modulation includes the influence of the off-resonance excitation both between and during the RF pulses. Using the assumption, $2\tau \leq T_{2e}$, the

theoretical function is given by

$$s_k(\boldsymbol{\psi}) = \zeta\, M \int_0^1 \cos\theta\, n_1\, n_2^2\, d(\cos\theta), \tag{4.9}$$

where ζ is a multiplicative constant, M is the number of signal acquisitions and

$$n_1 = \frac{2\omega_{1\theta}\sin\left(\tilde{\omega}_{1\theta}t_{\mathrm{pw}}\right)}{\tilde{\omega}_{1\theta}} \tag{4.10}$$

$$n_2 = \frac{\omega_{1\theta}\sin\left(\frac{1}{2}\tilde{\omega}_{1\theta}t_{\mathrm{pw}}\right)}{\tilde{\omega}_{1\theta}\sqrt{1-\cos^2\left(\frac{1}{2}\Omega t_c\right)}}. \tag{4.11}$$

The term in (4.10) indicates the influence of the off-resonance effects during the preparatory pulse, while (4.11) accounts for the rest of the RF pulses. The numerical integral in (4.9) represents an average over all crystalline orientations, assumed to be present with an equal probability in the crystal. Furthermore,

$$\begin{aligned}\cos\left(\frac{1}{2}\Omega t_c\right) &= \cos(\Delta\omega_k\tau)\cos\left(\frac{1}{2}\tilde{\omega}_{1\theta}t_{\mathrm{pw}}\right)\\ &\quad - \frac{\Delta\omega_k}{\tilde{\omega}_{1\theta}}\sin(\Delta\omega_k\tau)\sin\left(\frac{1}{2}\tilde{\omega}_{1\theta}t_{\mathrm{pw}}\right),\end{aligned} \tag{4.12}$$

where $\omega_{1\theta} = \omega_{\mathrm{nf}}\cos\theta$, $t_c = 2\tau + t_{\mathrm{pw}}$ and the effective strength of the RF field denoted as

$$\tilde{\omega}_{1\theta} = \sqrt{\Delta\omega_k^2 + \omega_{1\theta}^2}. \tag{4.13}$$

To achieve an optimum SNR enhancement, the number of echoes to sum up is expressed as [Marino and Klainer, 1977]

$$M = 1.25\frac{T_{2e}}{t_c} = 1.25\frac{T_{2e}}{2\tau + t_{\mathrm{pw}}}. \tag{4.14}$$

It is important to mention that approximations of the model in (4.9) may be derived. For strong RF excitation fields, there is no large deviation of the resulting magnetisation from the on-resonance magnetization, and one may neglect the off-resonance effects during the application of the RF pulse. However, for materials at low frequencies such as TNT, such an approximation is difficult to be assumed. As previously mentioned, for a polycrystalline sample in NQR, the signal is obtained by integration over all possible crystallite orientations in the PAS frame. Herein,

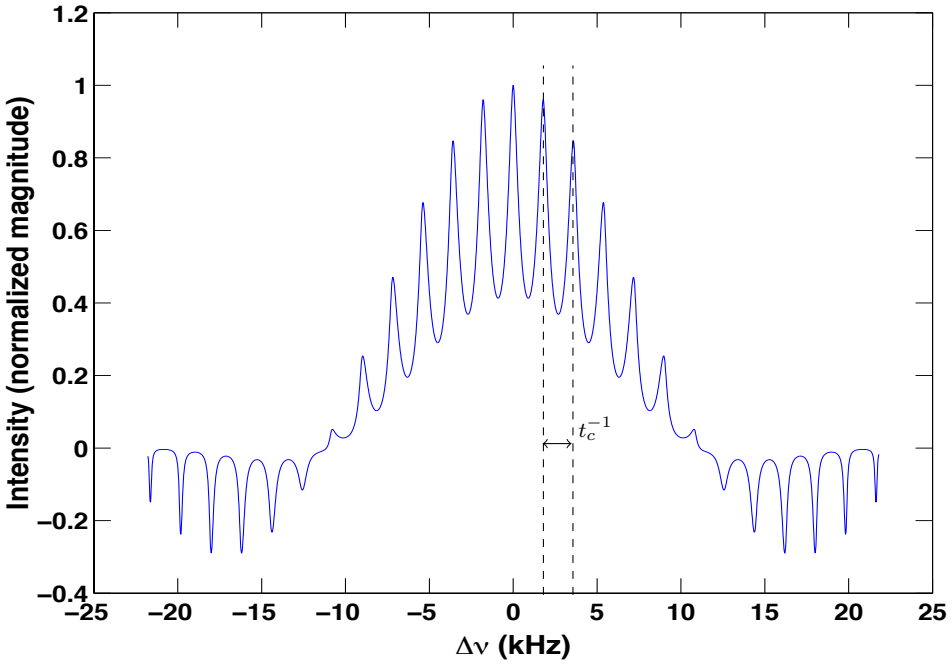

Figure 4.1: Theoretical amplitude (4.9) as a function of the off-resonance frequency, $\Delta\omega = 2\pi\Delta\nu$, for the 3.5 MHz NQR spectral line of sodium nitrite.

such an integral is expressed numerically.

In Figure 4.1, an example of the theoretical amplitude modulation with respect to the offset frequency is illustrated. Here, (4.9) was used to compute the signal amplitude for sodium nitrite, for the spectral line of 3.6 MHz. Clearly, there is a significant influence of the off-resonance excitation on the expected signal amplitude. In fact, the amplitude reaches the maximum on resonance, $\Delta\omega = 0$, while it exhibits a modulation with minimum and maximum values at $\Delta\omega_k = 2\pi\,(n + 1/2)/t_c$ and $\Delta\omega_k = 2\pi n/t_c$, respectively, with $n = 0, \pm1, \pm2, \ldots$ [Kyriakidou et al., 2014; Gregorovič et al., 2009]. The periodicity of the amplitude modulation illustrated in Figure 4.1 is t_c^{-1} [Gregorovič and Apih, 2008; Malone et al., 2011; Mikhaltsevitch and Rudakov, 2004; Malone and Sauer, 2012]. As shown, for the case of sodium nitrite, even an offset of 500 Hz can substantially reduce the detected SNR. The model in (4.3) will be controlled by the effect of the bandwidth of the coil's quality-factor. Herein, the assumption of a sufficiently large Q-factor is considered, to neglect these effects.

4.3 The ODETAML Detector

In this section, the offset dependent echo train approximate maximum likelihood detection algorithm ODETAML is formed, reminiscent to the presentation in Somasundaram et al. [2007]. Using (4.5), the m^{th} pre-whitened echo may be expressed as

$$\mathbf{z}_N^m \triangleq \left[\begin{array}{ccc} z^m(t_0) & \dots & z^m(t_{N-1}) \end{array} \right]^T = (\mathbf{A}_{\bar{\boldsymbol{\theta}}} \odot \mathbf{C})\mathbf{B}_m\boldsymbol{\alpha} + \mathbf{e}_N^m, \tag{4.15}$$

where N denotes the length of the NQR echo and

$$\mathbf{A}_{\bar{\theta}} = \left[\begin{array}{ccc} e^{(i\omega_1(T)-\eta_1)t_0-\beta_1|t_0-\tau|} & \dots & e^{(i\omega_K(T)-\eta_K)t_0-\beta_K|t_0-\tau|} \\ \vdots & \ddots & \vdots \\ e^{(i\omega_1(T)-\eta_1)t_{N-1}-\beta_1|t_{N-1}-\tau|} & \dots & e^{(i\omega_K(T)-\eta_K)t_{N-1}-\beta_K|t_{N-1}-\tau|} \end{array} \right], \tag{4.16}$$

$$\mathbf{B}_m = \text{diag}\left\{ \left[\begin{array}{ccc} e^{-\eta_1 m2\tau} & \dots & e^{-\eta_K m2\tau} \end{array} \right] \right\}, \tag{4.17}$$

$$\boldsymbol{\alpha} = \left[\begin{array}{ccc} \alpha_1 & \dots & \alpha_K \end{array} \right]^{\mathrm{T}}, \tag{4.18}$$

$$\mathbf{C} = \left[\begin{array}{ccc} C(\lambda_1) & \dots & C(\lambda_K) \\ \vdots & \ddots & \vdots \\ C(\lambda_1) & \dots & C(\lambda_K) \\ C(\tilde{\lambda}_1) & \dots & C(\tilde{\lambda}_K) \\ \vdots & \ddots & \vdots \\ C(\tilde{\lambda}_1) & \dots & C(\tilde{\lambda}_K) \end{array} \right]. \tag{4.19}$$

In (4.19), the size of the upper block and lower block of the matrix $\mathbf{C}$ is $(\lfloor \tau - t_0 \rfloor) \times K$ and $(N - \lfloor \tau - t_0 \rfloor) \times K$, respectively. The non-linear parameter vector, $\bar{\boldsymbol{\theta}}$, is defined as

$$\bar{\boldsymbol{\theta}} = \left[\begin{array}{ccc} T & \boldsymbol{\beta}^{\mathrm{T}} & \boldsymbol{\eta}^{\mathrm{T}} \end{array} \right]^{\mathrm{T}}, \tag{4.20}$$

where $\boldsymbol{\beta}$ and $\boldsymbol{\eta}$ are the vectors of unknown sinusoidal and echo damping constants, respectively. The prewhitened full echo train model can then be expressed by stacking each NQR echo, as

$$\mathbf{z}_{NM} \triangleq \left[\begin{array}{ccc} (\mathbf{z}_N^0)^T & \dots & (\mathbf{z}_N^{M-1})^T \end{array} \right]^T = \mathbf{H}_{\bar{\boldsymbol{\theta}}}\boldsymbol{\alpha} + \mathbf{e}_{NM}, \tag{4.21}$$

where e_{NM} is defined similar to $\mathbf{z}_{NM}$ and

$$\mathbf{H}_{\bar{\boldsymbol{\theta}}} = \begin{bmatrix} (\mathbf{A}_{\bar{\boldsymbol{\theta}}} \odot \mathbf{C})\mathbf{B}_0 \\ \vdots \\ (\mathbf{A}_{\bar{\boldsymbol{\theta}}} \odot \mathbf{C})\mathbf{B}_{M-1} \end{bmatrix}. \tag{4.22}$$

The complex amplitude, $\boldsymbol{\alpha}$, is factored as $\boldsymbol{\alpha} = \rho\boldsymbol{\kappa}$, where ρ is a common (complex) scaling due to the SNR and $\boldsymbol{\kappa}$ is a vector of *known* complex amplitudes. Thus, in the ODETAML detector, $\boldsymbol{\kappa}$ is given by the theoretical expression of the amplitude dependency on the off-resonance frequency in (4.9). As is well known, the maximum likelihood estimate of the unknown parameters, $\boldsymbol{\theta} = [\boldsymbol{\alpha}^T, \bar{\boldsymbol{\theta}}^T]^T$, is derived by (see, e.g., [Stoica and Moses, 2005])

$$\begin{aligned} \hat{\boldsymbol{\theta}} &= \arg\min_{\boldsymbol{\theta}} \left\| \mathbf{z}_{NM} - \mathbf{H}_{\bar{\boldsymbol{\theta}}}\boldsymbol{\alpha} \right\|_2^2 \\ &= \arg\min_{\boldsymbol{\theta}} \left\| \mathbf{z}_{NM} - \rho\mathbf{H}_{\bar{\boldsymbol{\theta}}}\boldsymbol{\kappa} \right\|_2^2. \end{aligned} \tag{4.23}$$

Therefore, the least squares estimate of ρ can be computed as

$$\hat{\rho} = (\mathbf{H}_{\bar{\boldsymbol{\theta}}}\boldsymbol{\kappa})^{\dagger}\mathbf{z}_{NM}, \tag{4.24}$$

where $\mathbf{X}^{\dagger} = (\mathbf{X}^*\mathbf{X})^{-1}\mathbf{X}^*$ denotes the Moore-Penrose pseudo-inverse of $\mathbf{X}$. Using the estimate of ρ in (4.24), the minimisation in (4.23) is given by

$$\begin{aligned} \hat{\boldsymbol{\theta}} &= \arg\min_{\boldsymbol{\theta}} \left\| \mathbf{z}_{NM} - \hat{\rho}\mathbf{H}_{\bar{\boldsymbol{\theta}}}\boldsymbol{\kappa} \right\|_2^2 \\ &= \arg\min_{\boldsymbol{\theta}} \left\| \mathbf{z}_{NM} - \mathbf{H}_{\bar{\boldsymbol{\theta}}}\boldsymbol{\kappa}(\mathbf{H}_{\bar{\boldsymbol{\theta}}}\boldsymbol{\kappa})^{\dagger}\mathbf{z}_{NM}) \right\|_2^2 \\ &= \arg\min_{\boldsymbol{\theta}} \left[\mathbf{z}_{NM}^*\mathbf{z}_{NM} - \mathbf{z}_{NM}^*\boldsymbol{\Pi}_{\mathbf{H}_{\bar{\boldsymbol{\theta}}}\boldsymbol{\kappa}}\mathbf{z}_{NM} \right], \end{aligned} \tag{4.25}$$

yielding the estimated non-linear parameter vector as

$$\hat{\bar{\boldsymbol{\theta}}} = \arg\max_{\bar{\boldsymbol{\theta}}} \ \mathbf{z}_{NM}^*\boldsymbol{\Pi}_{\mathbf{H}_{\bar{\boldsymbol{\theta}}}\boldsymbol{\kappa}}\mathbf{z}_{NM}, \tag{4.26}$$

where $\boldsymbol{\Pi}_{\mathbf{H}_{\bar{\boldsymbol{\theta}}}\boldsymbol{\kappa}} = (\mathbf{H}_{\bar{\boldsymbol{\theta}}}\boldsymbol{\kappa})(\mathbf{H}_{\bar{\boldsymbol{\theta}}}\boldsymbol{\kappa})^{\dagger}$. Herein, the algorithm is formed as a generalised likelihood ratio test (GLRT), where no prior knowledge of the variance of the

noise is required. Using (4.26), the test statistic $T(\mathbf{z}_{NM})$ is found as [Kay, 1998],

$$T(\mathbf{z}_{NM}) = (2NM-1)\frac{\mathbf{z}_{NM}^{*}\mathbf{\Pi}_{\mathbf{H}_{\hat{\boldsymbol{\theta}}}\boldsymbol{\kappa}}\mathbf{z}_{NM}}{\mathbf{z}_{NM}^{*}(\mathbf{I}-\mathbf{\Pi}_{\mathbf{H}_{\hat{\boldsymbol{\theta}}}\boldsymbol{\kappa}})\mathbf{z}_{NM}}, \tag{4.27}$$

with $\mathbf{I}$ denoting the identity matrix. The acceptable probability of false alarm is determined by a pre-set threshold value, γ; that is, the signal component is deemed present if and only if $T(\mathbf{z}_{NM}) > \gamma$, and otherwise not.

4.3.1 Frequency Selective ODETAML

The frequency selective counterparts of the AML and ODETAML, are formed in the frequency domain, which operate only on a subset of frequencies where the signal is expected to lie. In this section, the frequency selective version is summarised, forming the FODETAML, reminiscent to the derivations in Jakobsson et al. [2006] and Somasundaram et al. [2007]. Normally, the signal of interest is found within a known narrow band of frequencies. In most applications, the sample temperature may be assumed to vary within a known temperature range. Since the resonance frequencies are temperature dependent, according to (4.4), one may determine where the signal would lie in the frequency spectrum. Consider the frequency grid points

$$\left\{\frac{2\pi k_1}{N}, \frac{2\pi k_2}{N}, \ldots, \frac{2\pi k_L}{N}\right\}, \tag{4.28}$$

with $k_1, \cdots, k_L$ being L given, not necessarily consecutive, integers selected such that (4.28) only consists of the possible frequency grid points for each of the K frequency lines. Such a region is determined by the minimal and maximal frequency values for that line, considering the *measured* sample temperature, $\hat{T}_s$, and the size of the expected temperature uncertainty region, Δ_{T_s}, during a measurement. Using (4.4), this narrow band of frequencies, $\Delta\omega_s$, is determined by $T = \hat{T}_s \pm \Delta_{T_s}$. The Fourier transformed prewhitened data vector of the m^{th} echo is expressed as

$$Z_k^m = \mathbf{v}_k^{*}(\mathbf{A}_{\bar{\boldsymbol{\theta}}} \odot \mathbf{C})\mathbf{B}_m\boldsymbol{\alpha} + E_k^m, \tag{4.29}$$

where $E_k^m = \mathbf{v}_k^* \mathbf{e}_N^m$ represents the k^{th} frequency bin of the prewhitened noise sequence associated with the m^{th} echo, $\mathbf{e}_N^m$, and

$$\mathbf{v}_k = \left[\begin{array}{cccc} 1 & e^{i2\pi k/N} & \dots & e^{i2\pi k(N-1)/N} \end{array} \right]^T. \tag{4.30}$$

Therefore, for the frequency band of interest, given by

$$\mathbf{V}_L = \left[\begin{array}{ccc} \mathbf{v}_{k_1} & \dots & \mathbf{v}_{k_L} \end{array} \right], \tag{4.31}$$

(4.29) can be expressed as

$$\mathbf{Z}_L^m \triangleq \left[\begin{array}{ccc} Z_{k_1}^m & \dots & Z_{k_L}^m \end{array} \right]^T = \mathbf{V}_L^*(\mathbf{A}_{\bar{\boldsymbol{\theta}}} \odot \mathbf{C})\mathbf{B}_m \boldsymbol{\alpha} + \mathbf{E}_L^m, \tag{4.32}$$

where $\mathbf{E}_L^m$ is defined similar to $\mathbf{Z}_L^m$. The entire echo train is then given by

$$\mathbf{Z}_{LM} \triangleq \left[\begin{array}{ccc} (\mathbf{Z_L^0})^T & \cdots & (\mathbf{Z_L^{M-1}})^T \end{array} \right]^T = \tilde{\mathrm{H}}_{\bar{\boldsymbol{\theta}}} \boldsymbol{\alpha} + \mathbf{E}_{LM}, \tag{4.33}$$

with $\mathbf{E}_{LM}$ being defined similar to $\mathbf{Z}_{LM}$, and

$$\tilde{\mathbf{H}} = \left[\begin{array}{c} \mathbf{V}_L^*(\mathbf{A}_{\bar{\boldsymbol{\theta}}} \odot \mathbf{C})\mathbf{B}_0 \\ \vdots \\ \mathbf{V}_L^*(\mathbf{A}_{\bar{\boldsymbol{\theta}}} \odot \mathbf{C})\mathbf{B}_{M-1} \end{array} \right]. \tag{4.34}$$

Thus, using (4.33), the minimization in (4.23) can be approximated as

$$\hat{\theta} = \arg \min_{\boldsymbol{\theta}} \left\| \mathbf{Z}_{LM} - \tilde{\mathbf{H}}\boldsymbol{\alpha} \right\|_2^2. \tag{4.35}$$

Similar with the ETAML detector, the GLRT is determined as (4.27). From a computational point of view, one should exploit that the indices of $\Psi_{\bar{\boldsymbol{\theta}}}^m \triangleq \mathbf{V}_L^*(\mathbf{A}_{\bar{\boldsymbol{\theta}}} \odot \mathbf{C})\mathbf{B}_m$ form geometric series; the $(l,k)^{th}$ index of $\Psi_{\bar{\boldsymbol{\theta}}}^m$ can be written as

$$\left[\Psi_{\bar{\boldsymbol{\theta}}}^m\right]_{l,k} = G_k \left[\Omega_1 + \Omega_2\right], \tag{4.36}$$

where

$$G_k = e^{-\eta_k(t_0+2\tau m)+i\omega_k(T)t_0}, \tag{4.37}$$

$$\Omega_1 = C(\lambda_k)e^{\beta_k(t_0-\tau)}\frac{\left(1-\upsilon_{l,k}^{\lfloor\tau-t_0\rfloor+1}\right)}{1-\upsilon_{l,k}}, \tag{4.38}$$

$$\Omega_2 = C(\tilde{\lambda}_k)e^{-\beta_k(t_0-\tau)}\frac{\left(u_{l,k}^{\lfloor\tau-t_0\rfloor+1}-u_{l,k}^{N}\right)}{1-u_{l,k}}, \tag{4.39}$$

with

$$\upsilon_{l,k} = e^{-i2\pi k_l/N+i\omega_k(T)-\eta_k+\beta_k} \tag{4.40}$$

$$u_{l,k} = e^{-i2\pi k_l/N+i\omega_k(T)-\eta_k-\beta_k}. \tag{4.41}$$

4.4 Cramér Rao Lower Bound

For the extended model in (4.3) and (4.9), the Cramér-Rao lower bound (CRLB) is derived [Gudmundson et al., 2012]. The notation for the m^{th} signal echo, is simplified as

$$x_{m,t} = \sum_{k=1}^{K} \rho\, s_k(\psi)\, e^{i\phi_k}\, \lambda_k^{m,t}, \tag{4.42}$$

where

$$\lambda_k^{m,t} \triangleq e^{iw_k t-\beta_k|t-\tau|-(t+2\tau m)\eta_k}. \tag{4.43}$$

A NQR echo train which consists of M echoes, each of length N, can be written as

$$\mathbf{y}_{NM} = \mathbf{x}_{NM} + \boldsymbol{\upsilon}_{NM}, \tag{4.44}$$

by gathering all the NM measurements on a vector form and

$$\mathbf{x}_{NM} = \begin{bmatrix} \mathbf{x}_0^T & \dots & \mathbf{x}_{M-1}^T \end{bmatrix}^T, \tag{4.45}$$

$$\mathbf{x}_m = \begin{bmatrix} x_{m,t_0} & \dots & x_{m,t_{N-1}} \end{bmatrix}^T, \tag{4.46}$$

$$\boldsymbol{\upsilon}_{NM} = \begin{bmatrix} \upsilon_{0,t_0} & \dots & \upsilon_{M-1,t_{N-1}} \end{bmatrix}^T. \tag{4.47}$$

The CRLB is defined as the inverse of the Fisher Information Matrix (FIM) (see Appendix A) and is given by

$$\mathbf{C}_{\text{CRB}}(\boldsymbol{\gamma}) = [\mathbf{F}(\boldsymbol{\gamma})]^{-1}, \tag{4.48}$$

with $\boldsymbol{\gamma}$ denoting the vector of unknown parameters, i.e.,

$$\boldsymbol{\gamma} = \begin{bmatrix} \rho & \boldsymbol{\omega}^T & \boldsymbol{\phi}^T & \boldsymbol{\beta}^T & \boldsymbol{\eta}^T \end{bmatrix}^T \tag{4.49}$$

$$\boldsymbol{\omega} = \begin{bmatrix} \omega_1 & \dots & \omega_K \end{bmatrix}^T, \tag{4.50}$$

$$\boldsymbol{\phi} = \begin{bmatrix} \phi_1 & \dots & \phi_K \end{bmatrix}^T, \tag{4.51}$$

$$\boldsymbol{\beta} = \begin{bmatrix} \beta_1 & \dots & \beta_K \end{bmatrix}^T, \tag{4.52}$$

$$\boldsymbol{\eta} = \begin{bmatrix} \eta_1 & \dots & \eta_K \end{bmatrix}^T. \tag{4.53}$$

Herein, the temperature is a function of the fundamental parameter, ω_k, such as $T = \frac{\alpha}{\beta} - \frac{1}{\beta}\omega$. Therefore, the temperature is estimated using the Jacobian matrix, $\partial \mathbf{g}(\boldsymbol{\theta})/\partial \boldsymbol{\theta}$, as described in Appendix A. Using the Slepian-Bangs formula [Stoica and Moses, 2005; Gudmundson et al., 2012; Kay, 1993], the FIM can be expressed as

$$\mathbf{F}(\boldsymbol{\gamma}) = \frac{2}{\sigma^2}\left[\text{Re}\left\{\left(\frac{\partial \mathbf{x}}{\partial \boldsymbol{\gamma}}\right)^H \left(\frac{\partial \mathbf{x}}{\partial \boldsymbol{\gamma}}\right)\right\}\right], \tag{4.54}$$

where σ^2 is the variance of $\boldsymbol{\upsilon}_{NM}$. The derivatives with respect to the elements in

$\boldsymbol{\gamma}$ are denoted as

$$\frac{\partial x_{m,t}}{\partial \rho} = \sum_{k=1}^{K} s_k(T)\, e^{i\phi_k} \lambda_k^{m,t}, \tag{4.55}$$

$$\frac{\partial x_{m,t}}{\partial \omega_k} = i\, t\, \rho\, s_k(T)\, e^{i\phi_k} \lambda_k^{m,t}(T), \tag{4.56}$$

$$\frac{\partial x_{m,t}}{\partial \phi_k} = i\, \rho\, s_k(T)\, e^{i\phi_k} \lambda_k^{m,t}, \tag{4.57}$$

$$\frac{\partial x_{m,t}}{\partial \beta_k} = -\rho\, |t-\tau| s_k(T)\, e^{i\phi_k} \lambda_k^{m,t}, \tag{4.58}$$

$$\frac{\partial x_{m,t}}{\partial \eta_k} = -\rho\, (t + 2\,\tau\, m)\, s_k(T)\, e^{i\phi_k} \lambda_k^{m,t}. \tag{4.59}$$

4.5 Experimental Procedure

The NQR off-resonance amplitude modulation model in (4.9), is validated using measurements on three different materials. These include powder sodium nitrite, generic caplets of metformin and loose powder of aniracetam. The measurements were conducted using the experimental equipment described in Chapter 3. An automated function of the NTNMR system allowed the excitation of frequencies, in specified increments, from a set reference frequency; normally, this is the resonance frequency. Thus, the off-resonance dependence of the signals was obtained. Under carefully stabilised temperature conditions, the temperature was kept monitored at 283 ± 0.5 K by immersing the coil in silicon oil bath within the probe. The IF temperature sensor was used to record the actual temperature within the probe and the temperature was in fact varying within ± 0.25 K for all measurements. Throughout the duration of the measurements, the resonance frequency was checked frequently, with the average sample temperature being estimated using the known frequency shifting functions. Thus, any small offset of the resonance frequency was monitored. Herein, the signals from individual/single peaks were exploited. Therefore, the off-resonance profiles of the NQR signals were obtained by summing the PSL echoes in each scan and the signal intensities were derived by Fourier transformation. The pulse sequence parameters are summarised in the following sections. Furthermore, the CRLB of the refined model in (4.9), is compared to the variability in the echo trains for each of the three samples. For these measurements, PSL signal echo trains were recorded.

4.5.1 Sodium Nitrite

A wealth of research has been done in NQR using sodium nitrite [Mozzhukhin et al., 2008; Ikeda et al., 1969; Petersen and Bray, 1976; Sauer et al., 2001; Garroway et al., 1994a]. The molecule of sodium nitrite shown in Figure 4.2, contains one quadrupolar nuclei, ^{14}N ($I = 1$), with a single nitrogen site cor-

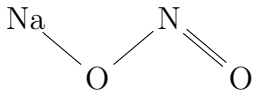

Figure 4.2: The molecular structure of sodium nitrite.

responding to three NQR resonance lines; $\nu_+ = 4.640$ MHz, $\nu_- = 3.601$ MHz and $\nu_0 = 1.023$ MHz, at room temperature. Over the temperature range of $240 - 313$ K, the resonance frequencies for the three lines were measured. The frequency shifting functions are shown in Figure 4.3. Table 4.1 contains the temperature coefficients determined from the associated frequency shifting functions.

Table 4.1: The temperature shifting function constants for the NQR transition lines of sodium nitrite.

	ν_+	ν_-	ν_0
a (MHz/K)	5.228	3.924	1.091
b (kHz/K)	2.00	1.091	0.813

Herein, experiments were conducted using 80 g of powder sodium nitrite, at the $\nu_- = 3.615$ MHz resonance transition and monitored at 283 K. For this frequency, $T_1 = 315$ ms, $T_2 = 3.1$ ms and $T_2^* = 0.67$ ms [Petersen and Bray, 1976]. The sample was immersed in a silicone oil to reduce any unwanted piezoelectric signals. For these measurements, a quarter-wave unit was used, which was centred at 3.3 MHz. The data were acquired using a PSL sequence. The experimental parameters are summarised in Table 4.2.

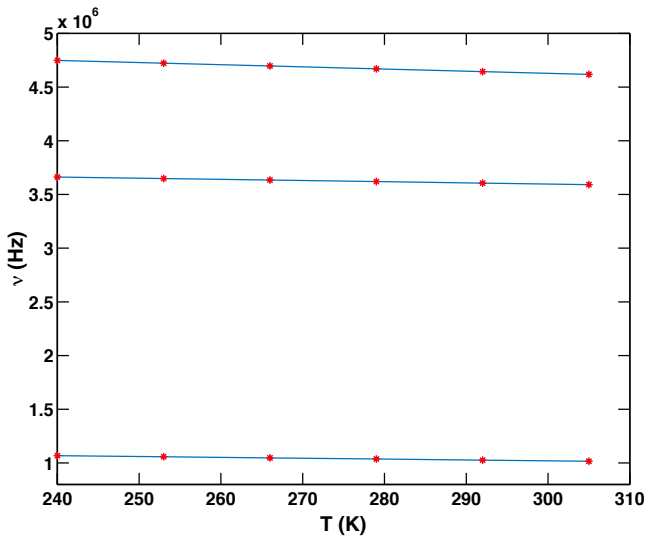

Figure 4.3: Resonance frequency versus temperature for the ν_+, ν_- and ν_0 NQR spectral lines of powder sodium nitrite; linear fit using $\omega = a - bT$ ($\omega = 2\pi\nu$).

4.5.2 Metformin Hydrochloride

Metformin hydrochloride is an oral antidiabetic drug, primarily used for the treatment of Type-2 diabetes, and it is mainly beneficial in overweight and obese patients [NHS, 2015; Kirpichnikov et al., 2002; Davidson and Peters, 1997]. For diabetes mellitus, metformin hydrochloride helps to maintain and control the level of blood sugar, by improving the patients' glucose tolerance. In the molecule, there

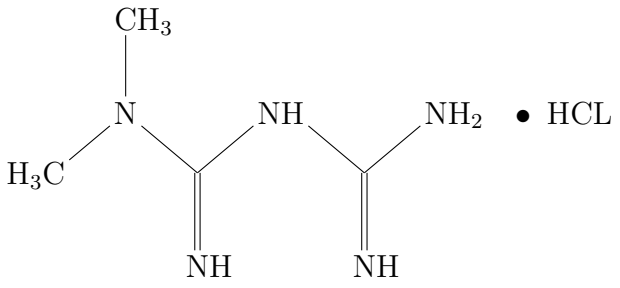

Figure 4.4: The molecular structure of metformin hydrochloride.

are multiple ^{14}N sites; in fact, five sets of three ^{14}N NQR resonance frequencies for each chemically different nitrogen environment can be observed. The NQR parameters provided by Dr. Iain Poplett and Dr. Jamie Barras, are summarised in Tables 4.3 and 4.4. Metformin hydrochloride is on the WHO list of essential

Table 4.2: PSL experimental parameters – Sodium nitrite.

excitation frequency (kHz)	3615.2
pulse width (µs)	40
τ spacing (µs)	407
echo spacing (µs)	814
dwell time (µs)	1
dead time (µs)	344
acquisition delay (µs)	458
repeat time (s)	1.5
acquisition time (µs)	64
number of echoes	128
samples per echo	64
scans	8

Table 4.3: ^{14}N NQR frequencies, asymmetry parameters and quadrupole coupling constants of metformin hydrochloride (T = 295 K).

k	ν_+ (kHz)	ν_- (kHz)	ν_0 (kHz)	η	e^2qQ/h (kHz)
1	3067	2908	159	0.08	3983
2	2834	2174	660	0.40	3339
3	2821	2117	704	0.43	3292
4	2721	2450	271	0.16	3447
5	2610	1874	736	0.49	2989

Table 4.4: Spin lattice relaxation constant for the ν_+ transition lines (T = 295 K).

ν_+ (kHz)	T_1 (s)	T_2^* (ms)	T_{2e} (ms) (for τ = 3.312 ms)
3067	6		
2834	16	1.53	880
2821	9	1.32	960
2721	14		2705
2610	10		

medicines [WHO, 2015]. The schematic structure of the metformin hydrochloride molecule is illustrated in Figure 4.4. Moreover, Figure 4.5 and Table 4.5 show the frequency shifting functions over the range $288.5 - 312$ K, and their associated constants of the ν_+ transition lines, respectively.

Herein, two ν_+ resonance frequencies were studied; these are the 2835 and 2822 kHz, at 283 K. The caplets of metformin hydrochloride were analysed in their standard size medicine bottle (30 caplets $\times$ 0.5 g). The PSL experimental

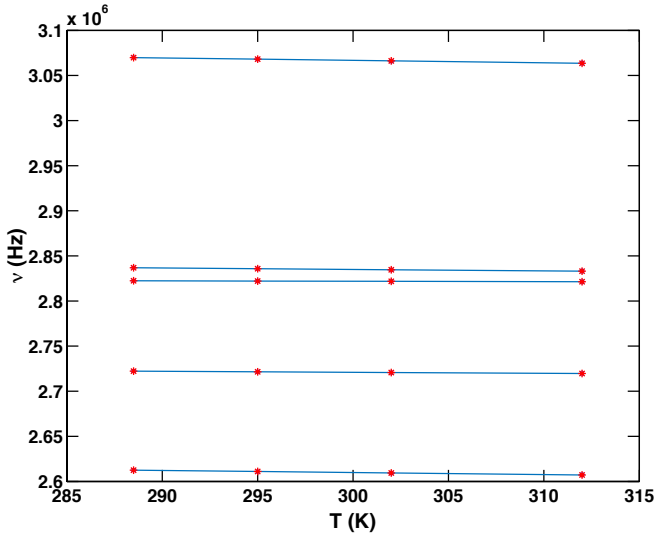

Figure 4.5: Resonance frequency versus temperature for the $\nu+$ NQR spectral lines of metformin hydrochloride; linear fit using $\omega = a - bT$ ($\omega = 2\pi\nu$).

Table 4.5: The temperature shifting function constants for the ν_+ NQR transition lines.

k	ν_+ (kHz)	a (MHz)	b (kHz/K)
1	3067	3.147	0.268
2	2834	2.881	0.163
3	2821	2.834	0.044
4	2721	2.755	0.114
5	2610	2.677	0.223

Table 4.6: PSL experimental parameters – Metformin hydrochloride.

excitation frequency (MHz)	2.835, 2.822
pulse width (µs)	60
τ spacing (µs)	520
echo spacing (µs)	1040
dwell time (µs)	4
dead time (µs)	304
acquisition delay (µs)	306
repeat time (s)	80, 50
acquisition time (µs)	512
number of echoes	512
samples per echo	128
scans	16

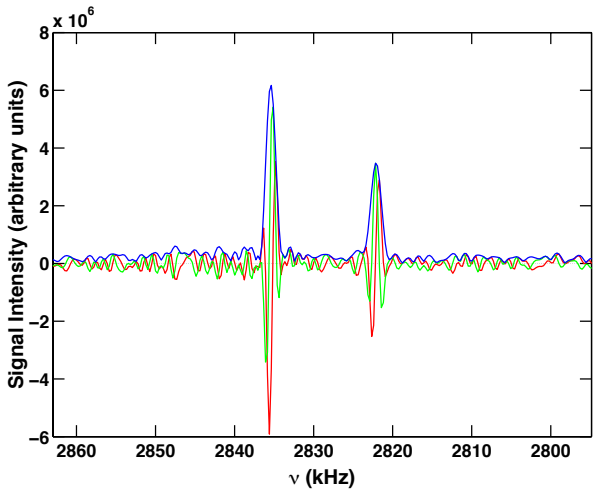

Figure 4.6: Fourier transformed NQR signal from metformin hydrochloride caplets.

parameters are summarised in Table 4.6. Furthermore, Figure 4.6 shows the Fourier transformed signal of the examined frequency lines.

4.5.3 Aniracetam

Aniracetam belongs to the nootropic type of drugs, which are used for the improvement of cognition and mental performance [Lee and Benfield, 1994; Croker et al., 2012]. This supplement is a compound of the racetam chemical class that shares the common pyrrolidone nucleus. Some of the beneficial functions of aniracetam include the enhancement of memory, mental endurance, focus and concentration [Lee and Benfield, 1994]. Figure 4.7 illustrates the molecular structure of aniracetam. In the molecule, there is only one ^{14}N site. Thus, one triplet

Table 4.7: ^{14}N NQR frequencies, asymmetry parameter and quadrupole coupling constant of aniracetam (T = 283 K).

ν_+ (kHz)	ν_- (kHz)	ν_0 (kHz)	η	e^2qQ/h (kHz)
2553	2410	143	0.09	3309

of the NQR resonance frequencies is observed. Table 4.7 shows the ^{14}N parameters, as obtained by Dr. Iain Poplett. Herein, the 2553 kHz resonance line is examined using 84 g of powder aniracetam. The relaxation time constants of this line are $T_1 = 300$ ms, $T_2 = 1.14$ ms and $T_{2e} = 380$ ms (for $\tau = 3.3$ ms), at 283 K.

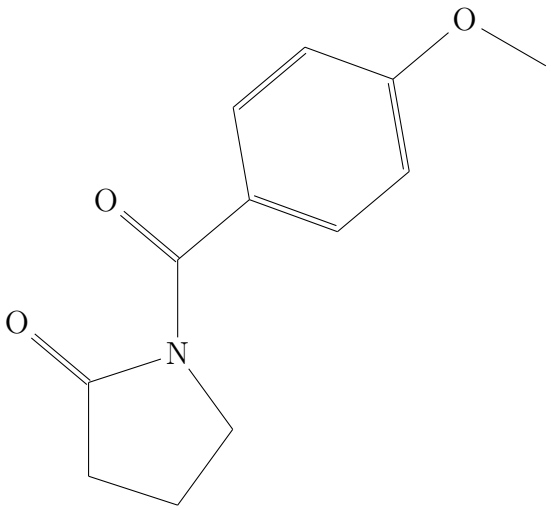

Figure 4.7: The molecular structure of aniracetam.

Moreover, the frequency shifting functions are illustrated in Figure 4.8, for the range $270 - 310$ K. Using (4.4), the temperature shifting constants are computed as $a = 2.564$ MHz and $b = 0.040$ kHz/K. The PSL timings are summarised in Table 4.8. Figure 4.9 shows the Fourier transformed signal obtained from the examined resonance line of powder aniracetam.

4.6 Numerical Results

The dependence of the ^{14}N NQR signal amplitude on the off-resonance excitation frequency was examined for the three materials. The experimental measurements and theoretical behaviour derived from the model in (4.9) are compared. The results are illustrated in Figures 4.10, 4.11 and 4.12 for sodium nitrite, metformin hydrochloride and aniracetam, respectively. For each compound, the signal was acquired under an off-resonance excitation frequency range; for sodium nitrate, $\Delta\nu = \pm 2$ kHz in steps of 20 Hz, for metformin hydrochloride, $\Delta\nu = -2.2$ to $+1.8$ kHz in steps of 40 Hz, and for aniracetam, $\Delta\nu = -1.25$ to $+0.75$ kHz, in steps of 50 Hz. The results reveal a reasonably good agreement between the theoretical model and the experimental measurements, yielding a reliable prediction of the expected signal amplitude with respect to the off-resonance frequency.
For all the materials, there is an evident modulation in the form of a periodic waveform, with periodicity $1/t_c$, where $t_c = t_{\mathrm{pw}+2\tau}$. As discussed in Gregorovič

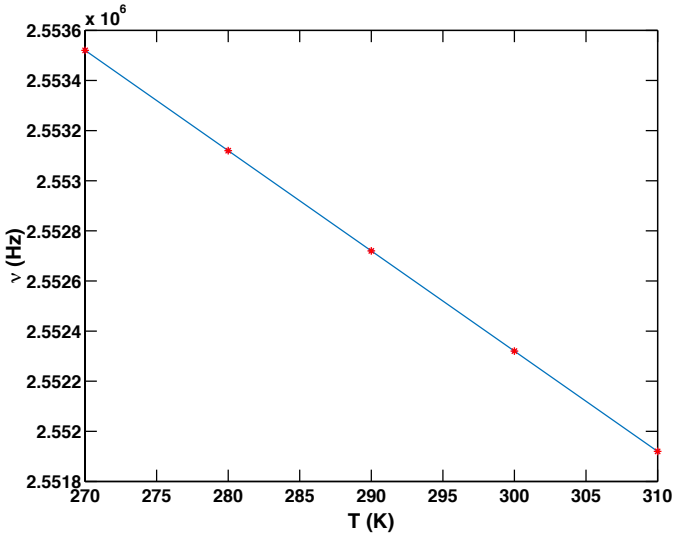

Figure 4.8: Resonance frequency versus temperature for the $\nu+$ NQR spectral line of aniracetam; linear fit using $\omega = a - bT$ ($\omega = 2\pi\nu$) where $a = 2.564$ MHz and $b = 0.040$ kHz/K.

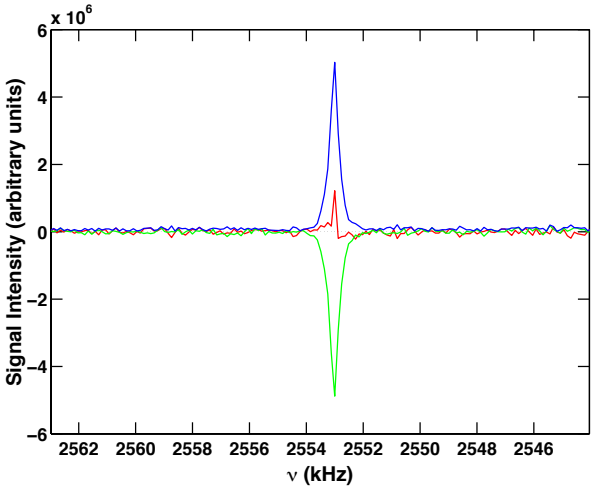

Figure 4.9: Fourier transformed signal of powdered aniracetam.

et al. [2009], Malone [2013] and Prescott [2010], the signal intensity reaches its maximum value when the on-resonance condition is met ($\Delta\nu = 0$), whereas when $\Delta\nu \neq 0$, the signal follows a sinc-like function with minimum values observed every $\Delta\nu = (n + 1/2)/t_c$ and maximum every $\Delta\nu = n/t_c$. As illustrated in Figure 4.10, there is a significant reduction in the expected signal intensity for sodium nitrite, when the resonance frequency is missed just by 500 Hz; this corresponds

Table 4.8: PSL experimental parameters – Aniracetam.

excitation frequency (kHz)	2553.1
pulse width (µs)	60
τ spacing (µs)	592
echo spacing (µs)	1184
dwell time (µs)	2
dead time (µs)	304
acquisition delay (µs)	306
repeat time (s)	1.5
acquisition time (µs)	512
number of echoes	128
samples per echo	256
scans	20

to only a small uncertainty in the sample's temperature of about 0.5 K. Furthermore, Figures 4.11 and 4.12 show the off-resonance profiles for both metformin hydrochloride and aniracetam, respectively. According to Malone et al. [2011] and Prescott [2010], this periodic waveform is generally more pronounced in samples with narrower spectral lines. One may determine the spectral linewidth (full-width at half-maximum (FWHM) $\nu_{1/2}$) by exploiting the spin-phase relaxation time constant, T_2^*, from the relation $\nu_{1/2} = 1/\pi T_2^*$ for Lorentzian lines [Petersen and Bray, 1976; Mikhaltsevitch and Rudakov, 2004]. Using the aforementioned relation, sodium nitrite, the two lines of metformin hydrochloride ($\nu_{+1} = 2834$ kHz and $\nu_{+2} = 2821$ kHz) and aniracetam, have linewidths of approximately 454, 208 and 241, and 280 Hz, respectively. In Figure 4.11(b), for the same RF pulse spacing, there is a decrease in the dips of the oscillations. This is because of the broader linewidth of this line, with a greater EFG in the vicinity of the nucleus. The amplitude of the oscillations is generally influenced by the condition $1/2t_c$ [Malone et al., 2011; Prescott, 2010; Sauer and Klug, 2006]. The longer the RF refocusing pulse spacing, the closer the linewidth approaches to this condition, and the shallower the dips of the off-resonance periodic behaviour must be [1]. Therefore, the amplitude is strongly correlated and dependent on the relation $e^{-2\tau/T_2^*}$; as the echo spacing increases, the dips of the offset profile are reduced since the spectral linewidth tends to approach $1/2t_c$ [Malone, 2013; Miller, 2007; Rudakov et al., 1997; Sauer and Klug, 2006]. To include for this effect, the amplitude model

[1] In similar words, the off-resonance amplitude oscillations tend to decrease as $2t_c$ approaches πT_2^*.

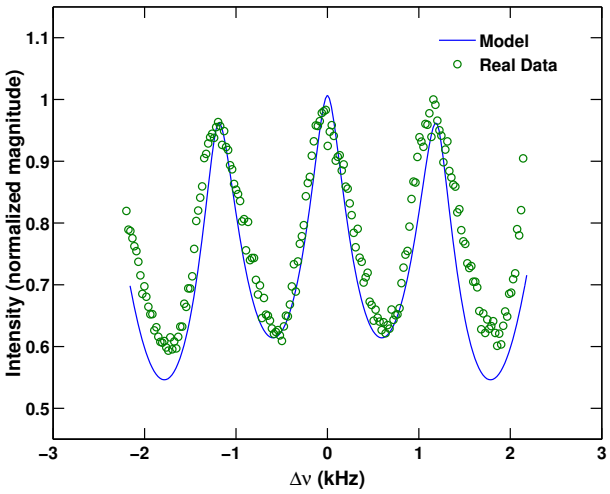

Figure 4.10: Comparison of the theoretical and experimental NQR signal intensities of sodium nitrite ($\nu_- = 3615$ kHz), as a function of the off-resonance excitation frequency; periodicity $1/t_c = 1.171$ kHz.

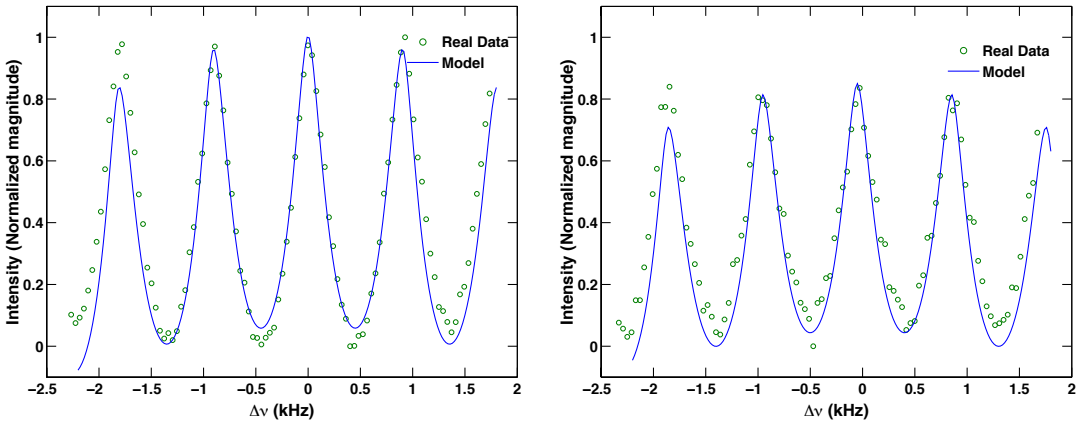

Figure 4.11: Comparison of the theoretical and experimental NQR signal intensities of metformin hydrochloride, as a function of the off-resonance excitation frequency; periodicity $1/t_c = 0.906$ kHz; (a) $\nu_{+1} = 2834$ kHz and (b) $\nu_{+2} = 2821$ kHz.

in (4.9) is simply convolved with a Lorentzian function, using the corresponding linewidths. It must be mentioned that the theoretical model is not a fit on the real measurements; instead, the theoretical values are calculated using the PSL experimental parameters, and scaled accordingly. Furthermore, measurements have been conducted on sodium nitrite over a range of 2τ spacings. The results

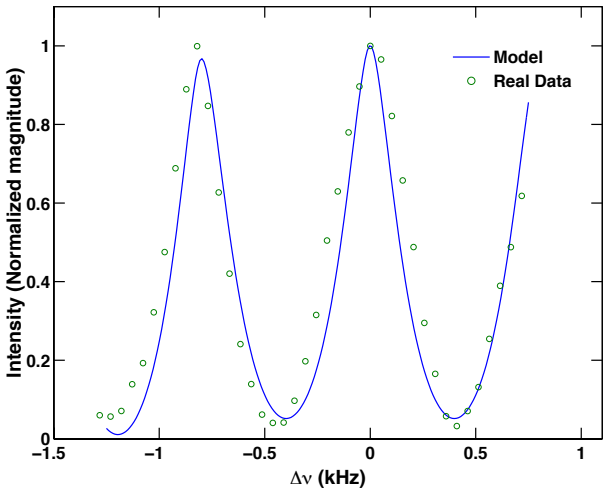

Figure 4.12: Comparison of the theoretical and experimental NQR signal intensities of aniracetam ($\nu_+ = 2553.1$ kHz), as a function of the off-resonance excitation frequency; periodicity $1/t_c = 0.804$ kHz.

are illustrated in Figure 4.13. As expected, the depth of the oscillations is reduced with longer echo spacings, as the linewidth of the sodium nitrite begins to reach $1/2t_c$. Again, there is a good agreement between the theoretical model and the experimental measurements. The slight discrepancies may possibly occur because of the omission of the spin echo decay time constant dependency on the off-resonance excitation frequency, which might influence the theoretical amplitude model. As described in Gregorovič et al. [2009], any uncertainties in the resonance frequency would also affect T_{2e}, which is shown to follow an oscillatory behaviour with respect to the offset frequency, with periodicity $1/t_c$. However, the degree of the dependency of T_{2e} on the off-resonance effects has been shown to be lower than the dependency of the signal amplitude [Gregorovič et al., 2009].

The proposed algorithm was evaluated using simulated NQR data. The formed signal imitated the response from the $\nu_- = 3.615$ MHz frequency line of sodium nitrite, when excited using a PSL sequence. As discussed in Section 4.1, the ODFETAML algorithm exploits the full NQR echo train signal [Somasundaram et al., 2007]. Trains of echoes were generated given the PSL parameters in Table 4.2, where $M = 128$ and $N = 64$ [2]. The non-linear parameter vector was estimated using a grid search method. As described in Somasundaram

[2]Herein, M and N denote the number of echoes and the number of samples per echo, respectively.

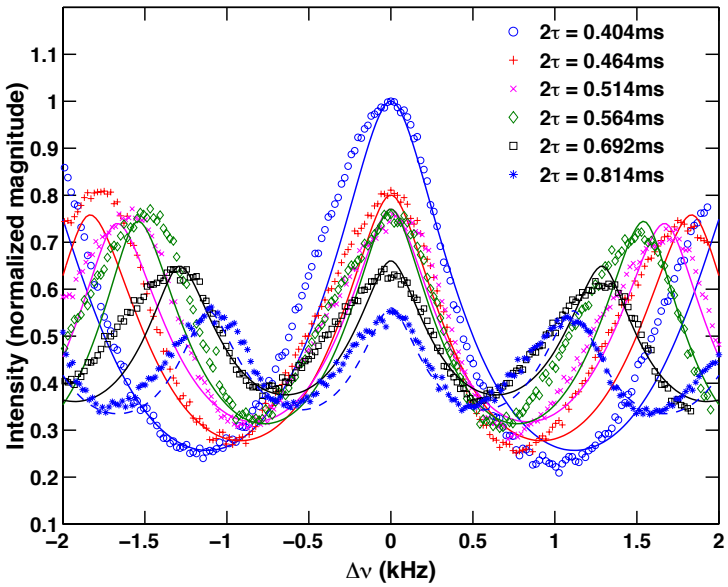

Figure 4.13: Comparison of experimental and theoretical NQR signal intensities, for sodium nitrite, as a function of the off-resonance excitation frequency, $\Delta\nu$, for a range of echo spacings (2τ).

et al. [2007], it is often beneficial to reduce computational complexity by following strategies, that reduce the multidimensional search. For multiple frequencies, Somasundaram [2007] refers to the grouping of the unknown parameters, particularly in multiple line substances, where the values of the sinusoidal and echo train damping constants are similar. Furthermore, one may reduce the dimension of the parameter space by splitting it into multiple lower dimensional spaces. This strategy requires initial estimates to be obtained, normally set as the middle value of the selected grid search range for the associated parameter. Another procedure for dimensionality reduction, is to exploit relationships among the parameters. For instance, as in the ETAML-based algorithms, the frequency dependency on the sample's temperature is also incorporated in the ODFETAML detector. In this way, a single search over the sample's temperature is exploited, instead of searching for k frequency lines. Herein, the simulations were obtained using $2K+1$ dimensional search (K: number of resonance lines), i.e., for the here single line measurements of the compounds of interest, this was implemented using 3 one-dimensional searches over the unknown non-linear parameters (i.e., over temperature, the sinusoidal dampings β_k, and the echo train dampings η_k, for the k^{th} frequency line). The grid search over temperature was selected as

$[280, 284]$ K in 500 steps, whereas for the damping constants, the search regions were $\beta = [1 \times 10^{-5}, 0.01]$ and $\eta = [0.0001, 0.1] \times 10^{-4}$ in 500 and 800 steps, respectively. For such a signal, the true damping parameters were $\beta_{\mathrm{T}} = 0.0017$ and $\eta_{\mathrm{T}} = 6.06 \times 10^{-6}$. The proposed algorithm was evaluated over $P = 1500$ Monte Carlo simulations, and the SNR was -15 to 20 dB in steps of 5 dB. Herein, the SNR is defined as

$$\mathrm{SNR} = \frac{\sigma_{\mathrm{s}}^2}{\sigma_{\mathrm{w}}^2}, \tag{4.60}$$

where σ_{s}^2 and σ_{w}^2 denote the noise-free signal and the power of the noise, respectively. The normalised root mean squared error (NRMSE) is given by

$$\mathrm{NRMSE} = \sqrt{\frac{1}{P}\sum_{p=1}^{P} \mid \hat{x}_p - x \mid^2}, \tag{4.61}$$

where $\hat{x}_p$ is the parameter estimate in the p^{th} Monte Carlo simulation and x is the true parameter value. Herein, the NRMSE of the estimated parameters was compared to the corresponding CRLB. Figure 4.14 illustrates the results for the on-resonance excitation, $\Delta\nu = 0$ Hz ($|\kappa| = 1$). As a comparison, the CRLB is also displayed. As shown, the CRLB is attained for the SNR range considered, indicating the statistical efficiency of the proposed algorithm. Note that at lower SNRs, the accuracy in the parameters' estimation may be influenced by grid limitations, while at higher SNRs, the NRMSE values may appear to flatten out at the resolution limit. Figure 4.14 was reproduced for two off-resonance excitation frequencies, $\Delta\nu = 1.7$ kHz ($|\kappa| = 0.5$) and $\Delta\nu = 2.2$ kHz ($|\kappa| = 0.7$), as illustrated in Figures 4.15 and 4.16, respectively (see also Figure 4.10). The algorithm achieves the theoretical bound, which is shown to vary with the off-resonance frequency; i.e., with the sample temperature.

Proceeding, the CRLB is exploited in order to determine a proper measurement setup. As described previously, substandard or counterfeit medicines may often not contain the correct dosage of active ingredient, posing the need of generating accurate "fingerprints". Many studies report on the quantitative characterisation of the active ingredient using pure NQR [Tate et al., 2009; Perez et al., 2005; Barras et al., 2013]. Thus, a "fingerprint" should reflect the expected quantity of the medicine under study, in order to investigate its authenticity.

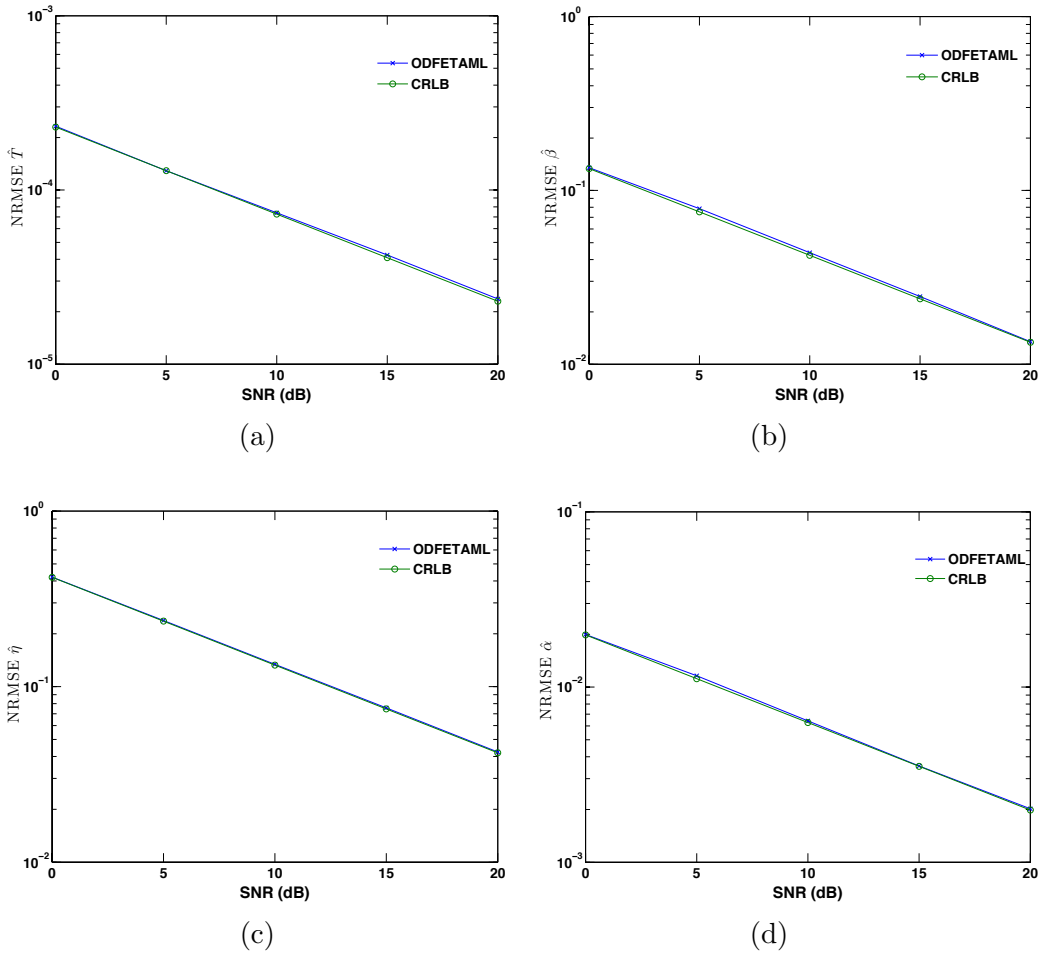

Figure 4.14: The NRMSE obtained by the ODFETAML algorithm, compared with the respective CRLB for the T, β, η and ρ parameters when $\Delta\nu = 0$ Hz; evaluation over $P = 1500$ Monte Carlo simulations.

Any variations in the expected NQR signal intensity, other than coming from the actual ingredients within the medicine, would have significant effects on the outcome of a detection/authentication analysis. As illustrated in Figures 4.10 - 4.12, even a small temperature uncertainty (e.g., order of 500 Hz) would have serious effects on the expected signal amplitude. Therefore, it is important to estimate the expected signal amplitude under several effects, for accurate quantitative outcomes. Herein, the additive noise of the signal may be well approximated as being a white Gaussian noise [Jakobsson et al., 2006]. The estimated amplitudes are then expected to lie within three standard deviations of the true amplitude, with a 99% probability. However, as the standard deviation is generally unknown, an estimate of the corresponding confidence interval is formed, using the refined

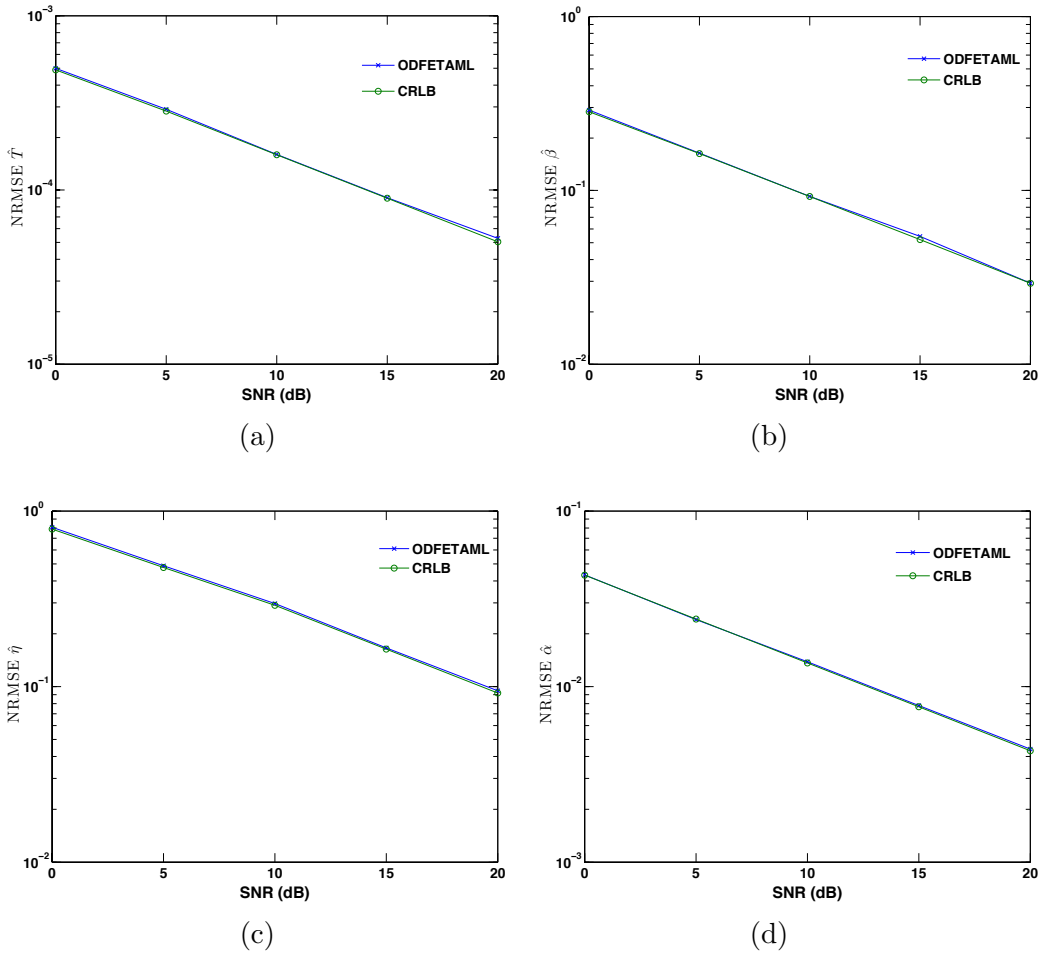

Figure 4.15: The NRMSE obtained by the ODFETAML algorithm, compared with the respective CRLB for the T, β, η and ρ parameters when $\Delta\nu = 1.7$ kHz; evaluation over $P = 1500$ Monte Carlo simulations.

CRLB of the signal magnitude, ρ, as a measure of the variance of the signal amplitude. Such a case is illustrated in Figures 4.17 - 4.19, which indicate the number of echo trains one needs to average over, in order to achieve a sufficiently strong SNR, with respect to the corresponding desired estimation accuracy in the signal amplitude. Real data were obtained, on resonance ($\Delta\nu = 0$ Hz), for sodium nitrite, metformin hydrochloride and aniracetam, using the PSL experimental parameters summarised in Tables 4.2, 4.6 and 4.8, respectively. However, here, full echo trains were obtained, with the NQR parameters, β, η, ρ and noise variance, being estimated using the proposed ODFETAML detection algorithm, by taking the average over 32 accumulations; that is, for a zero off-resonance frequency, this procedure is equivalent to the application of the FETAML algorithm proposed

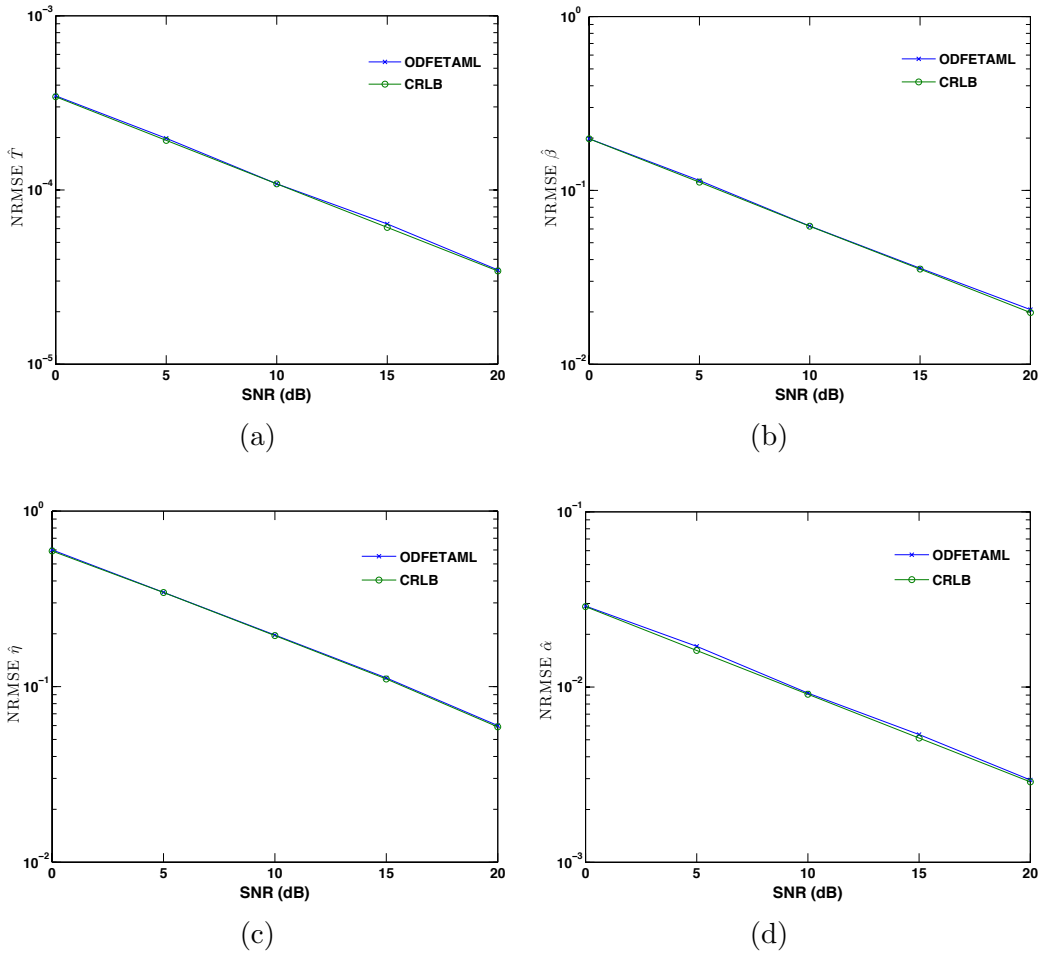

Figure 4.16: The NRMSE obtained by the ODFETAML algorithm, compared with the respective CRLB, for the T, β, η and ρ parameters when $\Delta\nu = 2.2$ kHz; evaluation over $P = 1500$ Monte Carlo simulations.

in Somasundaram et al. [2007]. The estimated parameters were then applied as the true parameters for the computation of the CRLB. Here, the first echo has been removed from the echo trains, as in practice, it can be significantly distorted by contributions from the FID [Somasundaram et al., 2007]. In Figure 4.17, the measurements (red circles), were averaged using a cross-validation scheme, when the temperature uncertainty, ΔT, was zero. Simply, starting from the bottom line, the real data of the amplitude estimation error were computed from each of the 32 echo trains. Next, the second line shows 32 data points, each of which represents the average of two measurements, randomly chosen among the 32 accumulations. Likewise, the third line of the real data, is the result of averaging three measurements, and so on, up to 31 averaged data points. The estimated

mean amplitude was then used as the true amplitude for the computation of the CRLB. The same steps were carried out for the other two materials, as seen in Figures 4.18 and 4.19. As expected, the CRLB accurately yields the expected variability of the signal amplitude. This result applies to all of the materials under study. However, in the presence of any uncertainty in the sample's temperature, off-resonance effects would significantly influence the expected estimated signal amplitude, and therefore affecting the overall estimation accuracy. To illustrate this effect, the CRLB was also computed in cases of temperature uncertainties (i.e., $\Delta T \neq 0$). As shown in Figure 4.17, the variability increases dramatically even for a small deviation of $\Delta T = 0.5$ K, that corresponds to 500 Hz off the resonance frequency. For $\Delta T = 0.5$ K, the expected signal magnitude decreases approximately by 50%, as compared with the maximum on-resonance value (see Figure 4.10). In particular, the CRLB for $\Delta T = 0.5$ K and $\Delta T = 1.5$ K, corresponds to the first two minima of the off-resonance profile in Figure 4.10, for sodium nitrite. Similarly, the bound was computed for the two frequency lines of metformin hydrochloride, in the presence of temperature uncertainty (see Figure 4.18). For the ν_{+1} line, $\Delta T = 0.5, 1, 1.5$ K (or $\Delta\nu \approx 80, 150, 250$ Hz), corresponding to $\sim 20\%$, 50% and 70% decrease in the expected signal intensity, respectively; whereas, for the ν_{+2} line, $\Delta T = 0.5, 1, 2$ K (or $\Delta\nu \approx 20, 45, 90$ Hz), corresponding to $\sim 3\%$, 30% and 45%, respectively. There is a significant change in the variability in both frequency lines, with the differences between them, mainly attributed to the different frequency shifting functions (see Table 4.5). Figure 4.19 illustrates the result for aniracetam. Here, the temperature uncertainty for the CRLB was $\Delta T = 0.5, 1, 1.5, 3$ K (or $\Delta\nu \approx 20, 40, 60, 140$ Hz), being related to $\sim 6\%$, 10%, 20% and 50% reduction in the expected amplitude, respectively. Small changes occur when the temperature is missed by 1.5 K, however, dramatic variation is observed in uncertainties above 3 K. Therefore, whenever there is an uncertainty in the temperature, one may need to acquire more echo trains to achieve the desired estimation accuracy to the same level, but always at the expense of longer experimental times.

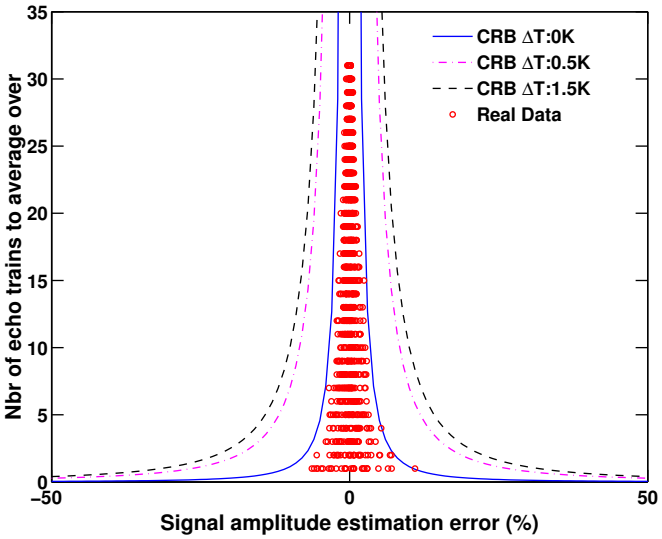

Figure 4.17: Estimation accuracy (99%) as determined using the CRLB of the signal intensities at various temperature uncertainties (ΔT). Comparison of the theoretical bounds and measurements for $\nu_{-} = 3615$ kHz frequency line of sodium nitrite.

4.7 Conclusions

In this chapter, the current state-of-the-art NQR echo train model was extended, to exploit the temperature dependence of the ^{14}N NQR signal amplitudes, as obtained using the PSL sequence [Somasundaram et al., 2007; Gregorovič and Apih, 2008]. Uncertainties in the sample's temperature during a measurement lead to uncertainties in the NQR resonance frequency. This dependency strongly affects the expected signal intensity, profoundly affecting the performance of existing detection and authentication algorithms. In fact, as described in Section 4.2, the signal amplitude follows a sinc-like function with periodicity due to the RF pulse spacings [Gregorovič and Apih, 2008, 2009b; Kyriakidou et al., 2014]. The amplitude modulation function has been validated using real measurements on powder sodium nitrite, metformin hydrochloride caplets and powder aniracetam. To the best knowledge of the author, no previous study has been published on the ^{14}N NQR of metformin hydrochloride and aniracetam, and in particular, on the off-resonance profiles of those materials. The results from the two lines of metformin hydrochloride, clearly illustrate how the relationship of the NQR linewidth and RF pulse spacing influences the off-resonance profile. This "feature" forms

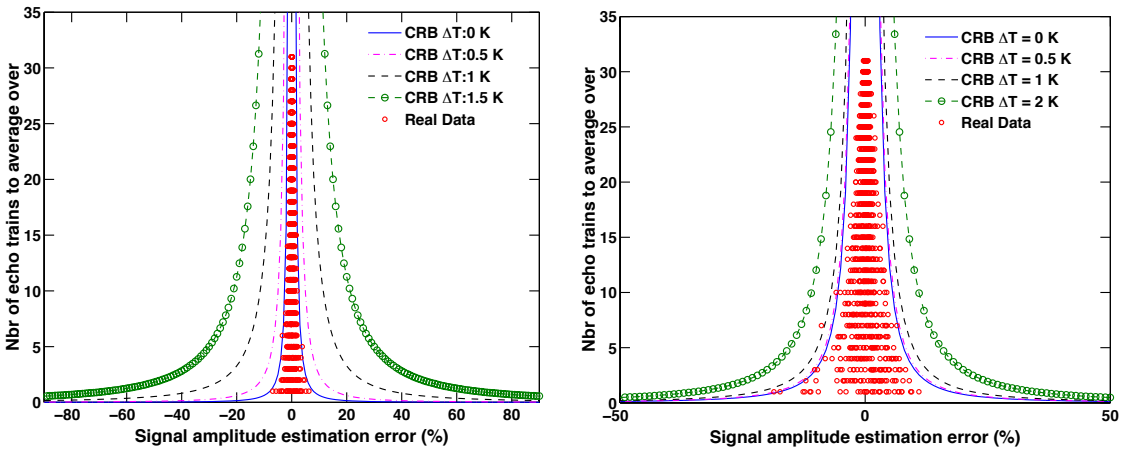

(a) (b)

Figure 4.18: Estimation accuracy (99%) as determined using the CRLB of the signal intensities at various temperature uncertainties (ΔT). Comparison of the theoretical bounds and measurements for (a) $\nu_{+1} = 2834$ kHz and (b) $\nu_{+2} = 2821$ kHz frequency lines of metformin hydrochloride.

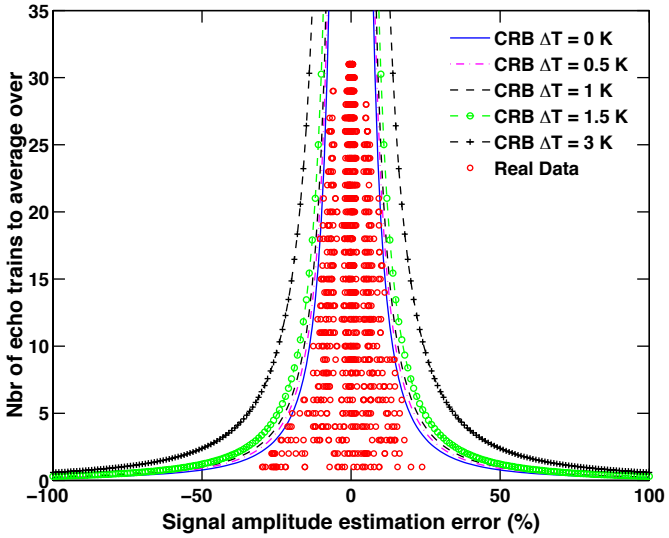

Figure 4.19: Estimation accuracy (99%) as determined using the CRLB of the signal intensities at various temperature uncertainties (ΔT). Comparison of the theoretical bounds and measurements for $\nu_{+} = 2553.1$ kHz frequency line of aniracetam.

a natural extension to the plethora of work outlined in Section 2.8, introducing the ODETAML detection algorithm, and its frequency selective counterpart, FODETAML. Therefore, the several algorithms developed in the literature can be extended correspondingly, creating for instance the ODRETAML, ODSEAQUER

and ODREMIQS, to mention just a few.

The proposed algorithm was evaluated using Monte Carlo simulated data. The refined model allows such algorithms to take the off-resonance effects into account, as an accurate modelling of the expected signal intensities, and the corresponding variance, given an uncertainty in the assumed temperature of the material. Such an uncertainty can often be as much as 0.5 K, which would affect the resulting SNR, as illustrated in the case of sodium nitrite. Furthermore, the CRLB of the refined model was derived and compared to the variance of the signal amplitude, given temperature uncertainties. The results may, for instance, be used to determine the required number of signal accumulations, to achieve the derived estimation accuracy, given an expected temperature uncertainty. For further improvement, future work would involve the implementation of the dependence of the relaxation time constant, T_{2e}, on the off-resonance frequency; an effect that, to a lesser extend, would influence the expected signal intensity. One would need to explain the relaxation in terms of all the dominant dipolar contributions (i.e., homonuclear and heteronuclear dipolar interactions).

Chapter 5

Discrimination of Paracetamol Batches

The variability between medicines produced by the same manufacturer can be a serious problem in the fight against low quality and counterfeit medicines. In this chapter, the batch-to-batch variability is examined using batches of analgesic paracetamol tablets. The chapter is organised as follows; Section 5.1 introduces the several factors that might influence the NQR signal parameters, followed by the motivation for this study. Sections 5.2 and 5.3 contain the experimental procedure and the numerical results from the statistical analysis, respectively. The conclusions are drawn in Section 5.4.

5.1 Introduction

The strategies for fighting counterfeit drugs are complex and challenging. Globalisation of this problem pose a significant threat to the public health that sometimes has fatal consequences. The different types of falsified drugs vary depending on the concentration of the API and the kind of excipients present in the product. A serious threat for pharmaceutical companies, is the so-called "high-quality" counterfeit pharmaceuticals. These may contain the correct or similar chemical composition but possibly differ in terms of their excipients, API, and conditions of manufacturing [Rodionova and Pomerantsev, 2010]. By exploiting the unique parameters of NQR signal, one may describe many of the physical and chemical properties of the crystalline samples. For instance, broadening of the NQR spectral line may be caused from defects or impurities present in the crystal [Balchin

et al., 2005; Barras et al., 2013; Latosińska, 2007a]. Often, pharmaceutical products are exposed to several factors that inevitably affect their "stability" and degradation. A few of those are the temperature, humidity, different processing conditions (i.e, pressure), and possibly, effects of ageing [Latosińska, 2007b; Latosińska and Latosińska, 2011]. Research studies report on the investigation of the influence of some of these factors on the quadrupolar frequency and relaxation time constants [Barras et al., 2013; Latosińska, 2007a; Lužnik et al., 2013; Ramu et al., 2010; Limandri et al., 2011; Mefed, 2015]. Lužnik et al. [2013] present linewidth variations which were caused from different compacting pressures and grinding during the tablets' production. Moreover, in Limandri et al. [2011], the authors studied and identified hydrates in ^{35}Cl nuclei, present in drugs containing diclofenac sodium. Gregorovič [2015] presents a quantitative analysis of hydration levels using ^{14}N NQR, in aminotetrazole and aminotetrazole monohydrate. The findings from these studies emphasise the application of NQR in quality control and monitoring of medicines during production stages and even storage. Latosińska [2007a] highlights the ability of NQR to analyse the thermal stability from several drugs by exploiting the influence of the temperature on the quadrupolar frequency. Moreover, these studies provide information on crystallographic changes such as the phase transitions of a polymorph. Improper monitoring and detection of crystallographic variations within a drug may have negative consequences on bioavailability; that is, the dose of a drug that enters the human system circulation and actually having an active effect.

Regarding ways of tackling the counterfeiting crime in real applications, a database must contain realistic"chemical fingerprints" of the medicines; for instance, the amount of active ingredient and formulation type of the commercial products. One major challenge that may hinder or limit the accurate authentication of a pharmaceutical, is the significant variability between medicines produced under the same processing conditions that have the same chemical formulation. That is, the batch-to-batch variability. This is more concerned with the presence of "high quality" fake products. Rodionova and Pomerantsev [2010] combine NIR with chemometric data processing methodologies, and highlight the issue of dealing with this kind of medicines. Moreover, the authors address the necessity for collection of a decent amount of data in order to test the natural variability within genuine drugs and investigate the batch-to-batch variability.

During the *shelf life* of medicines, the aforementioned factors might modify

their stability. Consider the scenario where a "fingerprint" of a medicine with a long shelf life is built during the early months of its life. If the medicine has degraded because of improper conditions during the later periods of its shelf life, then this chemical profile may no longer represent the actual crystalline state of the medicine. Therefore, a drug's bioavailability can be reduced if not monitored properly. In De Peinder et al. [2008], the authors present the study on the detection of Lipitor counterfeit medicines using NIR and Raman spectroscopy and indicate that storage conditions could be a significant factor of changes in a drug's stability.

This chapter examines the variability between batches using ^{14}N NQR. Analgesic paracetamol has a long shelf life (3 years) [GlaxoSmithKline Consumer Healthcare, 2012]. Herein, NQR signals where obtained from batches of paracetamol tablets that varied in terms of their expiry date. Two hypotheses are investigated: (a) the within-batches and (b) the batch-to-batch variability. The NQR signals were analysed using the proposed algorithm in Chapter 4. Multivariate analysis of variance (MANOVA) was used to examine any significant variations within the batches, by exploring the dependent variables (NQR signal characteristic parameters: signal amplitude, damping and echo train damping constants) across the between-group independent variable (batches or samples of one batch) [Bray and Maxwell, 1985; Anderson, 2003; Mayers, 2013].

In collaboration with the School of Engineering and Material Science at Queen Mary University, powder X-ray diffraction (XRD) was applied to extract diffraction patterns from two chosen batches. For the nature of this method, the samples were ground into powder. The real data were obtained by Dr Rory Wilson. Powder XRD provides distinctive diffraction patterns of many materials and characterises their crystalline structure. It was chosen as a method of support of the NQR findings. A brief introduction on powder XRD is included in Appendix C.

5.2 Experimental Procedure

5.2.1 NQR

Experiments were conducted on analgesic paracetamol (Figure 5.1) tablets, purchased from a shop in London. Paracetamol is on the WHO list of essential medicines [WHO, 2015]. The medicines were tested at the $\nu+$ NQR spectral line, 2.5624 MHz. Six different batches of paracetamol tablets were purchased and

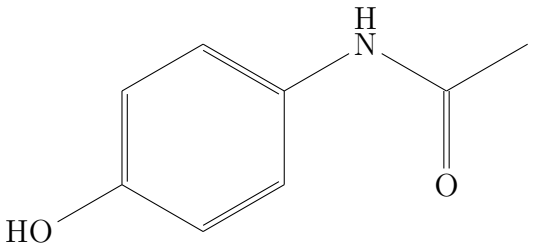

Figure 5.1: The molecular structure of paracetamol (acetaminophen).

chosen such that they differed in terms of their expiry date and batch number. Each batch contained two blister packs with total of 16 tablets $\times$ 0.5 g (see Figure 5.2(a)). For each batch, five more samples were also purchased. For the first hypothesis (within the same batch variability), the five samples of each of the six batches were examined. Next, for the second hypothesis (between different batches variability), the six batches were compared. The expiry dates of each of the six batches were: July 2014, August 2014, September 2014, October 2014, April 2015 and August 2016. Note that the NQR analysis was performed prior to the batches' expiry date. The measurements were conducted using the experimental equipment described in Section 3.3. No sample preparation was undertaken during the experiments. The blister packs were carefully inserted in the cylindrical fixed pitch coil, following a consistent "positioning" protocol (see Figure 5.2(b)). The temperature was controlled and stabilised during the measurements, following the procedure described in Section 3.2.

Figure 5.2(b) illustrates an intuitive setup followed in order to avoid significant temperature fluctuations in the remained empty space within the coil; the blister packs were attached on a plastic bottle filled with the silicone oil within the temperature control system. The temperature was kept monitored within 283 $\pm$ 0.5 K. The ^{14}N NQR signals were acquired using a PSL sequence. Table 5.1

(a)

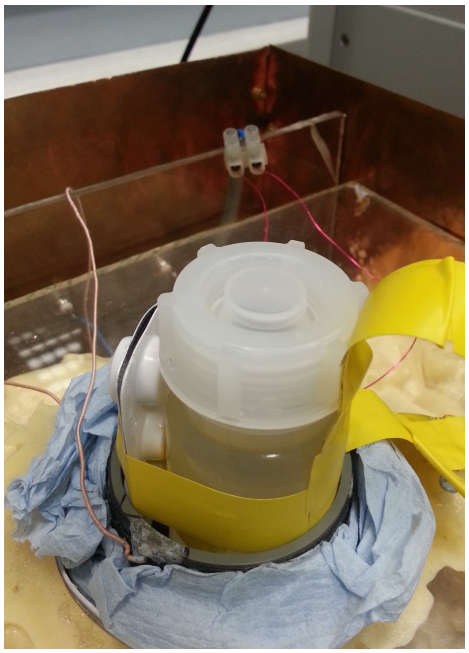

(b)

Figure 5.2: (a) Packs of analgesic paracetamol tablets; (b) Setup of one batch of paracetamol tablets within the coil.

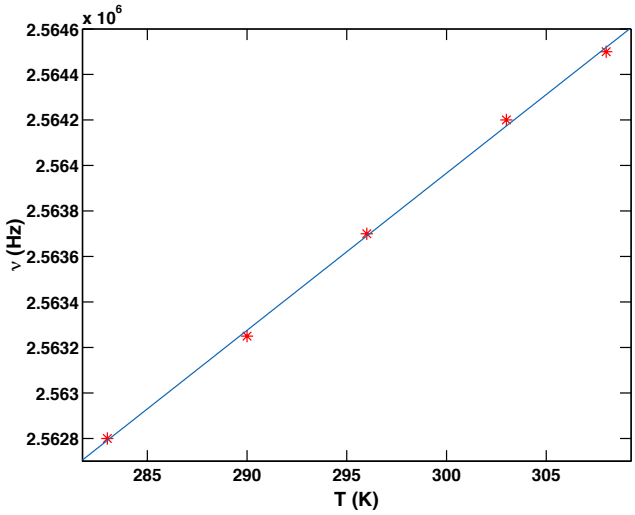

Figure 5.3: Resonance frequency versus temperature for the $\nu+$ NQR spectral line of analgesic paracetamol tablets; linear fit using $\omega = a - bT$ ($\omega = 2\pi\nu$).

Table 5.1: PSL experimental parameters

excitation frequency (MHz)	2.562
pulse width (µs)	60
τ spacing (µs)	1103
echo spacing (µs)	2206
dwell time (µs)	6
dead time (µs)	304
acquisition delay (µs)	306
acquisition time (µs)	1536
number of echoes	1024
samples per echo	256
scans	32

summarises the pulse sequence parameters. Moreover, the frequency shifting function of the examined line is shown in Figure 5.3, for the range $T = 283{-}310$ K. The temperature coefficients were determined using (4.4) and computed as $a = 2.543$ MHz and $b = -0.069$ kHz/K.

5.2.2 X-ray Diffraction

The diffraction patterns were collected on a Panalytical X' Pert Pro powder diffractometer in Bragg-Brentano θ/θ reflection geometry. The data were obtained using three samples; pure acetaminophen in powder form and two different batches of paracetamol tablets. The two batches were chosen following the NQR data analysis which revealed differences in their spin-phase memory decay time, T_2^* (or equivalently, β damping parameter), as discussed in Section 5.3.2. The expiry date corresponding to each of the two batches is September 2014 and August 2016, respectively. For powder XRD, the paracetamol tablets were ground into powder manually. The samples were mounted on zero background silicon single crystal substrates, by sprinkling on as a fine powder onto a thin layer of grease on the substrate surface. During the data collection, the sample is rotated in its plane, to improve the powder statistics and to reduce any texture to cylindrical symmetry, which is easier to model, if required.

The generator was set at an anode current 40 mA and voltage 45 kV. The target material was copper with characteristic wavelength $\lambda = 0.15418$ Å ($\mathrm{CuK}_{\alpha_1} = 1.5406$ Å, $\mathrm{CuK}_{\alpha_2} = 1.5444$ Å, $\mathrm{CuK}_{\beta} = 1.3922$ Å). The incident beam is normally collimated with 0.02 rad Soller slits (parallel copper plates), a 10 mm mask and 1/4° fixed divergence slit. The scattered beam is collimated by automated slits (fixed at 1/2°) and 0.02 rad Soller slits with a nickel (Ni) filter to remove the CuK_{β} radiation. The scattering angle 2θ was set at a range of 5° – 70° in steps of 0.033°. The detector is a Panalytical X' Celerator solid state real time and multiple strip (RTMS), which continuously scans over a range of 2.12°, consisting of 128 individual solid state detectors. Therefore, the data were collected very rapidly. Appendix C provides all the fundamental information on the concept of X-ray Diffraction.

5.3 Results

5.3.1 NQR – Hypothesis: Within batches variability

The data were analysed and the vector of unknown parameters was estimated using the ODFETAML detection algorithm. The parameter vector includes the unknown sinusoidal damping constant, β, the echo damping constant, η, and the magnitude scaling due to the SNR, ρ. A search region over temperature was

selected as $[282.5, 283.5]$ K in 500 steps. With prior knowledge on the relaxation time constants (T_2^* and T_{2e}) of paracetamol tablets, for the particular experimental setup, one can set lower bounds on the sinusoidal damping parameters. The algorithm used a search region of $\beta = [0.01, 0.1]$ and $\eta = [1 \times 10^{-6}, 1 \times 10^{-5}]$, in 1000 and 2000 steps, respectively. The NQR signals were obtained from five samples for each of the six batches. The spectra were repeated 20 times per sample during different times and days.

The proposed hypothesis was tested using MANOVA. The objective is to describe the effect of the independent variable (e.g., samples for the batch with expiry date August 2014) upon the combination of the dependent variables. The null hypothesis states that the three-dimensional mean vector of β, η and ρ is the same for all the five samples of each of the six batches. One-way MANOVA was performed using the R software [1], with the three-dimensional mean vector set as the vector of dependent variables. A number of assumptions were considered before performing MANOVA [Mayers, 2013] (see Appendix B for further details on MANOVA assumptions). For $N = 20$ observations per sample (for each batch), normality was checked using Kormogorov-Smirnov [Lilliefors, 1967], Shapiro-Wilk [Shapiro and Wilk, 1965] and Anderson-Darling [Anderson and Darling, 1954] tests. Also, the Mardia's [Mardia, 1974] and Henze-Zirkler's tests [Henze and Zirkler, 1990] were applied to test multivariate normality using the Multivariate Normality (MVN) package in R [Selcuk et al., 2015]. The Levene's test was used to measure the homogeneity of univariate between-group variance [Levene, 1960]. Next, the homogeneity of variance–covariance was tested using the Box'm test [Box, 1949; Mayers, 2013]. Due to the equal group sizes (20 observations per sample), mild violations of this assumption have no significant influence on the statistical outcome. For MANOVA outcomes to be meaningful, there should be a moderate correlation between the dependent variables. This assumption was checked using Pearson's correlation [Johnson et al., 1992]. First, a visual interpretation of the results is shown in Figures 5.4–5.9, which illustrate the means and standard deviations of the estimated parameters for the examined number of samples.

Next, the Wilks's λ and Pillai's Trace statistical tests [Johnson et al., 1992] were used to determine any statistical significant variability. Table 5.2 summarises

[1] R is a language and environment for statistical computing and graphics [The R foundation, 2016].

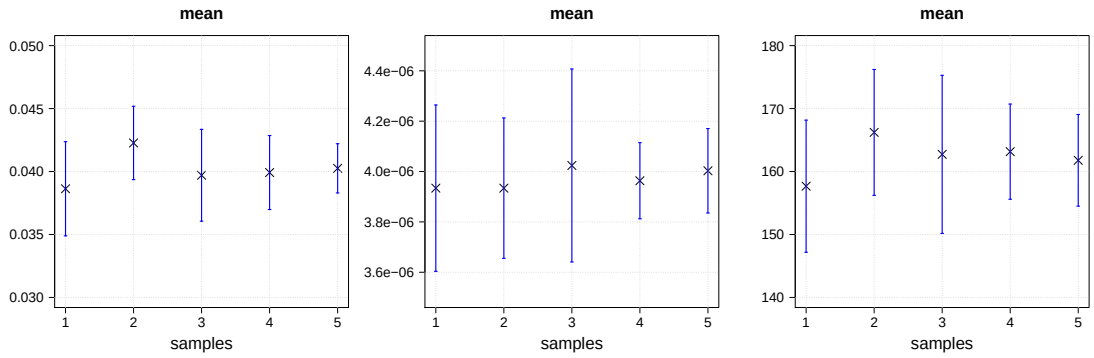

(a) β (b) η (c) ρ

Figure 5.4: Mean values of (a) β, (b) η , (c) ρ with respect to samples for the batch September 2014. Error bars represent $\pm$ the standard deviations.

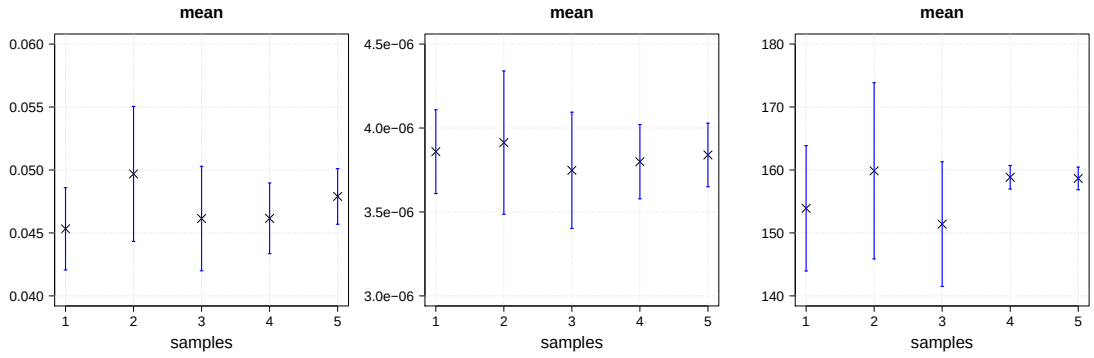

(a) β (b) η (c) ρ

Figure 5.5: Mean values of (a) β, (b) η , (c) ρ with respect to samples for the batch August 2016. Error bars represent $\pm$ the standard deviations.

the results of the one-way MANOVA analysis for each of the six different batches. Note that for each sample of each batch, the experiment was repeated 20 times. Therefore the "statistical" sample size per batch is $N = 100$. For each of the two tests, the corresponding F-statistic and probability values are illustrated. In conducting the hypothesis test, the p-values are compared with the threshold value, α; that is, the probability of rejecting the null hypothesis when it is actually true. The number of asterisks in Table 5.2 is associated with the level of statistical significance.

As illustrated, the p-values do not attain a statistically significant difference in the three variables between the five samples. This applies for all the six different batches, with different expiry date and batch number. There seems to be no

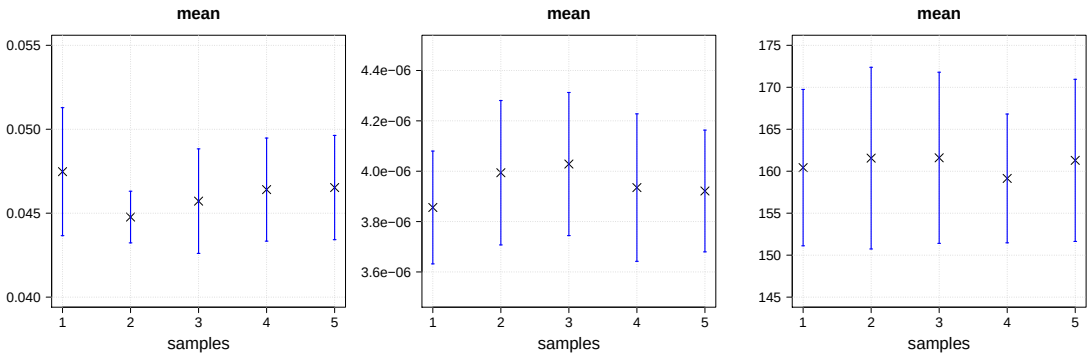

(a) β (b) η (c) ρ

Figure 5.6: Mean values of (a) β, (b) η , (c) ρ with respect to samples for the batch April 2015. Error bars represent $\pm$ the standard deviations.

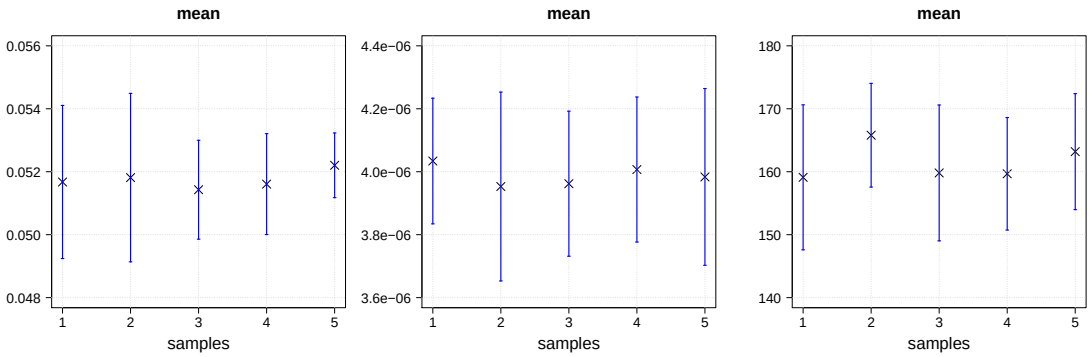

(a) β (b) η (c) ρ

Figure 5.7: Mean values of (a) β, (b) η , (c) ρ with respect to samples for the batch August 2014. Error bars represent $\pm$ the standard deviations.

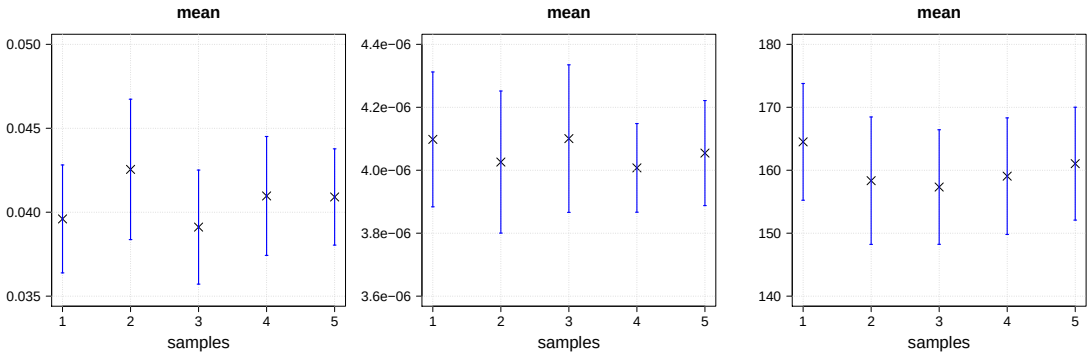

(a) β (b) η (c) ρ

Figure 5.8: Mean values of (a) β, (b) η , (c) ρ with respect to samples for the batch July 2014. Error bars represent $\pm$ the standard deviations.

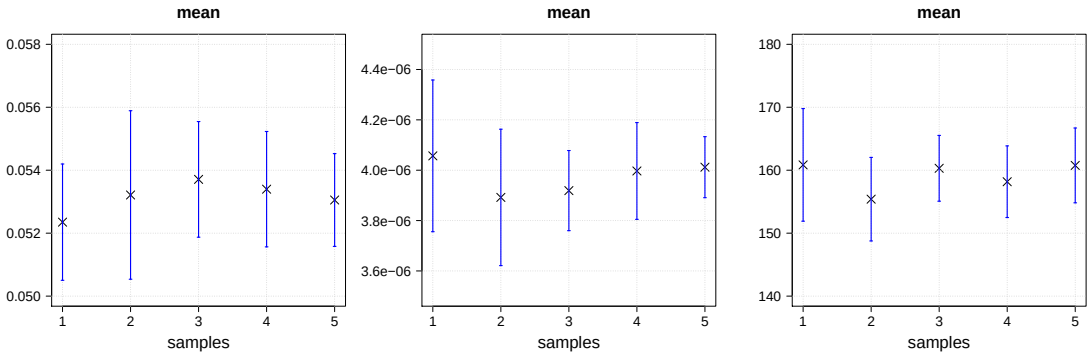

(a) β (b) η (c) ρ

Figure 5.9: Mean values of (a) β, (b) η , (c) ρ with respect to samples for the batch October 2014. Error bars represent $\pm$ the standard deviations.

Table 5.2: MANOVA: within batches comparison.

batch label	categorical variable	statistic[a]		F	Pr(>F)[b]
1	samples	W	0.9916	0.2704	0.8466
		P	0.0084	0.2704	0.8466
2		W	0.9408	2.0113	0.1175
		P	0.0591	2.0113	0.1175
3		W	0.9929	0.2258	0.8783
		P	0.0071	0.2258	0.8783
4		W	0.9721	0.9170	0.4357
		P	0.0278	0.9170	0.4357
5		W	0.9858	0.4606	0.7104
		P	0.0142	0.4606	0.7104
6		W	0.9639	1.1991	0.3144
		P	0.0361	1.1991	0.3144

[a] W = Wilks's λ; P = Pillai's Trace.

[b] Level of significance: $***$, p<0.001; $**$, p<0.01; $*$, p<0.05; no asterisk p<0.1

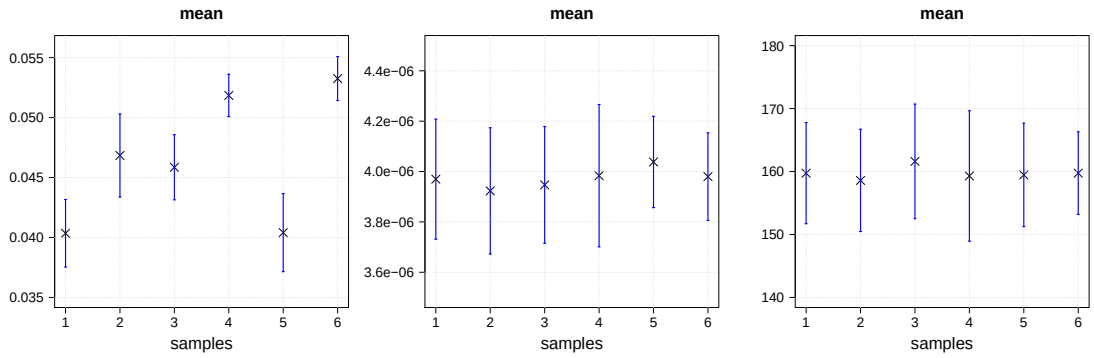

(a) β (b) η (c) ρ

Figure 5.10: Mean values of (a) β, (b) η , (c) ρ with respect to six batches; (1) September 2014, (2) August 2016, (3) April 2015, (4) August 2014, (5) July 2014 and (6) October 2014. Error bars represent $\pm$ the standard deviations.

significant multivariate effect and the null hypothesis fails to be rejected. As expected, the result indicates the natural variability in the manufacturing of the generic samples, produced under the same conditions.

5.3.2 NQR – Hypothesis: Between batches variability

This section examines the second hypothesis which states that the three - dimensional variable mean vector is the same among the six different batches. As in Section 5.3.1, the parameters were estimated using the ODFETAML, with the same search regions for the temperature and damping constants. Figure 5.10 illustrates the mean values for the three estimated parameters among the six batches of different expiry dates. At a first glance, there is an evident variability in the estimated β parameters (Figure 5.10(a)). Note that the sample size per batch is now $N = 100$ (i.e., 20 measurements for each of the five samples of each individual batch).

A scatter plot with the associated marginal histograms of the damping constant β with respect to η, is illustrated in Figure 5.11. Herein, despite the small degree of overlap between the β estimates, there is a distinct difference among the six batches, which needs to be statistically validated. One-way MANOVA was performed using the "batches" as the categorical variable, for a total sample size $N = 600$. The Wilks's λ and Pillai's Trace [Johnson et al., 1992] were applied to investigate how the batches have an impact upon the combination of the three dependent variables. The outcome of the MANOVA analysis is illustrated

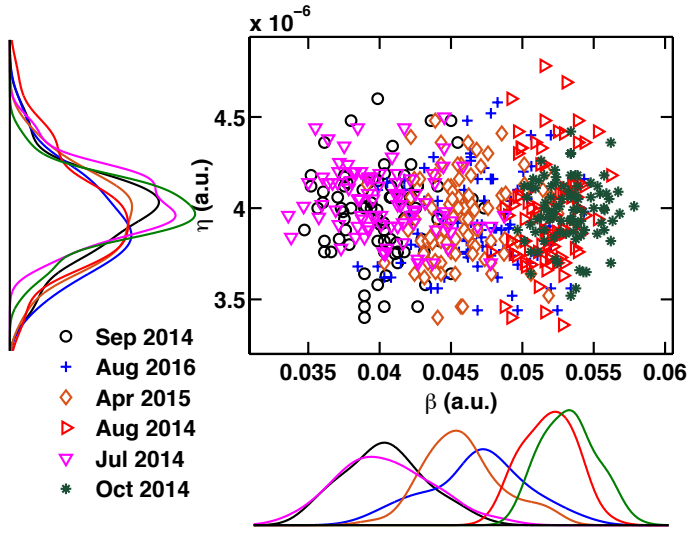

Figure 5.11: Scatter plot of β with respect to η dependent variable for the six different batches of paracetamol, with their corresponding marginal histograms.

Table 5.3: MANOVA: between batches comparison.

categorical variable	Statistic[a]	F	Pr(>F)[b]
batches	W 0.198	78.094	2.2×10^{-16} ***
	P 0.834	41.158	2.2×10^{-16} ***

[a] W = Wilks's λ; P = Pillai's Trace
[b] Level of significance: ***, p<0.001; **, p<0.01; *, p<0.05; no asterisk p<0.1

Table 5.4: Univariate ANOVAs: between batches comparison – Wilks's λ.

variables	F	Pr(>F)[a]
ρ	1.276	0.272
η	2.577	0.025 *
β	364.2	2.2×10^{-16} ***

[a] Level of significance: ***, p<0.001; **, p<0.01; *, p<0.05; no asterisk p<0.1

in Table 5.3. The p-values associated with both of the test criteria is very small ($p = 2.2 \times 10^{-16}$), indicating a significant discrimination even for $\alpha = 0.001$; therefore, the null hypothesis is rejected. Again, note that the number of asterisks in Table 5.3 represent the level of statistical significance. Next, the univariate test is explored to determine the effect of the batches (independent variable) against each of the parameters separately. The outcome from the univariate ANOVA test on each variable, is shown in Table 5.4. The Wilks's λ test criterion was used. There is a significant univariate effect for the damping constant β, with

Table 5.5: Tukey's Post-Hoc Test for the β variable.

expiry date	mean difference	CI	Pr
Aug 2014 – Apr 2015	0.0059	[0.0048 , 0.0071]	0.0000
Aug 2016 – Apr 2015	0.0009	[-0.0001 , 0.0021]	**0.1486**
Jul 2014 – Apr 2015	-0.0054	[-0.0066 , -0.0043]	0.0000
Oct 2014 – Apr 2015	0.0074	[0.0062 , 0.0085]	0.0000
Sep 2014 – Apr 2015	-0.0055	[-0.0066 , -0.0043]	0.0000
Aug 2016 – Aug 2014	-0.0050	[-0.0061 , -0.0038]	0.0000
Jul 2014 – Aug 2014	-0.0144	[-0.0126 , -0.0103]	0.0000
Oct 2014 – Aug 2014	0.0014	[0.0002 , 0.0026]	**0.0074**
Sep 2014 – Aug 2014	-0.0115	[-0.0126 , -0.0103]	0.0000
Jul 2014 – Aug 2016	-0.0064	[-0.0076 , -0.0053]	0.0000
Oct 2014 – Aug 2016	0.0064	[0.0052 , 0.0076]	0.0000
Sep 2014 – Aug 2016	-0.0065	[-0.0077 , -0.0053]	0.0000
Oct 2014 – Jul 2014	0.0128	[0.0117 , 0.0174]	0.0000
Sep 2014 – Jul 2014	-0.0000	[-0.0012 , 0.0011]	**0.9354**
Sep 2014 – Oct 2014	-0.0129	[-0.0140 , -0.0117]	0.0000

$p < 0.001$, as compared with η and ρ parameters.

Following a statistically significant outcome, a post-hoc test is commonly applied to explore the source of variation; i.e., the test is used to locate the source of difference among the six batches. The Tukey's [Tukey, 1949] and Games-Howell [Games and Howell, 1976] post-hoc tests were used. Only the Tukey's test is presented, since the outcomes from both tests were the same. Here, the hypothesis states that pairwise combinations are equal, for a significance level $\alpha = 0.05$. Tables 5.5, 5.6 and 5.7, illustrate the results computed from the Tukey's post-hoc test for β, η and ρ, respectively. The results indicate the mean differences of all the combinations, the adjusted confidence intervals [CI=$100(1-\alpha)$] and the corresponding probability values. The results are also illustrated graphically in Figure 5.12. In Table 5.5, the p-values indicate significant effects for most of the pairs; that is, most of the pairwise combinations reject the null hypothesis, showing a noteworthy difference among them due to the β variable. For the combinations Aug 2016/Apr 2015 and Sep 2014/Jul 2014, the null hypothesis fails to be rejected. Figure 5.11 clearly illustrates this result. As expected, the post-hoc analysis on the univariate outcomes for η and ρ, show no evidence of significant variations between the pairwise combinations of the six batches (Tables 5.6, 5.7 and Figures 5.12(b) and 5.12(c)).

The statistical analysis revealed significant variability between the six batches. Herein, the factor responsible for the observed variability is not known. However,

Table 5.6: Tukey's Post-Hoc Test for the η variable.

expiry date	mean difference	CI	Pr
Aug 2014 – Apr 2015	3.6666×10^{-08}	[-6.1221e-08 , 1.3455e-07]	0.8926
Aug 2016 – Apr 2015	-2.3777×10^{-08}	[-1.2166e-07 , 7.4110e-08]	0.9825
Jul 2014 – Apr 2015	9.1000×10^{-08}	[-6.8878e-09 , 1.8888e-07]	0.0854
Oct 2014 – Apr 2015	3.2888×10^{-08}	[-6.4998e-08 , 1.3077e-07]	0.9299
Sep 2014 – Apr 2015	-2.2777×10^{-08}	[-7.5110e-08 , 1.2066e-07]	0.9855
Aug 2016 – Aug 2014	-6.0444×10^{-08}	[-1.5833e-07 , 3.7443e-08]	0.4887
Jul 2014 – Aug 2014	5.4333×10^{-08}	[-4.3554e-08 , 1.5222e-07]	0.6071
Oct 2014 – Aug 2014	-3.7777×10^{-09}	[-1.0166e-07 , 9.4110e-09]	0.9999
Sep 2014 – Aug 2014	-1.3888×10^{-08}	[-1.1177e-07 , 8.3998e-08]	0.9986
Jul 2014 – Aug 2016	1.1477×10^{-07}	[1.6889e-08 , 2.1266e-07]	0.0109
Oct 2014 – Aug 2016	5.6666×10^{-08}	[-4.1221e-08 , 1.5455e-07]	0.5618
Sep 2014 – Aug 2016	4.6555×10^{-08}	[-5.1332e-08 , 1.4444e-07]	0.7507
Oct 2014 – Jul 2014	-5.8111×10^{-08}	[-1.5599e-07 , 3.9776e-08]	0.5337
Sep 2014 – Jul 2014	-6.8222×10^{-08}	[-1.6611e-07 , 2.9665e-08]	0.3474
Sep 2014 – Oct 2014	-1.0111×10^{-08}	[-1.0799e-07 , 8.7776e-08]	0.9997

Table 5.7: Tukey's Post-Hoc Test for the ρ variable.

expiry date	mean difference	CI	Pr
Aug 2014 – Apr 2015	-2.3131	[-5.926966 , 1.300665]	0.4468054
Aug 2016 – Apr 2015	-3.0210	[-6.634889 , 0.592741]	0.1611883
Jul 2014 – Apr 2015	-2.1464	[-5.760269 , 1.467361]	0.5331694
Oct 2014 – Apr 2015	-1.8641	[-5.477920 , 1.749711]	0.6802430
Sep 2014 – Apr 2015	-1.8691	[-5.482957 , 1.744673]	0.6777037
Aug 2016 – Aug 2014	-0.7079	[-4.321739 , 2.905891]	0.9934586
Jul 2014 – Aug 2014	0.1666	[-3.447119 , 3.780512]	0.9999944
Oct 2014 – Aug 2014	0.4490	[-3.164769 , 4.062861]	0.9992550
Sep 2014 – Aug 2014	0.4440	[-3.169807 , 4.057823]	0.9992948
Jul 2014 – Aug 2016	0.8746	[-2.739195 , 4.488436]	0.9827913
Oct 2014 – Aug 2016	1.1569	[-2.456845 , 4.770785]	0.9424678
Sep 2014 – Aug 2016	1.1519	[-2.461883 , 4.765747]	0.9434930
Oct 2014 – Jul 2014	0.2823	[-3.331466 , 3.896165]	0.9999236
Sep 2014 – Jul 2014	0.2773	[-3.336504 , 3.891127]	0.9999301
Sep 2014 – Oct 2014	-0.0050	[-3.618853 , 3.608777]	1.0000000

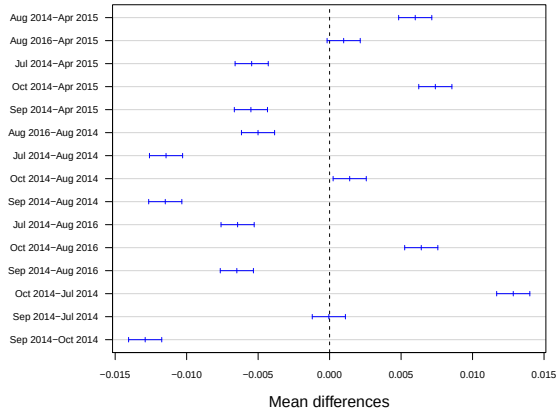

(a) β

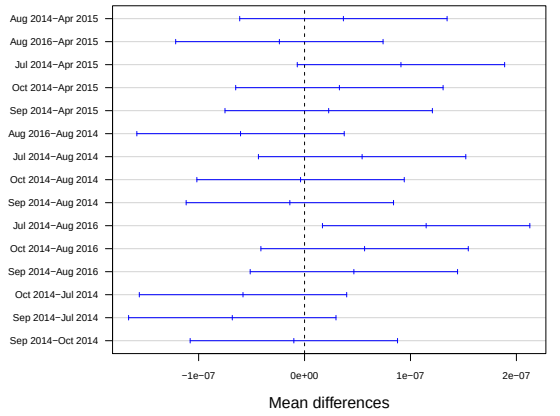

(b) η

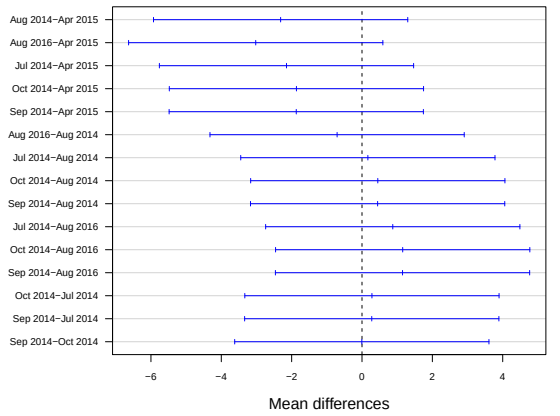

(c) ρ

Figure 5.12: Pairwise combinations versus mean differences for (a) β, (b) η and (c) ρ parameters, obtained from the Tukey's post hoc test.

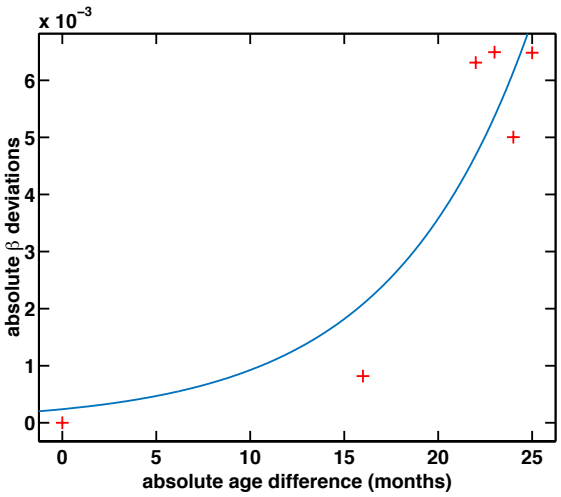

Figure 5.13: Absolute age difference versus the associated absolute β deviations from the reference/newest batch (red crosses). For illustration purposes, a possible exponential fit is shown (blue curve).

the different expiry dates is a known fact. Therefore, in more specific words, the ageing of the medicine could possibly be one factor. In Figure 5.11, for the most recent batch (August 2016), the discriminant parameter β seems to lie in the middle from the rest of the batches. If one considers the newest batch, August 2016, as an "age reference point", the deviations of the other batches from this point can be computed. In Figure 5.13, the absolute age differences (in units of months), with respect to the analogous deviations of the β variable are shown. Despite the fact that the number of points is small, a correlation between the absolute β deviations and the absolute age differences is observed. This correlation could perhaps be modelled as an exponential decay. For illustration purposes, an exponential fit is shown in Figure 5.13. Possibly, the damping parameter could be an indicator of the influence of ageing on the crystalline structure of the medicines. For a complete and solid conclusion, a larger number of batches at a wider range of expiry dates should be explored.

It is accepted that the SNR is proportional to the square root of the number of signal accumulations. The number of scans used in the pulse sequence, determines the degree of estimation accuracy. Considering the scattering of the batches shown in Figure 5.11, one may choose the number of signal accumulations that will define how well the cluster separation will be. The higher the SNR, the less "spread" and more accurate the estimated parameters will be. Theoretically, the CRLB is used to determine the variance of the estimated parameters, by

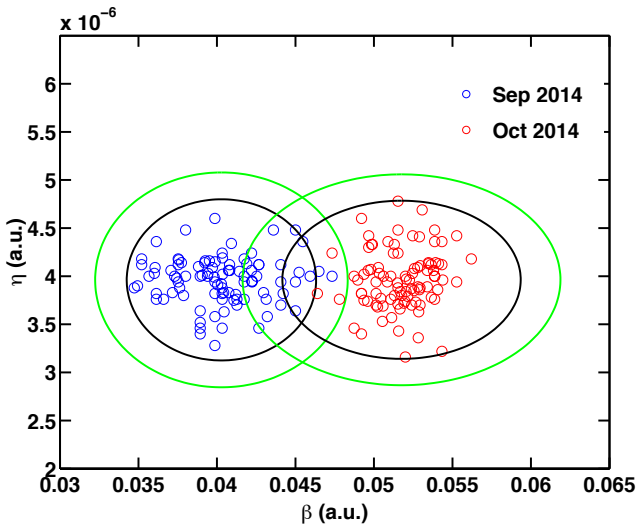

Figure 5.14: Scatter plot of β vs η variables for two batches (Sep 2014 and Oct 2014), along with their corresponding CRLB ellipses for two values of S/Ns.

computing the lower bound on the least achievable variance of any unbiased estimator. The SNR of the measurements is computed to be -24 ± 2 dB, using the definition in (4.60). The CRLBs for the two batches, September 2014 and October 2014, were computed for SNR $= -24$ dB (see Section 4.4). Figure 5.14 shows the β versus η parameter for the two batches, with their corresponding CRLB ellipsoids. The ellipsoids indicate that about 99% of the data are expected to lie within these margins. The estimated values show a good correlation with the theoretical CRLB ellipsoids. The CRLBs were also plotted for SNR $= -30$ dB. The theoretical variance computed with the CRLB is correlated with the SNR [Kyriakidou et al., 2014]. The higher the SNR, the better the estimation accuracy and the "tighter" the ellipsoids must be, and vice versa. Consequently, one may need to acquire more signal accumulations to achieve a desired estimation accuracy and greater differentiation between the examined batches.

5.3.3 X-ray Diffraction Results

For powder XRD, three samples were used in powder form; pure acetaminophen (reference pattern) and the two batches with expiry date September 2014 and August 2016. The diffraction patterns were obtained by plotting the intensity of the spectra with respect to the diffraction angle 2θ, as illustrated in Figure 5.15.

The diffraction patterns seem identical – same phase – with a notable difference in the intensity. The number and shape of the diffraction peaks are very similar for the three materials. Note that the width of the peaks depends on the number of crystallographic planes whereas their sharpness depends on the size of crystalline molecules (see Appendix C) [Suryanarayana and Norton, 2013]. With the diffraction pattern of pure acetaminophen set as the reference pattern, one may conclude that the spectra from the two different batches do not reveal any structural differences in their crystals. Many factors might influence this variation in the intensities of the XRD patterns. The manual grinding of the paracetamol tablets may have caused a slight variation in the thickness of the layer on the substrate. Another reason may be the preferred orientation or the fact that there are not enough randomly oriented crystallites. The X-ray diffraction patterns between the two batches of different expiry date, did not reveal any crystalline variations, as compared with NQR. Perhaps, this is attributed to the higher sensitivity of NQR spectroscopy.

5.4 Conclusion

In this chapter, a number of paracetamol batches with different use-by dates were analysed using NQR. The estimated parameters were explored using MANOVA. The hypothesis of the within-batches variation fails to be rejected on the one-way MANOVA test. The observed variation is possibly an evidence of the natural variability among genuine medicines. On the other hand, there is statistically efficient discrimination between the batches with different expiry dates. Therefore, the findings confirm the batch-to-batch variability. Herein, the sinusoidal damping constant β, was the control discriminatory parameter. Moreover, it could be a possible indicator of the ageing influences on the physical and chemical properties of the compound. The findings strongly suggest that such a study would be worthwhile. More batches from other manufacturers and a wider range of expiry dates should be collected and analysed. Moreover, the study is not limited only to analgesic paracetamol tablets. Variations in the crystalline structure are observed in all the materials and should be exploited correspondingly. As a further step, a number of analytical techniques should be employed to chemically identify the actual source of variation among the different batches.

The ability to provide knowledge on medicines' degradation and how factors

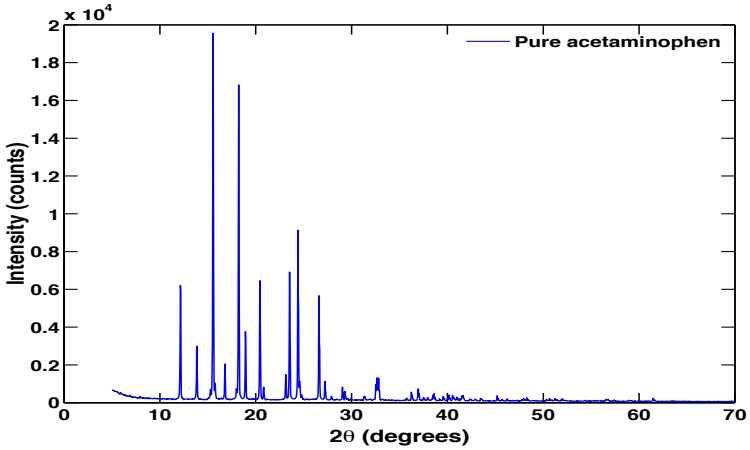

(a) pure acetaminophen

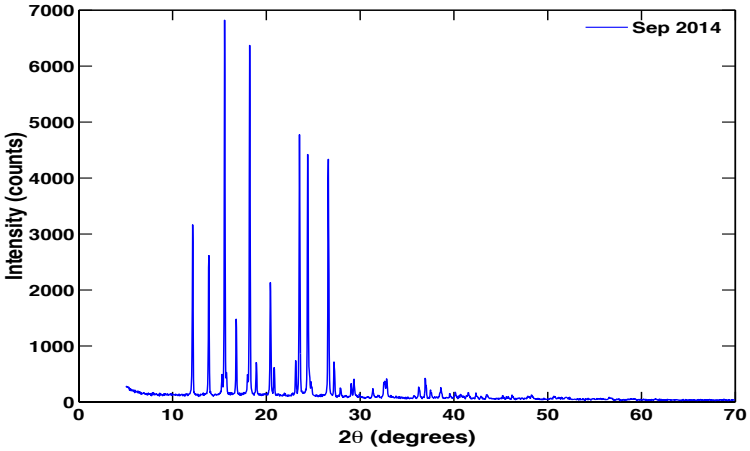

(b) ground paracetamol; expiry date: September 2014

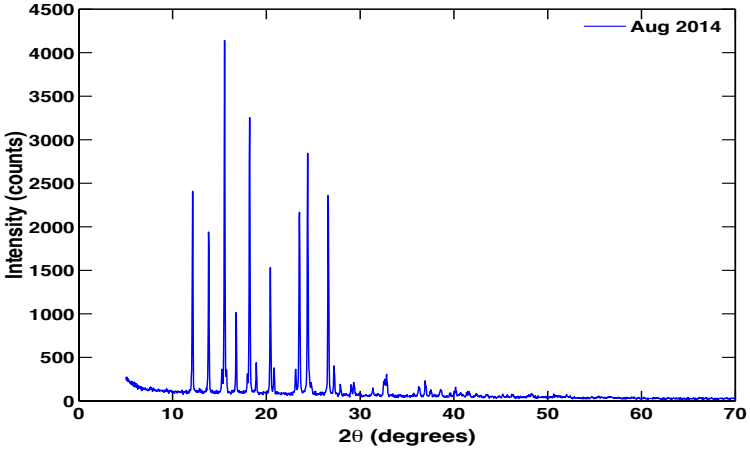

(c) ground paracetamol; expiry date: August 2016

Figure 5.15: Powder X-ray diffraction patterns.

such as temperature, ageing, storage conditions, humidity influence bioavailability is crucial. The capabilities of NQR could possibly be applied in the concept of "*medicines recycling*". From the manufacturing step of the quality assurance process, where a medicine is produced, until the product reaches the patient's hands, there are certain procedures followed to ensure the highest standards in the product's quality. In authentication, a database will contain chemical profiles of the medicines. These "fingerprints" may simply contain a barcode placed on the pack at the production stage, or they may also represent a complete chemometric profile of monadical spectroscopic parameters. NQR is a powerful candidate for generating such unique features for materials even at the level of batches of the same manufacturer. There is a point during the quality assurance stage of the drugs, where the packaged medicines are analysed and the question "do the contents match the label?" is tested. For instead, this occurs at the European Union borders at the airport checks. The findings of this study rise the potential of applying NQR spectroscopy after the final stage of the quality assurance process. What about unused medications that reach, but never be consumed by the patient? The National Health Service (NHS) in England states that the waste of unused prescription medicines reaches 300 million pounds per year [BMA, 2011; Pencheon, 2012]. One reason is the inability of patients to return unopened medicines. In addition, regulations do not permit the reuse of the medications as their quality cannot be guaranteed. Degradation of medicines under unknown storage conditions may affect the biodisponibility and bioavailability of the active substance, creating a risk in patients' health. Dr David Pencheon, Head of the NHS Sustainable Development Unit, suggests the use of medicines recycling [Pencheon, 2012]. Unused prescription medications should be returned to the NHS, where a safety check will be applied that guarantees the reuse from patients. Since physical inspection may not assure the quality of medicines, the necessity of a non-invasive and non-destructive method is essential. NQR could possibly be applied in analysing unused medications and generating a database on safe reused medicines with perhaps a "new expiry date". New research questions should be addressed regarding this area, checked for potential benefits and highlight any controversies that may hinder this application.

Chapter 6

Optimising the utility of signal processing methods through pulse sequence design

This study presents flexible methodologies that seek to identify limits in the accuracy of the estimated damping constants. Being able to determine such limits, the utility of the chosen signal processing method is optimised through conditions which help to design a pulse sequence. The chapter is organised as follows: Section 6.1 provides an introduction to the concerned issues. In Section 6.2, the experimental procedure and results from the study of the effect of a short acquisition window on the sinusoidal damping constant is provided. Moreover, in Section 6.3, the accuracy of the estimated echo train decay constant is explored when the NQR echo train contains fewer echoes. The experimental procedure and the results from several materials is included.

6.1 Introduction

In medicines authentication, accurate and reliable "fingerprints" of the original genuine medicines are to be compared with the responses from other drugs under examination. The NQR relaxation parameters provide information on the conditions during the processing stages and can be used to build the chemical profiles of the medicines [Barras et al., 2012a; Latosińska, 2007a; Kyriakidou et al., 2015]. As discussed in previous chapters, these NQR parameters are the spin-phase (T_2^*)

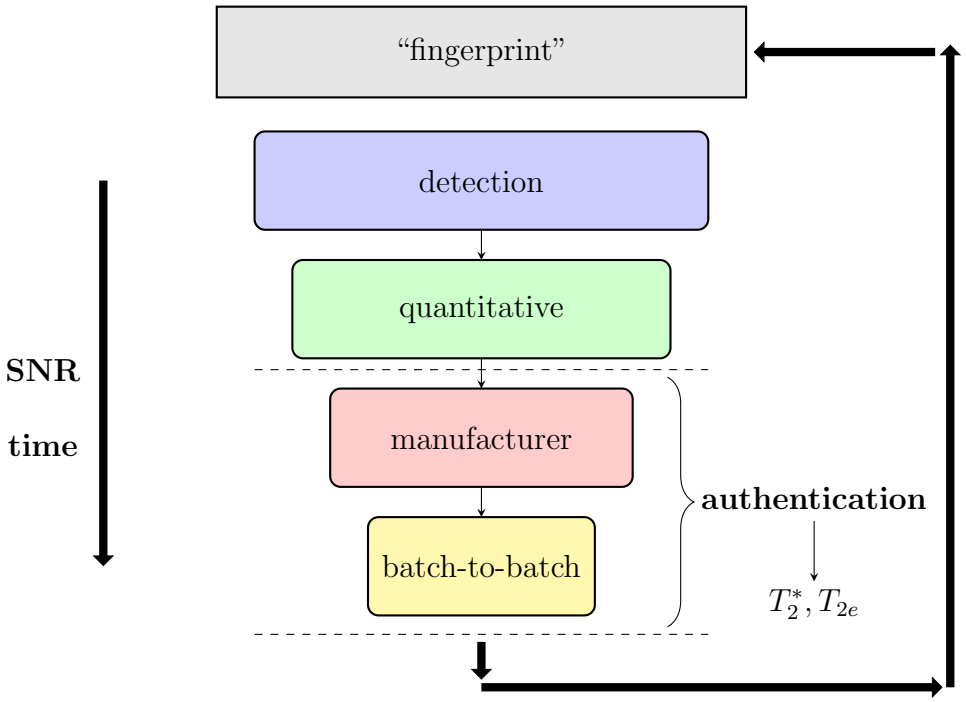

Figure 6.1: Simple block diagram emphasising the basic steps in medicines authentication using NQR.

and echo train (T_{2e}) relaxation time constants [1]. Figure 6.1 shows a simple block diagram of the typical workflow of a medicine's testing. As discussed in Section 1.4, in real applications, a set of different questions needs to be answered in order to assign an examined medicine as a genuine (a "match"), or as a medicine that its origins should be determined by further analysis. The two essential features of a system which is to be used to tackle the crime of counterfeit medicines in the field, are the signals of high SNR and a short overall detection time. In NQR, the SNR needs to be enhanced due to the relatively weak signals, typically with multiple averages of the measurements. However, this leads to prohibitively long detection times [Gregorovič and Apih, 2009c; Gregorovič, 2015]. Several experimental techniques with sophisticated apparatus, have been proposed to increase the SNR, but in practice, simple, conventional and low cost NQR methods are preferred (see Section 1.2). Moreover, the duration of an experiment, and consequently the SNR, are relative measurements, and they depend on the "level

[1] The T_2^* (i.e., signal lineshape) and T_{2e} relaxation time constants of the k^{th} resonance line are equivalently described by the damping constants $\beta_k = D_w/T_2^*$ and $\eta_k = D_w/T_{2e}$, respectively, with D_w denoting the dwell time.

of identification"; i.e., different levels include the detection of a quadrupolar nuclei, the presence of the correct amount of active ingredient (quantitative NQR), identify a specified manufacturer or even a "finer" level such as identify a batch from this manufacturer. As illustrated in Figure 6.1, the needed SNR increases for each level of analysis. For instance, as shown in Chapter 4, one needs to acquire a number of signal averages to obtain a desired estimation accuracy in the signal amplitude estimates, with or without an uncertainty in the sample's temperature (i.e., off-resonance effects); significant in determining the expected amount of API of a medicine (i.e., quantitative NQR). Furthermore, the damping parameters of the signal can be used as unique features of the identity of a medicine [Topa, 2011; Lužnik et al., 2013; Barras et al., 2012a; Kyriakidou et al., 2015]. The research in Chapter 5 proves the ability of NQR in authenticating variability between batches produced by the same manufacturer, with the sinusoidal damping constant β (i.e., equivalent to the lineshape, T_2^*) being the control parameter. Therefore, depending on what needs to be determined, a fingerprint is to be generated according to specific experimental protocols and conditions. Generally, this procedure is identical to a feedback loop, where information on the medicines' characteristics either through experimental results or signal processing outcomes, are used to build a more accurate and reliable fingerprint.

Generally, the overall aim is to explore ways to minimise the time of the test, while retaining or even improving the SNR. Several research studies propose ways and determine conditions to maximise the signal experimentally. For example, Mikhaltsevitch and Rudakov [2004] have determined the condition of $2\tau \geq T_2^*$ (2τ is the RF pulse spacing) for the optimum detection experimentally, when the multiple pulse spin-locking sequence is used. By exploiting the dependence of the T_{2e} parameter on 2τ in sodium nitrite, the authors found that the maximum signal intensity is achieved when $2\tau \geq T_2^*$. It is known that when 2τ decreases, the echo train decays for longer periods (i.e., T_{2e} increases); thus, more echoes need to be acquired to capture the full echo train [Gregorovič and Apih, 2009c]. This dependency has been shown to be different for each material, and needs to be further investigated and well understood (see Section 2.6.2). Moreover, in Gregorovič and Apih [2009c], the authors used a matched filter method to obtain a theoretical expression of the SNR and employed it to optimise parameters of the SLSE pulse sequence. In that study, the aim was to improve detection performance using TNT, by determining the optimal sampling and pulse spacing

times. Herein, the focus is authentication of a material, which requires accurate estimates of the control parameters T_2^* and T_{2e}. In simpler words, if a fingerprint of paracetamol tablets of the brand Panadol is to be authenticated, the goal is the assignment of single values of the characteristic parameters for this specific product. For every form of medicine (capsules, caplets, powders and so on) and for every manufacturer, their fingerprints should contain distinct values obtained under specific experimental protocols; this includes both experimental procedures and signal processing methods (e.g, FT or other advanced detection algorithms).

In comparison with other studies, this chapter presents how the use of the efficient FETAML algorithm can be optimised, through conditions of pulse sequence design. As the strength of the signals returned by the PSL sequence decreases when the spacing between the refocussing RF pulses increases, it is often impractical to work with acquisition times - and also RF pulse spacings - long enough to capture the whole echo. Thus, if the FETAML algorithm is to be exploited, the minimum possible acquisition time for the algorithm to return a good estimate of β_k (or T_2^*), for the k^{th} spectral line, must be determined. Moreover, a NQR echo train can be sustained for long times and a number of echoes should be acquired over those periods in order to obtain an accurate estimate of its decay time. As mentioned, since the echo train persists if the refocusing pulse spacing shortens, more echoes should be acquired to precisely estimate the full decay in the same time; in practice, for a very long T_{2e} (order of several seconds), one should acquire thousands of echoes. Herein, the accuracy of the estimated echo train decay constant is explored when fewer echoes compose the NQR echo train. The data sets in this study were obtained under on-resonance conditions, at a fixed sample temperature. The FETAML (similarly, FODETAML when $\Delta\nu = 0$) detection algorithm was used to estimate the parameters.

6.2 Sinusoidal damping constant and acquisition time

The effect of the level of truncation of the NQR echoes on the estimated spin-phase relaxation parameter T_2^* is examined, when the FETAML algorithm is applied. Therefore, materials with very dissimilar lineshapes are used to examine this effect. Sections 6.2.1 and 6.2.2 illustrate the experimental procedure and the results, respectively.

6.2.1 Experimental Procedure

Two formulations of analgesic paracetamol (acetaminophen) were used. The lineshapes of the NQR signals depend on the mechanical processing and manufacturing conditions, and differ from powders, caplets, tablets and capsules [Lužnik et al., 2013; Topa, 2011; Barras et al., 2012a]. Herein, paracetamol caplets and capsules of the same brand (Panadol) were used; 60 caplets and 60 capsules of 0.5 g each. The medicines were tested at the resonance line $\nu_+ = 2.563$ MHz at 295 K. Both the paracetamol caplets and capsules were put in separate standard medicine bottles and placed in the cylindrical fixed pitch coil. The experimental setup used is described in Chapter 3. Using the temperature control bath system, the temperature was kept monitored at 295 ± 0.5 K throughout the measurements. In order to test the influence of the level of echo truncation, data sets were obtained at four different acquisition times. Note that the refocusing RF pulse spacing was kept constant in order to eliminate any other dependencies of the signal parameters and ensure that the total signal intensity was the same. The measurements were obtained using the PSL sequence. Table 6.1 summarises the timing parameters used for both samples. Echo trains containing 1024 echoes were obtained followed by another *noise only* sequence of 1024 blocks. Note that the dead time and acquisition delay were changed accordingly in order to keep the echo in the middle of the acquisition window, whereas the number of samples per echo was kept constant. A total of 16 data sets per sample were acquired. Figure 6.2 illustrates the NQR lineshapes (in time domain) of paracetamol caplets and capsules, obtained from the spectra of the summed echoes for the longer acquisition time of 1536 μs. For the temperature estimates, the search region was set as $[290, 300]$ K in 500 steps. Furthermore, the selected search regions for the sinusoidal damping and echo damping constants were $\beta = [1 \times 10^{-3}, 0.05]$ in 500

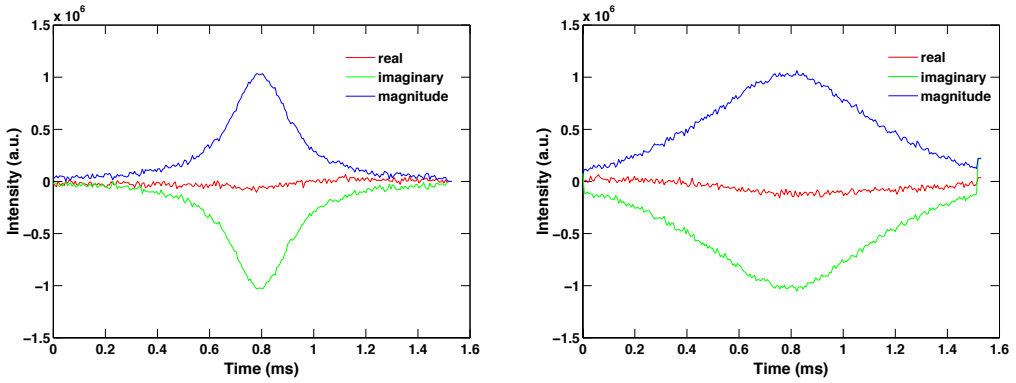

(a) (b)

Figure 6.2: NQR lineshapes of paracetamol (a) caplets (T_2^*=0.164 ms) and (b) capsules (T_2^*=0.510 ms) of the same brand (Panadol); 2τ = 2286 µs and acquisition time = 1536 µs.

Table 6.1: PSL experimental parameters.

excitation frequency (MHz)	2.563
pulse width (µs)	60
τ spacing (µs)	1143
echo spacing (µs)	2286
repeat time (s)	11
number of echoes	1024 × 2
samples per echo	256
scans	8
dwell time (µs)	1, 2, 4, 6
acquisition time (µs)	256, 512, 1024, 1536
dead time (µs)	984, 856, 600, 344
acquisition delay (µs)	986, 858, 602, 346

steps and $\eta = [1 \times 10^{-7}, 1 \times 10^{-5}]$ in 1000 steps, respectively. As illustrated, the lineshapes vary significantly, with $T_2^* = 0.164$ ms ($\beta = 0.036$) and $T_2^* = 0.510$ ms ($\beta = 0.012$) for caplets and capsules, respectively.

6.2.2 Results and Discussion

The FETAML detection algorithm was used to provide estimates of the truncated echo sinusoidal damping constant, β, for each of the 16 measurements. In Figure 6.3, the T_2^* estimated parameters (derived from $T_2^* = D_w/\beta$) are plotted with respect to the acquisition time, for both paracetamol caplets and capsules.

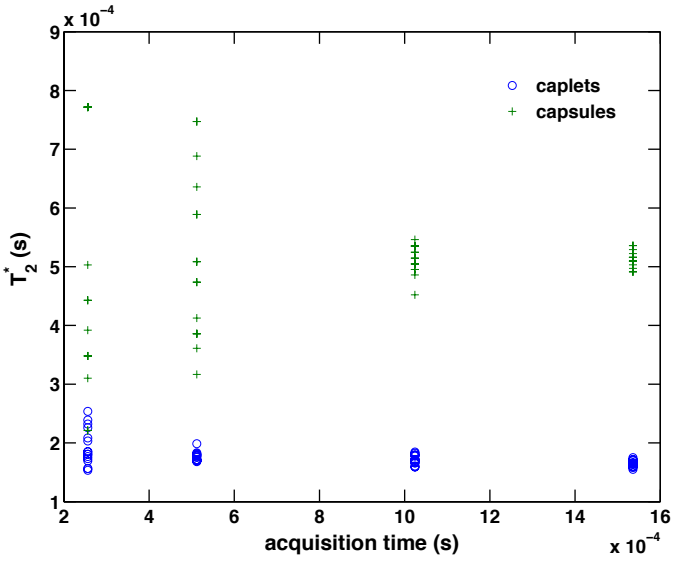

Figure 6.3: T_2^* estimates with respect to the acquisition time, for both paracetamol caplets and capsules.

The echo signal is modelled as a back-to-back damped sinusoidal. When the acquisition window shortens, only some part of the echo is captured. For too short acquisition times, it is expected that the accuracy in the estimates will be limited. This is illustrated in Figure 6.3. There is a significant variation in the estimated parameters at shorter acquisition windows, for both samples. Note that the mean T_2^* is relatively constant for both samples. As expected, the estimated parameters are more dispersed for paracetamol capsules and this is attributed to the longer lineshape of the sample. In order to determine the accuracy in the β estimates, the corresponding coefficient of variations [2] were computed for each acquisition time and illustrated in Figures 6.4 and 6.5, for paracetamol caplets and capsules, respectively. In detection and authentication applications, the estimation accuracy may be determined by setting a desired tolerance level. If this level is set to be 5%, then from the results in Figures 6.4 and 6.5, one should acquire the measurements using an acquisition window twice the size of the lineshape of the examined medicine. Therefore, for this tolerance level, the optimal performance of the algorithm is achieved when the sinusoidal damping constant is estimated under this condition. In practice, it is the refocusing RF pulse spacing that is to be reduced in order to enhance the signal. It should be noted that the accuracy

[2]Coefficient of variation is a statistical measure also known as relative standard deviation (RSD), that describes the dispersion of a probability distribution. This measure is defined as the ratio of the standard deviation to the mean and often expressed as a percentage.

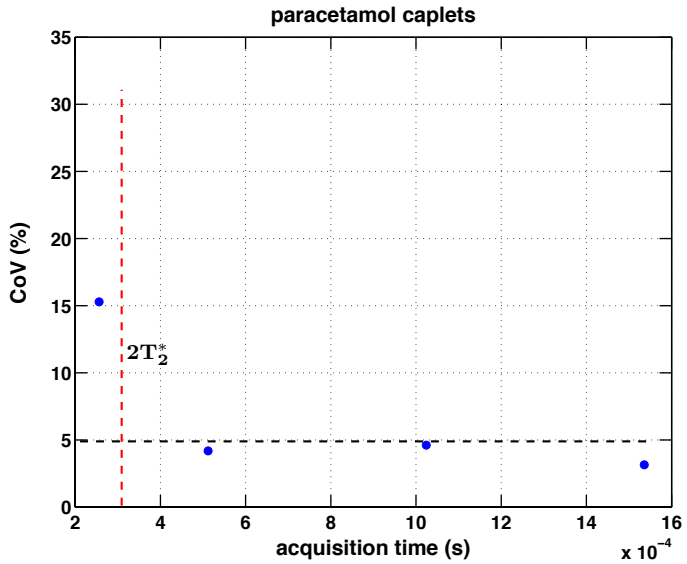

Figure 6.4: Coefficient of variation versus acquisition time for paracetamol caplets, of the sinusoidal damping constant (β) estimates; for caplets, $T_2^* = 0.164$ ms.

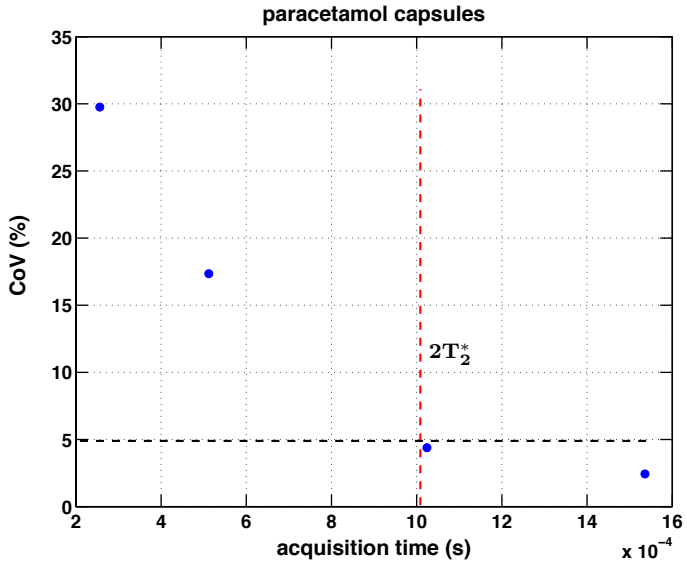

Figure 6.5: Coefficient of variation versus acquisition time for paracetamol capsules, of the sinusoidal damping constant (β) estimates; for capsules, $T_2^* = 0.510$ ms.

in the estimated parameters is greatly influenced by the SNR. Therefore, the condition is violated at lower SNR. However, even when the SNR is high enough, a too short pulse spacing will result in a truncated damped sinusoidal with less sampling information. Consequently, it is important to identify the ability of the applied signal processing method, and then use this information to design the pulse sequence for the algorithm's optimal performance.

6.3 Echo damping constant and number of echoes

Trains of echoes were obtained from several materials in order to investigate how the accuracy in the echo damping constant estimates is influenced when the number of echoes is modified. As in Section 6.2, the measurements were obtained under on-resonance conditions. A data processing method was applied on each original echo train in order to re-create echo trains with fewer and fewer echoes. Herein, that number of echoes that will still enable the FETAML algorithm to accurately estimate the echo damping constants, within a tolerance level, is to be explored. Since the echo train decay varies between different materials, this number may not be the same for every one of them. Section 6.3.1 contains information on the experimental conditions and pulse sequence parameters used to capture the echo trains from different substances, whereas Section 6.3.2 provides a discussion of the outcomes.

6.3.1 Experimental Procedure

^{14}N NQR echo trains were obtained from several materials; the molecular structures of analgesic paracetamol caplets, paracetamol capsules, antibiotic ampicillin (trihydrate) [Barras et al., 2012a,b], antibacterial sufladiazine [Blinc et al., 2006; Latosińska, 2007a] and sodium nitrite are illustrated in Figures 5.1 (for both caplets and capsules), 6.6, 6.7 and 4.2, respectively. The temperature control system was used for stabilisation within 297 ± 0.5 K. The measurements were conducted using the selected resonance lines 2.564 MHz, 3.033 MHz, 2.563 MHz and 3.60 MHz, for paracetamol, ampicillin, sulfadiazine and sodium nitrite, respectively. Both ampicillin and sulfadiazine are on the WHO list of essential medicines [WHO, 2015]. The temperature coefficients for ampicillin and sulfadiazine are 80 Hz/K and -40 Hz/K, respectively, and they can be well modelled using (4.4) [Blinc et al., 2006; Barras et al., 2012a]. Herein, the quantities of the

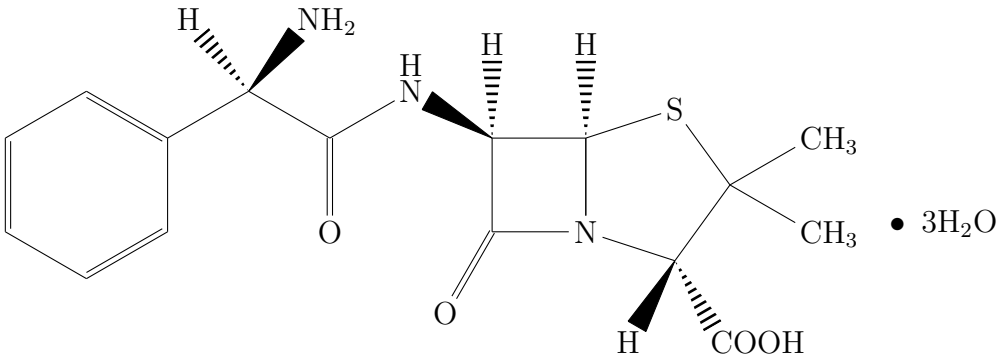

Figure 6.6: The molecular structure of ampicillin (trihydrate).

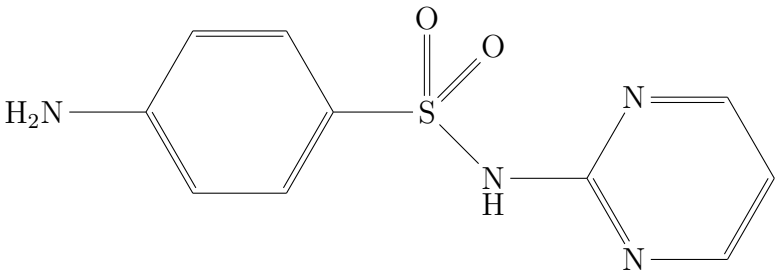

Figure 6.7: The molecular structure of sulfadiazine.

examined materials were as follows: 60×500 mg paracetamol caplets, 60×500 mg paracetamol capsules, 22 g powder ampicillin trihydrate (Sigma Aldrich), 50 g powder sulfadiazine (Sigma Aldrich) and 80 g powder sodium nitrite. The PSL sequence was used to obtain the NQR signals and the timing parameters are summarised in Table 6.2. Chapter 3 provides all the information on the experimental setup used to obtain the data sets. Figure 6.8 illustrates the captured NQR echo trains.

6.3.2 Results and Discussion

The FETAML algorithm was used to analyse the echo trains and provide estimates of the signal parameters. Herein, the primary aim is to explore how the accuracy in the echo damping constant estimates (η) is influenced with the number of echoes within the echo train. In order to examine this research question, a simple approach was implemented. An illustration of the approach is shown in Figure 6.9. When a series of refocusing RF pulses is applied every 2τ periods, a train of echoes is generated within a total time, t. The echo train in Figure 6.9 consists of $M = 8$ echoes. If one merges every two adjacent echoes (i.e., $N = 2$)

Table 6.2: PSL experimental parameters for all the examined materials (T = 297 K).

	paracetamol	ampicillin	sufladiazine	sodium nitrite
excitation frequency (MHz)	2.564	3.033	2.563	3.600
pulse width (µs)	60	50	60	40
τ spacing (µs)	1144	349	1203	621
echo spacing (µs)	2284	698	2406	1242
dwell time (µs)	6	4	6	2
dead time (µs)	344	126	404	344
acquisition delay (µs)	344	10	406	346
repeat time (s)	11	0.001	30	1
acquisition time (µs)	1536	512	1536	512
number of echoes	2048	64	512	256
samples per echo	256	128	256	256
scans	1,600	40,000	2,600	400

in that echo train, the resulting echo train ends up with $M' = M/2$ echoes. Here, the overall period of the decay needs to be retained in order to keep all the other parameters constant (such as the signal intensity); thus, "pseudo" RF pulse spacings are generated to ensure the total decay time is kept the same. The remaining 4 echoes are now separated by $2 \times 2\tau$ periods. Moreover, when every 4 adjacent echoes are merged (i.e., $N = 4$), the echo train will contain 2 echoes separated by $4 \times 2\tau$. In every iteration, the number of merged adjacent echoes doubles; that is, $N = 2, 4, 8, 16, 32, 64, \ldots$. Therefore, the analogous pulse spacing and total number of echoes within the resulting echo train will change accordingly. This approach was applied on several materials with different echo train decays. For each of the materials, the search grid region for the damping constants was selected as: for paracetamol caplets, $\beta = [0.01, 0.1]$ in 1000 steps, and $\eta = [1 \times 10^{-6}, 1 \times 10^{-5}]$ in 4000 steps; for paracetamol capsules, $\beta = [0.01, 0.05]$ in 1000 steps, and $\eta = [1 \times 10^{-6}, 1 \times 10^{-5}]$ in 4000 steps; for ampicillin, $\beta = [1 \times 10^{-5}, 0.03]$ in 2000 steps, and $\eta = [1 \times 10^{-6}, 1 \times 10^{-3}]$ in 4000 steps; for sulfadiazine, $\beta = [0.01, 0.05]$ in 1000 steps, and $\eta = [1 \times 10^{-7}, 5 \times 10^{-5}]$ in 5000 steps; for sodium nitrite, $\beta = [0.001, 0.06]$ in 1000 steps, and $\eta = [1 \times 10^{-6}, 5 \times 10^{-4}]$ in 3000 steps.

Figure 6.10 illustrates the estimated echo damping constants with respect to the number of echoes (M') within the echo train for each of the examined materials. In Figure 6.10(a), the estimated η parameters are shown for paracetamol caplets, when every 1, 2, 4, 8, 16, 32, 64, 128, 256 and 512 adjacent echoes are merged. In other words, the resulting echo trains contain 2048, 1024, 512, 256,

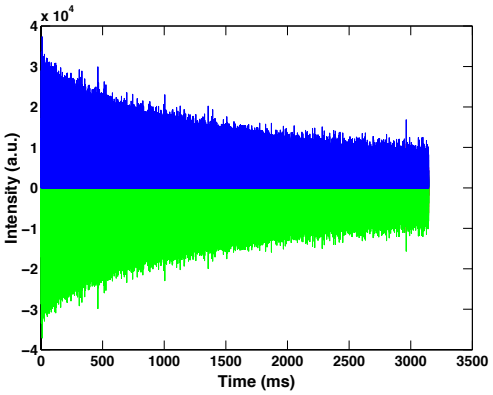

(a) paracetamol caplets

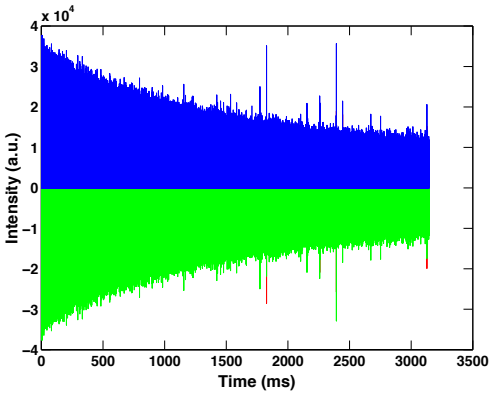

(b) paracetamol capsules

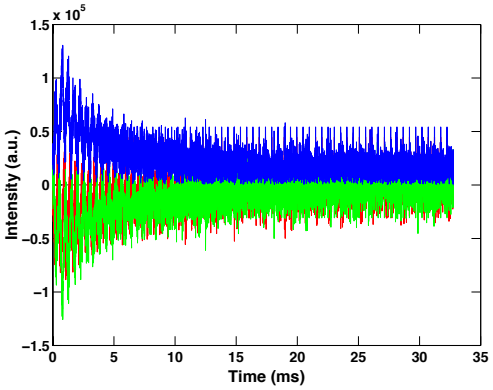

(c) ampicillin (trihydrate)

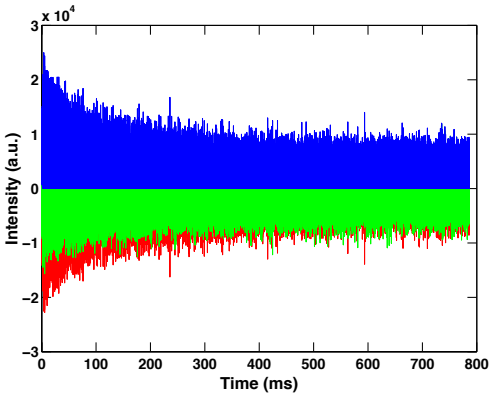

(d) sulfadiazine

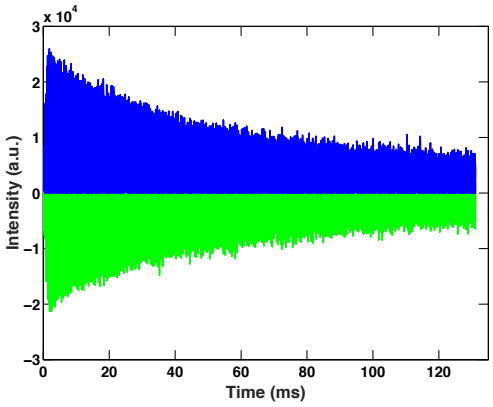

(e) sodium nitrite

Figure 6.8: The time domain echo trains obtained from five different samples.

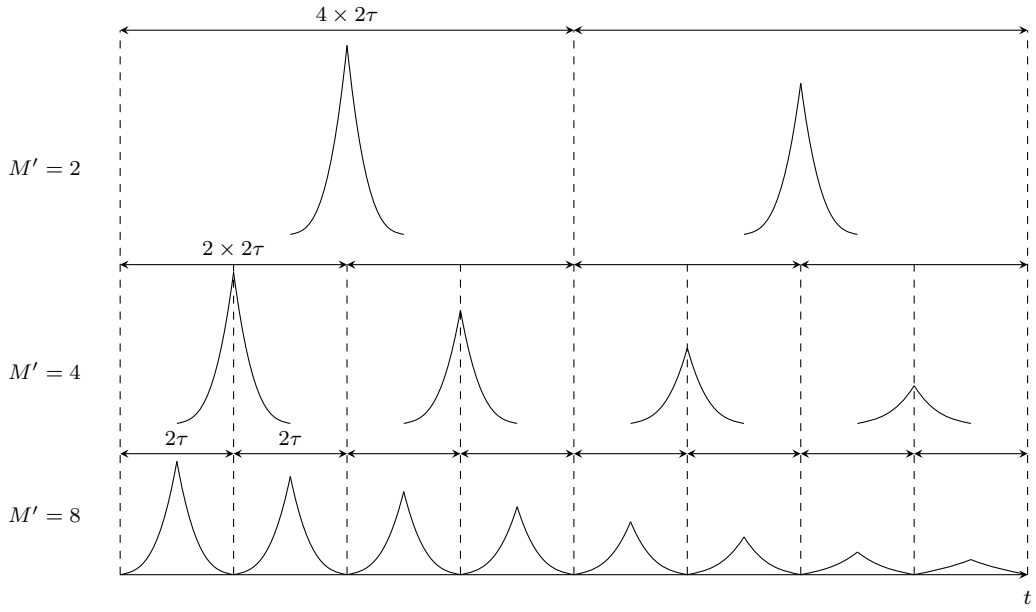

Figure 6.9: Simple illustration of merging the adjacent echoes within an echo train; in every iteration, N doubles are merged with $2\tau' = N \times 2\tau$ and $M' = M/N$ changing correspondingly.

Table 6.3: The echo damping constant estimates for each of the examined material.

	η	M
paracetamol caplets	3.509×10^{-6}	2048
paracetamol capsules	5.425×10^{-6}	2048
ampicillin trihydrate	5.514×10^{-4}	64
sulfadiazine	1.902×10^{-5}	512
sodium nitrite	2.032×10^{-5}	256

128, 64, 32, 16, 8 and 4 echoes, respectively. In order to examine how the estimated η parameters vary, a benchmark value is defined. From the benchmark value, a percentage degree of tolerance within which the resulting estimates are considered accurate is allowed. The reasonable benchmark values are shown in Table 6.3 and they are the η parameters estimated when the echo trains contain the maximum number of echoes (i.e., the echo trains obtained experimentally). In Figure 6.10, the selected tolerance levels of 1% and 2% are illustrated. In the case of paracetamol caplets (see Figure 6.10(a)), the estimated η parameter begins to deviate from the $\pm 1\%$ tolerance level when the echo train contains only 4 echoes. Therefore, the accuracy is retained within this level even when the echo train contains just 8 echoes. With regards to the rest of the materials, the

outcome of this straightforward approach indicates that at the ±1% tolerance level, the accuracy of the estimates is maintained when the echo trains consist of at least 16 echoes.

6.4 Conclusions

NQR suffers from relatively weak signals. The most common approach of signal enhancement is the acquisition of multiple signal averages which sometimes may result in prohibitively long experimental durations. Current ways to overcome this limitation range from hardware improvements to sophisticated designs of pulse sequences. In NQR, any methods that could help increase the SNR is extremely beneficial. While several studies propose ways to maximise the signal intensity experimentally, the aim of this study was to identify limits in terms of data analysis, while focusing on the accuracy of the damping constants. Specifically, this study proposes flexible approaches to optimise the utility of the FETAML algorithm through pulse sequence design. First, the effect of a too short acquisition window on the accuracy of the sinusoidal damping constant was examined in a high SNR scenario. By exploiting two materials - here, paracetamol in two forms (caplets and capsules) - with very different signal lineshapes, the optimal performance of the FETAML algorithm was achieved when the acquisition window is greater or equal to twice the lineshape. The condition was determined by selecting a reasonable tolerance level in the variability of the estimated parameter. This outcome is valid for these particular experimental conditions and when the FETAML algorithm is to be applied. It may be that a general condition does not exist; but if the aim is to use the sinusoidal damping constant as the control parameter in authenticating a medicine, one needs to identify the capabilities of the signal processing technique used for estimating this parameter. Then one can exploit this information to help design the pulse sequence (here, the PSL pulse sequence). Moreover, the duration of the refocusing pulse spacing is always limited by the dead time. However, depending on what are the limitations in terms of data acquisition, one needs to explore the effect on data processing. For example, if there is the requirement of the acquisition time being much shorter than $2T_2^*$, then a secondary characteristic parameter should be exploited. Depending on the question to be answered, a parameter may be chosen over another. In Chapter 5, the results from the analysis of different batches of paracetamol caplets revealed

that the sinusoidal damping constant was the discriminatory parameter. Therefore, one should choose wisely the pulse sequence timings, if the aim is to obtain accurate estimates of this parameter.

Next, the effect of having an echo train with fewer echoes was explored and tested on several materials with different echo decay times. The outcomes of the simple approach carried out, revealed that one doesn't need to capture a large number of echoes in order to obtain an accurate estimate of the echo train decay time. The FETAML algorithm illustrates that the echo damping constant can still be accurately estimated within acceptable tolerance levels when the echo train consists of just a few echoes. The fact that the estimated parameter is persistent within the set tolerance level when the number of echoes decreases, then this might indicate some presence of data redundancy, where the model could have been fitted with a fewer number of data points. Therefore, for a substance with a long echo decay time, it may not be necessary to acquire thousands of echoes for an accurate estimate of the decay.

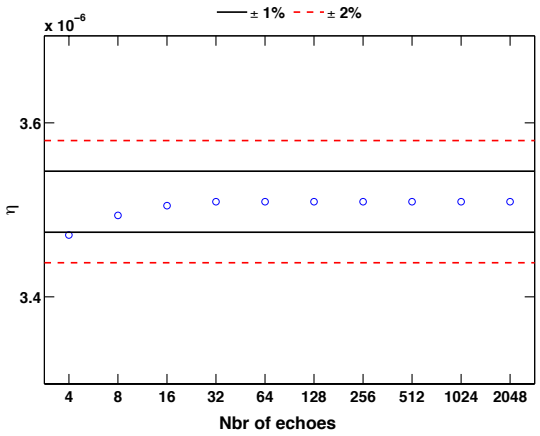

(a) paracetamol caplets

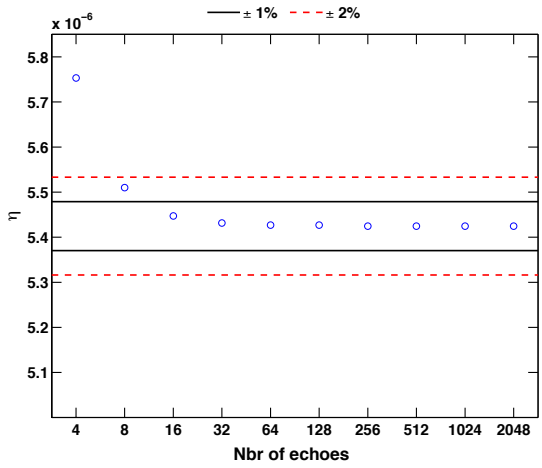

(b) paracetamol capsules

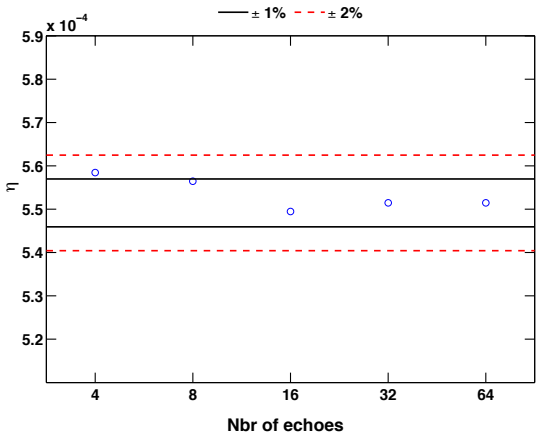

(c) ampicillin (trihydrate)

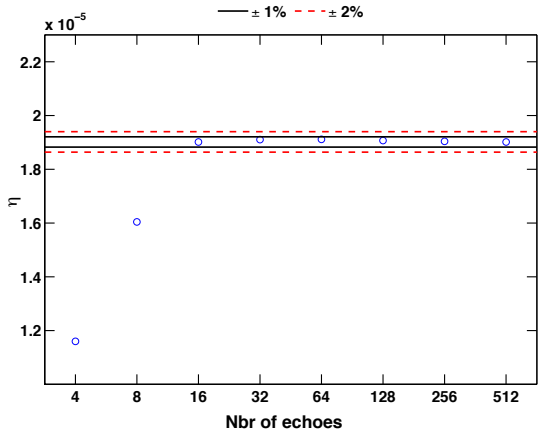

(d) sulfadiazine

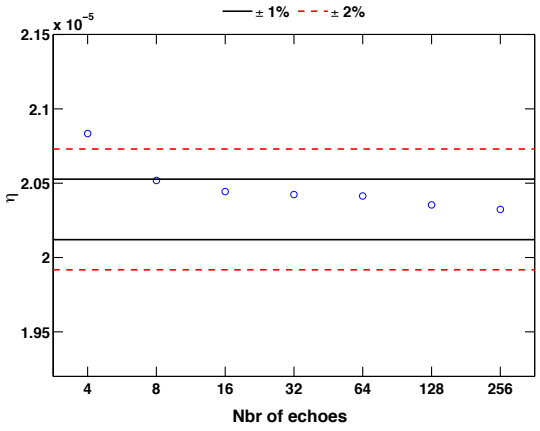

(e) sodium nitrite

Figure 6.10: The echo damping estimates versus the number of echoes (M') within the echo train, with the tolerance levels of $\pm 1\%$ and $\pm 2\%$.

Chapter 7

Conclusions

"And if you find her poor, Ithaka wont have fooled you. Wise as you will have become, so full of experience, you will have understood by then what these Ithakas mean."

Constantinos C. Cavafy, Poet

In response to the global crime of substandard and counterfeit medicines, the necessity of implementing analytical methods in order to tackle this problem is raised. This thesis primarily focused on improving signal processing and pulse sequence systems using NQR. The suitability of NQR spectroscopy for medicine authentication has been made feasible since most of the commercially available medicines are found in solid form. NQR can uniquely identify the presence of the actual active ingredient within the material while its high sensitivity to crystalline fluctuations facilitates the specification of the material's physical and chemical properties. The critical step of building a precise "fingerprint" for a certain medicine is often hampered by several factors that must be addressed carefully:

- The NQR signals are inherently weak, and often, multiple signal accumulations are obtained in order to enhance the signal-to-noise (SNR) ratio.
- Depending on the material under study, the duration of a measurement may be prohibitively long. In particular, the higher the number of signal averages selected, the longer the duration of the test. This limitation of NQR could potentially cause delays in real applications when accurate authentication must be achieved within a few minutes or even seconds.

- Often, when there is an uncertainty in the sample's temperature, the *off-resonance effects* occur, in which the resonance and RF excitation frequency do not coincide. This can result in an unexpected weakening of the signal amplitude and a non precise estimation of the amount of the active ingredient within the material.

- The variability between medicines produced by the same manufacturing conditions can be an important issue, especially in the presence of "high-quality" fake medicines. Several factors, including the temperature, pressure or humidity, may be responsible for the stability and degradation of a medicine.

In this thesis, the objective was to improve upon the aforementioned issues, by proposing an enhanced signal model, introducing versatile signal processing approaches and investigating the responses from several medicines; these led to the following contributions:

Thesis Contributions

- The proposal of an enhanced NQR signal model, which exploits the dependence of the signal amplitude on the off-resonance excitation and sample's temperature. The capability of the model to determine the actual signal amplitude under temperature uncertainties, is expected to improve the overall detection performance.

- The proposal of the improved theoretical bound, Cramér-Rao lower bound (CRLB). Depending on the desired estimation accuracy in the estimated signal amplitude, the CRLB can be used to determine the number of needed signal averages.

- Presentation of the ^{14}N off-resonance profiles of metformin hydrochloride caplets and powder aniracetam; to the best knowledge of the author, this is the first time such a study has been conducted.

- The investigation of batch-to-batch variability of paracetamol tablets, produced by the same manufacturing company. The NQR sinusoidal damping constant is the crucial parameter in revealing variability among the different batches. The results indicate the possible correlation of the medicines

degradation to the ageing factor and shelf life. Essential contribution in quality control and medicines authentication, highlighting the compulsory long term monitoring of a medicine's "fingerprint".

- The introduction of versatile approaches to optimise the utility of the chosen signal processing method, with the proposed solutions achieving a reduction in the measurement times, while ensuring that the accuracy of the estimated parameters remains at the desired levels.

7.1 Summary and Future Work

In practice, the origin of a new medicine is to be tested against a "fingerprint" of its known to be authentic version. The outcome of such a test can be considered precise and reliable only if the same protocols and environmental conditions are used to build the fingerprint. However, there may be occasions where some conditions can be derived only approximately. Temperature fluctuations may alter some of the signal's characteristic parameters and ultimately affect the resulting outcome. Given that the NQR signals can be weak, the presence of an uncertainty in the sample's temperature causes off-resonance effects which can significantly worsen the expected SNR. It is observed that the signal amplitude follows a sinc-like function against the off-resonance frequency, and the amount of signal drop can vary between materials. To tackle this problem, the dependence of the signal amplitude - generated using a pulsed spin-locking (PSL) sequence - on the off-resonance excitation was implemented as an extension to the NQR signal data model. The theoretical amplitude modulation model has been validated on real measurements from three different materials. From those, the off-resonance profiles of antidiabetic metformin hydrochloride and aniracetam were presented. The offset dependent echo train approximate maximum likelihood (ODETAML), and its frequency selective counterpart (ODFETAML), were introduced. This "feature" can be used to extend the plethora of algorithms developed in the literature. Monte Carlo simulation has been used to evaluate the proposed algorithms. By accurately modelling the expected signal amplitudes, the refined model enables the algorithm to account for the off-resonance effects. The derivation of the CRLB of the extended signal data model was introduced. Examples from real measurements have shown that, for given a temperature uncertainty,

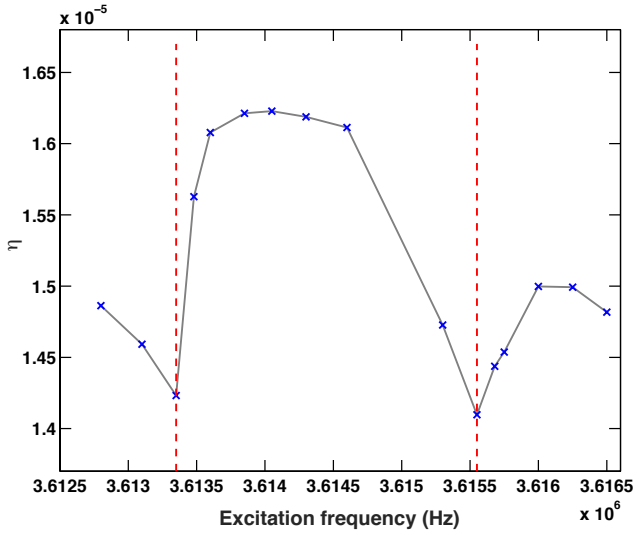

Figure 7.1: The estimated echo damping parameter versus the off-resonance excitation frequency, for the $\nu = 3.615$ MHz spectral line of powder sodium nitrite (283 K); $t_{\mathrm{pw}} = 40$ μs, $2\tau = 418$ μs.

the theoretical bound accurately yields the expected variability of the signal amplitude. Moreover, the CRLB was exploited in order to allow one to determine the required number of signal accumulations for a desired estimation error. The larger the number of signal averages, the higher the estimation accuracy, but the longer the duration of the measurement. It has been reported that the effective relaxation time constant, T_{2e}, exhibits a periodic behaviour with the off-resonance excitation frequency, as observed for paranitrotoluene and trinitrotoluene [Gregorovič et al., 2009]. Initial experiments have been conducted on powder sodium nitrite, in order to test how the echo damping parameter varies with the off-resonance excitation frequency. Figure 7.1 illustrates the results from the early stages of such a study, when a PSL sequence was used; a range of 3.7 kHz was covered. As expected, the echo damping estimates seem to exhibit minimum values, with a periodicity of $t_c^{-1} \approx 2.2$ kHz ($t_c = t_{\mathrm{pw}} + 2\tau$). A result that has been observed from the NQR signals of paranitrotoluene and trinitrotoluene, in the literature [Gregorovič et al., 2009]. Future work should involve the better understanding and implementation of the dependence of the echo damping parameter on the off-resonance effects, as a further extension to the NQR signal data model.

The accuracy of a detection outcome may also be influenced when substantial variability appears among different batches of the examined medicine. This becomes of particular interest when "high-quality" fake drugs are to be examined;

that is, medicines that may contain the correct chemical composition, but vary in terms of excipients and conditions of manufacturing processes. NQR is highly sensitive in dynamical modifications in the crystal, and it is known for discriminating among medicines of various formulations (e.g., capsules, caplets, powder) and medicines produced from different manufacturers. Therefore, in an ideal real case, a database should contain "fingerprints" of unique parameters of the NQR signal, assigned to each individual medicine for each brand and so on. However, a number of factors, including temperature and poor storage conditions can alter the stability of a medicine, which can lead in reduction of its bioavailability. The presented study investigated the presence of variability among batches of one medicine with a long shelf life. The NQR signals generated from batches of analgesic paracetamol tablets (same manufacturing company), with different use-by dates, have been tested. The results revealed no notable variability within packs of the same batch. This outcome indicates the natural variability in generic medicines which are produced under the same manufacturing conditions. However, there was a significant discrimination among the batches with different expiry dates. The parameter which controlled this variability was the sinusoidal damping constant. This outcome strongly confirms that this parameter can be used to describe the physical and chemical properties of the material, including the possibility of acting as a monitoring parameter of the medicine's degradation due to ageing. Therefore, in the fight against the crime of counterfeit medicines, such a study addresses the necessary monitoring of the "fingerprints" within a database. Further work should involve the test of a larger number of batches from a wider range of expiry dates, including medicines from several manufacturers. Moreover, the next step should be the application of a destructive analytical method that could potentially determine the actual source of variability. An example could be the high performance liquid chromatography (HPLC). NQR could potentially be used at all stages of manufacturing and quality assurance of medicines. A future application may be in the concept of "medicines recycling", where the objective is to reduce the waste of unused prescribed medications that leads in significant costs to the national health service (NHS) in UK [BMA, 2011; Pencheon, 2012]. NQR could be a beneficial and easy to use technique, that would analyse unused medicines and according to the quality control standards, one could assign new expiry dates on those (safe to use) products. In the future, optimised models that exploit potential theoretical expressions of the dependence

of the signal characteristic features on each individual factor (e.g., ageing, storage conditions, hydration) would provide innovative improvements in detection performances.

In an optimal scenario, the objective of a real system should be a fast and reliable authentication of the examined medicines. In NQR, the duration of a test can be a relevant number, as it depends on the level of authentication and the SNR; the "finer" the goal, the higher the required SNR and the longer the experimental duration. That is, it may require less time to discriminate among medicines from two different manufacturers, than two batches of the same medicine and same manufacturer. As NQR generally suffers from relatively weak signals, any approach that can be used to enhance the SNR can be extremely beneficial. It is often required to change the timings of a pulse sequence in order to increase the signal intensity. Depending on how one is limited in terms of data acquisition, it is important to determine the effect on data processing. In this thesis, the effect of the level of truncation on the damped sinusoidal signal was examined using two materials of different lineshapes. From the signals of paracetamol caplets and capsules and for a given desired tolerance level, it was determined that the acquisition time should be twice as long as the spin phase relaxation time constant. Note that this condition is specifically derived for that particular set of experimental protocols; a similar identification procedure could be employed for any other set of protocols, for which relevant results could easily be obtained. Another characteristic parameter of the NQR signal is the echo damping constant. In NQR, an echo train can be sustained for long periods, where many echoes should be acquired for an accurate estimation of its decay time. It has been determined that the echo damping constant can still be accurately estimated within acceptable tolerance levels when the echo train consists of just a few echoes. The fact that the estimated parameter is persistent within the set tolerance level and when the number of echoes decreases, then this might indicate some presence of data redundancy, where the model could have been fitted with a fewer number of data points. Again, the echo damping constant is affected by the presence of off-resonance effects, which would create a degree of uncertainty in the estimation. Thus, this dependence should be further explored.

In conclusion, this thesis presents a complete research methodology that addresses issues at all stages of a medicines authentication workflow, using NQR

spectroscopy. The author believes that the proposed novel approaches could potentially provide new insights as to how the problem of counterfeit and low quality medicines could be tackled in the future.

Collaborative Related Work: Publications

Aside to my Ph.D research, I had the opportunity to collaborate and contribute with my colleagues and other members of the NQR society in two studies in regards to medicines authentication using NQR spectroscopy. The first study focuses on the optimisation of hardware such as the design of RF coils to improve quantitative analysis in NQR. The second study reports on the authentication of a suspected fake antimalarial medicine.

Variable-pitch rectangular cross-section radio frequency coils for the nitrogen-14 nuclear quadrupole resonance investigation of sealed medicines packets

NQR spectroscopy can quantitatively analyse the active pharmaceutical ingredient (API) of medicines. In NQR, the RF radiation can pass through materials, such as blister packs, cartoon and plastic without attenuation. This illustrates the non-invasive and non-destructive nature of this technique; no need to remove the blister packs from their packets. In this study, the performance of an optimised variable pitch RF coil which is able to enclose medicine packs of rectangular cross section, have an acceptable filling factor and produce a homogeneous RF field was tested. The objective was the detection of the signal amplitude, independent of the position of the sample within the coil; this is crucial in real scenarios, where the actual medicines are differently mounted on the blister packs. In collaboration with the Graduate School of Engineering Sciences at Osaka University, the performance of three coils of different winding schemes was compared. One fixed

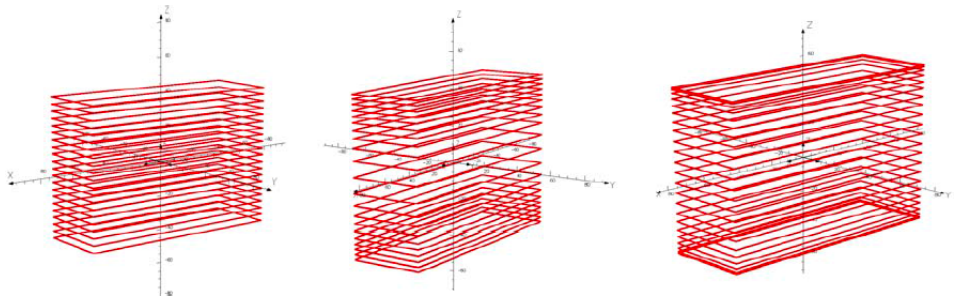

Figure R.1: The rectangular cross section RF coils; left: fixed, middle: variable based on Leifer equations and right: optimised variable pitch coils.

pitch and two variable pitch coils were examined (see Figure R.1). Build on the earlier study of the cylindrical variable pitch coil in Tate et al. [2009], the first variable winding was modified to allow for a rectangular geometry, based on the Leifer equations [Leifer, 1993]. The second variable pitch coil was an optimised version which was designed by empirical modelling, in order to deliver a more homogeneous field distribution. Initially, the performance of the coils was tested using measurements of the effective RF field across different positions within the volume of the coils. An increase in field homogeneity across the optimised RF coil was evident. Next, on-resonance PSL measurements were conducted for different configurations of medicines within the volume of the optimised variable and fixed pitch coils. That is, capsules were either evenly distributed inside the coils, or they were all concentrated in the center, top or bottom of the coils. Herein, ampicillin trihydrate capsules and blister packs of paracetamol tablets were used. As expected, the results revealed less dependence of the NQR signals on the different positioning and distribution of the medicines within the optimised variable pitch solenoid. This is because of the improved homogeneity and sensitivity. An example is shown in Figure R.2 which illustrates the results from the mean signal versus the number of paracetamol pills for two different configurations; loose pills concentrated in the center of the coils and pills spread across the whole volume of the coils. This study has been published in Barras et al. [2012b].

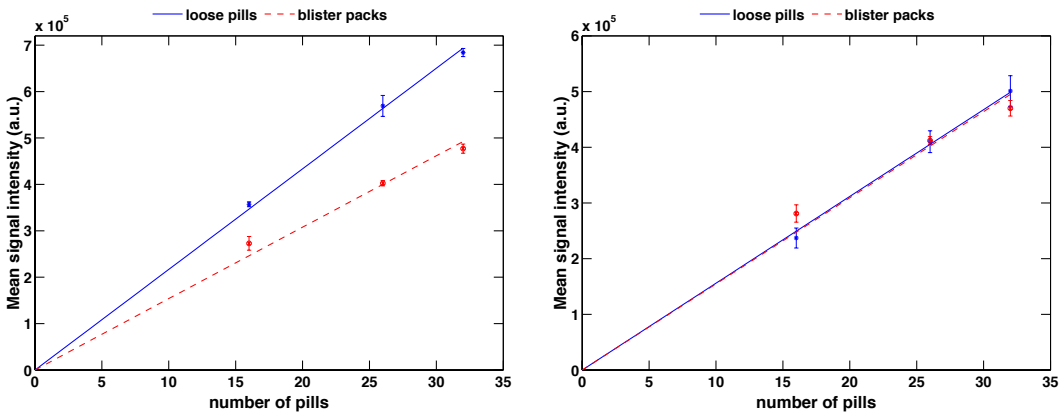

(*a*) (*b*)

Figure R.2: Mean echo signal intensity versus number of analgesic paracetamol pills; (a) fixed and (b) variable pitch coils.

Nitrogen-14 nuclear quadrupole resonance spectroscopy: a promising analytical methodology for medicines authentication and counterfeit antimalarial analysis

Globally, antimalarials are a class of medicines which are commonly targeted by counterfeiters [Dondorp et al., 2004; Nayyar et al., 2012a]. In this study, a suspected counterfeit batch of the antimalarial medicine metakelfin was compared with a known-to-be genuine batch, both produced from the same named manufacturer. The active ingredients contained within a tablet of Metakelfin are sulfalene and pyrimethamine. Quantitative ^{14}N NQR analysis was used to examine the sulfalene content, because of its higher abundance as compared with pyrimethamine. The NQR signals obtained using a PSL sequence, revealed significant spectral differences. Figure R.3 illustrates the NQR spectra obtained from both the genuine and suspected batches. The results of the NQR quantitative analysis proved that the suspected counterfeit medicine contained only $43 \pm 3\%$ of active ingredient (sulfalene), compared to the genuine tablets. The conventional non-destructive tools, FT-NIR and FT-Raman analysis, commonly used in the area of counterfeit crimes, only achieved differentiation between batches but no ascription. The outcome of the NQR analysis was confirmed with destructive HPLC, with a sulfalene content of $42 \pm 2\%$. The slight differences in their linewidths could possibly indicate differences in the way they have been processed. The named manufacturer, Pfizer (Italy), was contacted after the detection and analysis of

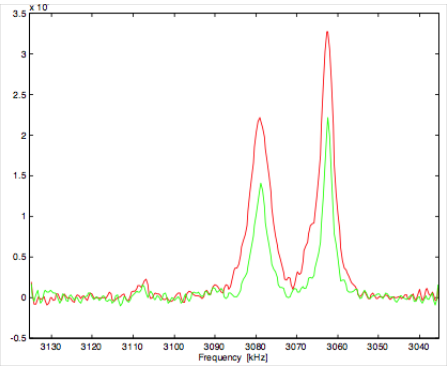

Figure R.3: ^{14}N NQR spectra of genuine (red/higher peaks) and suspect counterfeit (green/lower peaks) of antimalarial medicine Metakelfin.

the two batches, which was able to confirm that the suspected tablets actually came from a batch known to be counterfeit. The high sensitivity and characteristic quadrupolar parameters of NQR spectroscopy enables the authentication of medicines between samples made by the same manufacturer. Without the need of any complex chemometric approaches, NQR was able to provide rapid and non-invasive authentication of Metakelfin tablets. This study has been published in Barras et al. [2013].

Bibliography

Adalbjörnsson, S. I. and Jakobsson, A. (2010). Relax-based estimation of voigt lineshapes. In *18th European Signal Processing Conference, EUSIPCO*, pages 1053–1057.

Aissani, S., Guendouz, L., and Canet, D. (2014). Cmos based q-switch for low-power pulsed14N quadruple resonance. *Concepts in Magnetic Resonance Part B: Magnetic Resonance Engineering*, 44(1):12–17.

Anderson, T. W. (2003). *An Introduction to Multivariate Statistical Analysis*. Wiley-Blackwell: Hoboken, NJ, 3 edition.

Anderson, T. W. and Darling, D. A. (1954). A test of goodness of fit. *Journal of American Statistical Association*, 49(268):765–769.

Andrew, E. R. and Jurga, K. (1987). NMR probe with short recovery time. *Journal of Magnetic Resonance*, 73(2):268–276.

Augustine, M. P., TonThat, D. M., and Clarke, J. (1998). SQUID detected NMR and NQR. *Solid State Nuclear Magnetic Resonance*, 11(1):139–156.

Balchin, E., Malcolme-Lawes, D. J., Poplett, I. J. F., Rowe, M. D., Smith, J. A. S., Pearce, G. E. S., and Wren, S. A. C. (2005). Potential of nuclear quadrupole resonance in pharmaceutical analysis. *Analytical Chemistry*, 77(13):3925–3930.

Balchin, E., Malcolme-Lawes, D. J., Rowe, M. D., Smith, J. A. S., Bearpark, M. J., Steed, J. W., Wu, W., Horsewill, A. J., and Stephenson, D. (2004). The unusual solid state structure of heroin hydrochloride monohydrate and its selective detection using NQR spectroscopy. *New Journal of Chemistry*, 28(11):1309–1314.

Barras, J., Althoefer, K., Rowe, M. D., Poplett, I. J., and Smith, J. A. S. (2012a). The emerging field of medicines authentication by nuclear quadrupole resonance spectroscopy. *Applied Magnetic Resonance*, 43(4):511–529.

Barras, J., Gaskell, M. J., Hunt, N., Jenkinson, R. I., Mann, K. R., Pedder, D. A. G., Shilstone, G. N., and Smith, J. A. S. (2004). Detection of ammonium nitrate inside vehicles by nuclear quadrupole resonance. *Applied Magnetic Resonance*, 25(3-4):411–437.

Barras, J., Katsura, S., Sato-Akaba, H., Itozaki, H., Kyriakidou, G., Rowe, M. D., Althoefer, K. A., and Smith, J. A. S. (2012b). Variable-pitch rectangular cross-section radiofrequency coils for the nitrogen-14 nuclear quadrupole resonance investigation of sealed medicines packets. *Analytical Chemistry*, 84(21):8970–8972.

Barras, J., Murnane, D., Althoefer, K., Assi, S., Rowe, M. D., Poplett, I. J. F., Kyriakidou, G., and Smith, J. A. S. (2013). Nitrogen-14 nuclear quadrupole resonance spectroscopy: A promising analytical methodology for medicines authentication and counterfeit antimalarial analysis. *Analytical Chemistry*, 85(5):2746–2753.

Bayer, H. (1951). Zur theorie der spin-gitterrelaxation in molekülkristallen. *Zeitschrift für Physik*, 130(2):227–238.

Beguš, S., Jazbinšek, V., Pirnat, J., and Trontelj, Z. (2014). A miniaturized NQR spectrometer for a multi-channel NQR-based detection device. *Journal of Magnetic Resonance*, 247:22–30.

Blauch, A. J., Schiano, J. L., and Ginsberg, M. D. (1999). Optimization of offset frequency in the SORC pulse sequence using feedback. *Journal of Magnetic Resonance*, 139(1):139–151.

Blinc, R., Seliger, J., Zidans, A., Žagar, V., Milia, F., Robert, H., et al. (2006). 14N nuclear quadrupole resonance of some sulfa drugs. *Solid State Nuclear Magnetic Resonance*, 30(2):61–68.

BMA (2011). Dispensed but unopened medications. `http://bma.org.uk/about-the-bma/how-we-work/professional-activities-and-special-interest/`

`patient-liaison-group/dispensed-but-unopened-medications`. (accessed May 19, 2015).

Box, G. E. (1949). A general distribution theory for a class of likelihood criteria. *Biometrika*, pages 317–346.

Bray, J. H. and Maxwell, S. E. (1985). *Multivariate Analysis of Variance*. Number 54. Sage Publications: Newbury Park, CA.

Buess, M. L. and Caulder, S. M. (2004). Factors affecting the NQR line width in nitramine explosives. *Applied Magnetic Resonance*, 25(3-4):383–393.

Buess, M. L., Garroway, A. N., and Yesinowski, J. P. (1994). Removing the effects of acoustic ringing and reducing temperature effects in the detection of explosives by NQR. US Patent 5,365,171.

Burstein, D. (1996). Stimulated echoes: Description, applications, practical hints. *Concepts in Magnetic Resonance*, 8(4):269–278.

Butt, N. R., Gudmundson, E., and Jakobsson, A. (2014). An overview of NQR signal detection algorithms. In Apih, T., Rameev, B., Mozzhukhin, G., and Barras, J., editors, *In Magnetic Resonance Detection of Explosives and Illicit Materials*, NATO Science for Peace and Security Series B: Physics and Biophysics, pages 19–33. Springer: Dordrecht, The Netherlands.

Butt, N. R. and Jakobsson, A. (2011). Efficient removal of noise and interference in multichannel quadrupole resonance. In *Signals, Systems and Computers (ASILOMAR)*, pages 1072–1076. IEEE.

Butt, N. R., Jakobsson, A., Somasundaram, S. D., and Smith, J. A. S. (2008a). Robust multichannel detection of mixtures using nuclear quadrupole resonance. *IEEE Trans. Signal Processing*, 56(10):5042–5050.

Butt, N. R., Somasundaram, S. D., Jakobsson, A., and Smith, J. A. S. (2008b). Frequency-selective robust detection and estimation of polymorphic QR signals. *Signal Processing*, 88(4):834–843.

Canet, D., Merlat, L., Cordier, B., Grandclaude, D., Retournard, A., and Ferrari, M. (2006). 14N pulsed nuclear quadrupole resonance. 2. effect of a single radio-frequency pulse in the general case. *Molecular Physics*, 104(09):1391–1399.

Cantor, R. S. and Waugh, J. S. (1980). Pulsed spin locking in pure nuclear quadrupole resonance. *Journal of Chemical Physics*, 73(3):1054–1063.

Cardona, L., Miyato, Y., Itozaki, H., Jiménez, J., Vanegas, N., and Sato-Akaba, H. (2015). Remote detection of ammonium nitrate by nuclear quadrupole resonance using a portable system. *Applied Magnetic Resonance*, 46(3):295–307.

Carr, H. Y. and Purcell, E. M. (1954). Effects of diffusion on free precession in nuclear magnetic resonance experiments. *Physical Review*, 94(3):630.

Chihara, H. and Nakamura, N. (1980). Advances in nuclear quadrupole resonance. *Heyden, London*, 4:1.

Chihara, H., Nakamura, N., and Ōkuma, H. (1968). Temperature dependence of nuclear quadrupole resonance frequencies of 121Sb, 123Sb and 35Cl in solid antimony trichloride. *Journal of the Physical Society of Japan*, 24(2):306–313.

Choi, K. and Yu, I. (1989). Inductive detection of piezoelectric resonance by using a pulse NMR/NQR spectrometer. *Review of Scientific Instruments*, 60(10):3249–3252.

Cockburn, R., Newton, P. N., Agyarko, E. K., Akunyili, D., and White, N. J. (2005). The global threat of counterfeit drugs: why industry and governments must communicate the dangers. *PLOS Medicine*, 2(4):302.

Conphirmer (2011). Conphirmer. `http://www.conphirmer.com/index.html`. (accessed August 29, 2015).

Cordier, B., Grandclaude, D., Retournard, A., Merlat, L., and Canet*, D. (2005). 14N pulsed nuclear quadrupole resonance. 1. nutation experiments in the case of an axially symmetric electric field gradient tensor. *Molecular Physics*, 103(19):2593–2598.

Cowan, B. (2005). *Nuclear magnetic resonance and relaxation*. Cambridge University Press.

Croker, D. M., Hennigan, M. C., Maher, A., Hu, Y., Ryder, A. G., and Hodnett, B. K. (2012). A comparative study of the use of powder X-ray diffraction, Raman and Near Infrared spectroscopy for quantification of binary polymorphic mixtures of piracetam. *Journal of Pharmaceutical and Biomedical Analysis*, 63:80–86.

Culzoni, M. J., Dwivedi, P., Green, M. D., Newton, P. N., and Fernández, F. M. (2014). Ambient mass spectrometry technologies for the detection of falsified drugs. *Med. Chem. Comm.*, 5(1):9–19.

Darbeau, R. W. (2006). Nuclear magnetic resonance (NMR) spectroscopy: a review and a look at its use as a probative tool in deamination chemistry. *Applied Spectroscopy Reviews*, 41(4):401–425.

Das, T. P. and Hahn, E. L. (1958). *Nuclear quadrupole resonance spectroscopy*. Number 1. Academic Pr.

Davidson, M. B. and Peters, A. L. (1997). An overview of metformin in the treatment of type 2 diabetes mellitus. *American Journal of Medicine*, 102(1):99–110.

De Peinder, P., Vredenbregt, M., Visser, T., and De Kaste, D. (2008). Detection of lipitor counterfeits: A comparison of NIR and Raman spectroscopy in combination with chemometrics. *Journal of Pharmaceutical and Biomedical Analysis.*, 47(4):688–694.

Deconinck, E., Sacré, P.-Y., Courselle, P., and De Beer, J. O. (2013). Chromatography in the detection and characterization of illegal pharmaceutical preparations. *Journal of Chromatographic Science*, 51(8):791–806.

Dégardin, K., Roggo, Y., Been, F., and Margot, P. (2011). Detection and chemical profiling of medicine counterfeits by Raman spectroscopy and chemometrics. *Anal. Chim. Acta*, 705(1):334–341.

Deisingh, A. K. (2005). Pharmaceutical counterfeiting. *Analyst*, 130(3):271–279.

Dolinšek, J., Milia, F., Papavassiliou, G., Papantopoulos, G., and Karayianni, M. (1994). Two dimensional NQR separation of inhomogeneous and homogeneous lineshapes in disordered solids. *Applied Magnetic Resonance*, 6(4):499–510.

Dondorp, A. M., Newton, P. N., Mayxay, M., Van Damme, W., Smithuis, F. M., Yeung, S., Petit, A., Lynam, A., Johnson, A., Hien, T. T., McGready, R., Farrar, J., Looareesuwan, S., Day, N. P. J., Green, M. D., and White, N. J. (2004). Fake antimalarials in southeast Asia are a major impediment to malaria control: multinational cross-sectional survey on the prevalence of fake antimalarials. *Tropical Medicine & International Health*, 9(12):1241–1246.

El-Khateeb, S. Z., Assaad, H. N., El-Bardicy, M. G., and Ahmad, A. S. (1988). Determination of metformin hydrochloride in tablets by nuclear magnetic resonance spectrometry. *Analytica Chimica Acta*, 208:321–324.

Eliasson, C. and Matousek, P. (2007). Noninvasive authentication of pharmaceutical products through packaging using spatially offset Raman spectroscopy. *Analytical Chemistry*, 79(4):1696–1701.

Fernandez, F. M., Green, M. D., and Newton, P. N. (2008). Prevalence and detection of counterfeit pharmaceuticals: a mini review. *Ind. & Eng. Chem. Res.*, 47(3):585–590.

Ferrari, M. and Canet, D. (2009). 14N pulsed nuclear quadrupole resonance. 4. two-pulse sequences for the determination of T1 and T2 relaxation times. *Molecular Physics*, 107(22):2419–2430.

Freeman, R. (1998). *Spin Choreography*. Oxford University Press Oxford, UK.

Gadape, H. H. and Parikh, K. S. (2011). Quantitative determination and validation of metformin hydrochloride in pharmaceutical using quantitative nuclear magnetic resonance spectroscopy. *Journal of Chemistry*, 8(2):767–781.

Gallagher, J. (2015). `http://www.bbc.co.uk/news/health-33183330`. (accessed September 26, 2015).

Games, P. A. and Howell, J. F. (1976). Pairwise multiple comparison procedures with unequal ns and/or variances: a Monte Carlo study. *Journal of Educational and Behavioral Statistics*, 1(2):113–125.

Garroway, A. N., Buess, M. L., Yesinowski, J. P., and Miller, J. B. (1994a). Narcotics and explosives detection by 14N pure nuclear quadrupole resonance. In *Substance Identification Technologies*, pages 318–327.

Garroway, A. N., Buess, M. L., Yesinowski, J. P., Miller, J. B., and Krauss, R. A. (1994b). Explosives detection by nuclear quadrupole resonance (NQR). In *SPIE's 1994 International Symposium on Optics, Imaging, and Instrumentation*, pages 139–149.

GlaxoSmithKline Consumer Healthcare (2012). Panadol advance 500 mg tablets. `http://www.medicines.org.uk/emcmobile/medicine/21622/spc#SHELF_LIFE`. (accessed July 6,2014).

Gostin, L. O., Buckley, G. J., et al. (2013). *Countering the problem of falsified and substandard drugs*. National Academies Press.

Grechishkin, V. S. and Sinyavskii, N. Y. (1997). New technologies: nuclear quadrupole resonance as an explosive and narcotic detection technique. *Physics-Uspekhi*, 40(4):393–406.

Gregorovič, A. (2015). Quantitative analysis of hydration using nitrogen-14 nuclear quadrupole resonance. *Analytical Chemistry*, 87(13):6912–6918.

Gregorovič, A. and Apih, T. (2008). Relaxation during spin-lock spin-echo pulse sequence in N14 nuclear quadrupole resonance. *Journal of Chemical Physics*, 129(21):214504.

Gregorovič, A. and Apih, T. (2009a). Aplicability of TNT "super-Q detection" to multipulse sequences. *Journal of Magnetic Resonance*, 201(2):131–136.

Gregorovič, A. and Apih, T. (2009b). Improving 14N nuclear quadrupole resonance detection of trinitrotoluene using off-resonance effects. *Solid State Nuclear Magnetic Resonance*, 36(2):96–98.

Gregorovič, A. and Apih, T. (2009c). Tnt detection with 14N NQR: Multipulse sequences and matched filter. *Journal of Magnetic Resonance*, 198(2):215–221.

Gregorovič, A., Apih, T., Lužnik, J., Pirnat, J., and Trontelj, Z. (2009). 14N nuclear quadrupole resonance signals in paranitrotoluene and trinitrotoluene. Spin-lock spin-echo off-resonance effects. In *Explosives Detection Using Magnetic and Nuclear Resonance Techniques*, pages 171–191. Springer.

Gudmundson, E., Stoica, P., Li, J., Jakobsson, A., Rowe, M. D., Smith, J. A. S., and Ling, J. (2010). Spectral estimation of irregularly sampled exponentially decaying signals with applications to RF spectroscopy. *Journal of Magnetic Resonance*, 203(1):167–176.

Gudmundson, E., Wirfalt, P., Jakobsson, A., and Jansson, M. (2012). An ESPRIT-based parameter estimator for spectroscopic data. In *IEEE Statistical Signal Processing Workshop (SSP)*, pages 77–80. IEEE.

Guendouz, L., Robert, A., Retournard, A., Leclerc, S., Aissani, S., and Canet, D. (2012). Off-resonance effects and selectivity profiles in pulsed nitrogen-14

nuclear quadrupole resonance. *Solid State Nuclear Magnetic Resonance*, 47:39–46.

Haas, T. E. and Marram, E. P. (1965). Temperature dependence of chlorine NQR frequencies and pi bonding. *Journal of Chemical Physics*, 43(11):3985–3989.

Hahn, E. L. (1950). Spin echoes. *Physical review*, 80(4):580.

Hajjou, M., Krech, L., Lane-Barlow, C., Roth, L., Pribluda, V. S., Phanouvong, S., El-Hadri, L., Evans, L., Raymond, C., Yuan, E., et al. (2015). Monitoring the quality of medicines: Results from Africa, Asia, and South America. *American Journal of Tropical Medicine and Hygiene*, pages 14–0535.

Hammond, G. S. (1955). A correlation of reaction rates. *Journal of the American Chemical Society*, 77(2):334–338.

Henze, N. and Zirkler, B. (1990). A class of invariant consistent tests for multivariate normality. *Communications in Statistics-Theory and Methods*, 19(10):3595–3617.

Holzgrabe, U. and Malet-Martino, M. (2011). Analytical challenges in drug counterfeiting and falsificationthe NMR approach. *Journal of Pharmaceutical and Biomedical Analysis*, 55(4):679–687.

Ikeda, R., Mikami, M., Nakamura, D., and Kubo, M. (1969). Nuclear quadrupole resonance of nitrogen in sodium nitrite. *Journal of Magnetic Resonance*, 1(2):211–220.

Itozaki, H. (2013). Equipment for inspecting explosives and/or illicit drugs, antenna coil and method for inspecting explosives and/or illicit drugs. US Patent 8,525,515.

Jakobsson, A. and Mossberg, M. (2007). Using spatial diversity to detect narcotics and explosives using NQR signals. *IEEE Trans. Signal Processing*, 55(9):4721–4726.

Jakobsson, A., Mossberg, M., Rowe, M. D., and Smith, J. A. S. (2005a). Frequency-selective detection of nuclear quadrupole resonance signals. *IEEE Trans. Geoscience and Remote Sensing*, 43(11):2659–2665.

Jakobsson, A., Mossberg, M., Rowe, M. D., and Smith, J. A. S. (2005b). Frequency-selective detection of nuclear quadrupole resonance signals. *IEEE Trans. Geoscience and Remote Sensing*, 43(11):2659–2665.

Jakobsson, A., Mossberg, M., Rowe, M. D., and Smith, J. A. S. (2005c). Frequency-selective detection of nuclear quadrupole resonance signals. *IEEE Trans. Geoscience and Remote Sensing*, 43(11):2659–2665.

Jakobsson, A., Mossberg, M., Rowe, M. D., and Smith, J. A. S. (2006). Exploiting temperature dependency in the detection of NQR signals. *IEEE Trans. Signal Processing*, 54(5):1610–1616.

Johnson, R. A., Wichern, D. W., et al. (1992). *Applied multivariate statistical analysis*, volume 4. Prentice Hall Englewood Cliffs, NJ.

Kay, S. (1993). Fundamentals of statistical processing, vol. i: Estimation theory. *America: Prentice Hall PTR*.

Kay, S. M. (1998). Fundamentals of statistical signal processing, Vol. II: Detection Theory. *Signal Processing. Upper Saddle River, NJ: Prentice Hall*.

Kim, S. S., Jayakody, J. R. P., and Marino, R. A. (1992). Experimental investigations of the strong off-resonant comb (SORC) pulse sequence in 14N NQR. *Zeitschrift für Naturforschung A*, 47(1-2):415–420.

Kim, Y. J., Karaulanov, T., Matlashov, A. N., Newman, S., Urbaitis, A., Volegov, P., Yoder, J., and Espy, M. A. (2014). Polarization enhancement technique for nuclear quadrupole resonance detection. *Solid State Nuclear Magnetic Resonance*, 61:35–38.

Kirpichnikov, D., McFarlane, S. I., and Sowers, J. R. (2002). Metformin: an update. *Annals of Internal Medicine*, 137(1):25–33.

Konnai, A., Odano, N., and Asaji, T. (2008). Study of 14N NQR response to SORC pulse sequence. *Hyperfine Interactions*, 181(1-3):93–98.

Kovacs, S., Hawes, S. E., Maley, S. N., Mosites, E., Wong, L., and Stergachis, A. (2014). Technologies for detecting falsified and substandard drugs in low and middle-income countries. *PloS one*, 9(3):e90601.

Kronvall, T., Sward, J., and Jakobsson, A. (2013). Non-parametric data-dependent estimation of spectroscopic echo-train signals. In *IEEE International Conference on Acoustics, Speech and Signal Processing (ICASSP)*, pages 6259–6263. IEEE.

Kushida, T., Benedek, G. B., and Bloembergen, N. (1956). Dependence of the pure quadrupole resonance frequency on pressure and temperature. *Physical Review*, 104(5):1364.

Kyriakidou, G., Jakobsson, A., Althoefer, K., and Barras, J. (2015). Batch-specific discrimination using nuclear quadrupole resonance spectroscopy. *Analytical Chemistry*, 87(7):3806–3811.

Kyriakidou, G., Jakobsson, A., Gudmundson, E., Gregorovic, A., Barras, J., and Althoefer, K. (2014). Improved modeling and bounds for NQR spectroscopy signals. In *In Proceedings of the 22nd European Signal Processing Conference (EUSIPCO 2014)*, pages 2325–2329. Institute of Electrical and Electronics Engineers: Piscataway, NJ.

Latosińska, J. N. (2007a). Applications of nuclear quadrupole resonance spectroscopy in drug development. *Expert Opinion on Drug Discovery*, 2(2):225–248.

Latosińska, J. N. (2007b). Applications of nuclear quadrupole resonance spectroscopy in drug development.

Latosińska, J. N. and Latosińska, M. (2011). Towards understanding drugs on the molecular level to design drugs of desired profiles. In Kapetanović, I., editor, *Drug Discovery and Development–Present and Future*, pages 231–274. Intech: Rijeka, Croatia.

Lee, C. R. and Benfield, P. (1994). Aniracetam. *Drugs & aging*, 4(3):257–273.

Lee, S., Sauer, K. L., Seltzer, S. J., Alem, O., and Romalis, M. V. (2006). Subfemtotesla radio-frequency atomic magnetometer for detection of nuclear quadrupole resonance. *Applied Physics Letters*, 89(21):214106–216100.

Lee, Y. K. (2002). Spin-1 nuclear quadrupole resonance theory with comparisons to nuclear magnetic resonance. *Concepts in Magnetic Resonance*, 14(3):155–171.

Leifer, M. C. (1993). Rf solenoid with extended equiripple field profile. *Journal of Magnetic Resonance, Series A*, 105(1):1–6.

Levene, H. (1960). Robust tests for equality of variances. *Contributions to probability and statistics: Essays in honor of Harold Hotelling*, 2:278–292.

Lilliefors, H. W. (1967). On the Kolmogorov-Smirnov test for normality with mean and variance unknown. *Journal of American Statistical Association*, 62(318):399–402.

Limandri, S., Visnovezky, C., Perez, S. C., Schurrer, C. A., Wolfenson, A. E., Ferro, M., Cuffini, S. L., Goncalves de Souza, J., Aguiar, F. A., and Masetto de Gaitani, C. (2011). Nuclear quadrupole resonance: a technique to control hydration processes in the pharmaceutical industry. *Analytical Chemistry*, 83(5):1773–1776.

Lowe, I. J. and Norberg, R. E. (1957). Free-induction decays in solids. *Physical Review*, 107(1):46.

Lužnik, J., Pirnat, J., Jazbinšek, V., Lavrič, Z., Srčič, S., and Trontelj, Z. (2013). The influence of pressure in paracetamol tablet compaction on 14N nuclear quadrupole resonance signal. *Applied Magnetic Resonance*, 44(6):735–743.

Luźnik, J., Pirnat, J., Jazbinšek, V., Lavrič, Z., Veselco, Žagar, S. S., Seliger, J., and Trontelj, Z. (2014). 14N nuclear quadrupole resonance study of polymorphism in famotidine. *Journal of Pharmaceutical Sciences*, 103(9):2704–2709.

Mackey, T. K., Liang, B. A., York, P., and Kubic, T. (2015). Counterfeit drug penetration into global legitimate medicine supply chains: A global assessment. *American Journal of Tropical Medicine and Hygiene*, pages 14–0389.

Malcolm-Lawes, D. J., Mallion, S., Rowe, M., and Smith, J. A. S. (1999). Time-domain data analysis of NQR response. *Patent application number*, 9915842.

Malone, M. and Sauer, K. (2012). Homonuclear dipolar coupling and cpmg spin-echoes in NQR. *Applied Magnetic Resonance*, 43(4):541–546.

Malone, M. M. (2013). *Pulsed spin locking in spin-1 NQR: Broadening mechanisms*. PhD thesis, George Mason University.

Malone, M. W., McGillvray, M., and Sauer, K. L. (2011). Revealing dipolar coupling with NQR off-resonant pulsed spin locking. *Physical Review B*, 84(21):214430.

Malone, M. W. and Sauer, K. L. (2014a). Heteronuclear dipolar coupling in spin-1 NQR pulsed spin locking. *Journal of Magnetic Resonance*, 238:8–15.

Malone, M. W. and Sauer, K. L. (2014b). Investigating homonuclear broadening in NQR with Carr-Purcell Meiboom-Gill performed on p-chloroaniline. In *Magnetic Resonance Detection of Explosives and Illicit Materials*, pages 61–67. Springer.

Mardia, K. V. (1974). Applications of some measures of multivariate skewness and kurtosis in testing normality and robustness studies. *Sankhyā: The Indian Journal of Statistics, Series B*, pages 115–128.

Marino, R. and Connors, R. (1983). Orthorhombic and monoclinic TNT: a Nitrogen-14 NQR study. *Journal of Molecular Structure*, 111:323–328.

Marino, R. A. and Klainer, S. M. (1977). Multiple spin echoes in pure quadrupole resonance. *Journal of Chemical Physics*, 67(7):3388–3389.

Marshall, I., Higinbotham, J., Bruce, S., and Freise, A. (1997). Use of voigt lineshape for quantification of in vivo 1H spectra. *Magnetic Resonance in Medicine*, 37(5):651–657.

Martino, R., Malet-Martino, M., Gilard, V., and Balayssac, S. (2010). Counterfeit drugs: analytical techniques for their identification. *Analytical and Bioanalytical Chemistry*, 398(1):77–92.

Maurin, J. K., Pluciński, F., Mazurek, A. P., and Fijałek, Z. (2007). The usefulness of simple X-ray powder diffraction analysis for counterfeit controlthe Viagra® example. *Journal of Pharmaceutical and Biomedical Analysis*, 43(4):1514–1518.

Mayers, A. (2013). *Introduction to Statistics and SPSS in Psychology*. Pearson Education: Upper Saddle River, NJ, 1 edition.

Mefed, A. E. (2015). On the characteristics of 14N NQR in explosives containing random electronic paramagnetic impurities. *Applied Magnetic Resonance*, 46(3):261–279.

Mehring, M. (2012). *Principles of high resolution NMR in solids*. Springer Science & Business Media.

Meiboom, S. and Gill, D. (1958). Modified spin-echo method for measuring nuclear relaxation times. *Review of Scientific Instruments*, 29(8):688–691.

Melexis (2014). Mlx90614. `http://www.melexis.com`. (accessed August 4, 2015).

Meriles, C. (2001). Revision of spin echoes in pure nuclear quadrupole resonance. *Journal of Magnetic Resonance*, 149(2):188–195.

Mikhaltsevitch, V., Rudakov, T., Flexman, J., Hayes, P., and Chisholm, W. (2004a). Multipulse sequences for explosives detection by NQR under conditions of magnetoacoustic and piezoelectric ringing. *Applied Magnetic Resonance*, 25(3-4):449–465.

Mikhaltsevitch, V. T. and Rudakov, T. N. (2004). On the NQR detection of nitrogenated substances by multi-pulse sequences. *Physica Status Solidi (b)*, 241(2):411–419.

Mikhaltsevitch, V. T., Rudakov, T. N., Chisholm, W. P., Flexman, J. H., and Hayes, P. A. (2007). Probe coil for detecting NQR responsive materials in large volumes. US Patent 7,250,763.

Mikhaltsevitch, V. T., Rudakov, T. N., Flexman, J. H., Hayes, P. A., and Chisholm, W. P. (2004b). Comparative experimental analysis of composite pulses in 14N NQR. *Solid State Nuclear Magnetic Resonance*, 25(1):61–63.

Miller, J. B. (2007). Nuclear quadrupole resonance detection of explosives. *Counterterrorist Detection Techniques of Explosives*.

Miller, J. B. (2011). Nuclear quadrupole resonance detection of explosives: an overview. In *SPIE Defense, Security, and Sensing*, pages 801715–801715.

Miller, J. B. and Barrall, G. A. (2005). Explosives detection with nuclear quadrupole resonance - an emerging technology will help to uncover land mines and terrorist bombs. *American Scientist*, 93(1):50–57.

Miller, J. B., Sauer, K. L., Klug, C. A., and Buess, M. L. (2009). Efficient excitation and ringing suppression in nuclear quadrupole resonance. In *Explosives*

Detection Using Magnetic and Nuclear Resonance Techniques, pages 57–71. Springer.

Mozzhukhin, G., Rameev, B., Khusnutdinov, R., Doğan, N., and Aktas, B. (2012). Three-frequency composite multipulse nuclear quadrupole resonance technique for explosive detection. *Applied Magnetic Resonance*, 43(4):547–556.

Mozzhukhin, G. V., Efremov, A. V., Bodnya, A. V., and Fedotov, V. V. (2005). A two-spiral flat coil for detecting 14N NQR signals. *Russian Physics Journal*, 48(9):978–983.

Mozzhukhin, G. V., Rameev, B. Z., Doğan, N., and Aktaş, B. (2008). Secondary signals in two-frequency nuclear quadrupole resonance on 14N nuclei with I= 1. *Journal of Magnetic Resonance*, 193(1):49–53.

NABP (2011). Issues rogue online pharmacy public health alert. `http://www.nabp.net/news/nabp-issues-rogue-online-pharmacy-public-health-alert/`. (accessed August 25, 2015).

Nayyar, G. M., Breman, J. G., Newton, P. N., and Herrington, J. (2012a). Poor-quality antimalarial drugs in southeast asia and sub-saharan africa. *The Lancet Infectious Diseases*, 12(6):488–496.

Nayyar, G. M. L., Attaran, A., Clark, J. P., Culzoni, M. J., Fernandez, F. M., Herrington, J. E., Kendall, M., Newton, P. N., and Breman, J. G. (2015). Responding to the pandemic of falsified medicines. *American Journal of Tropical Medicine and Hygiene*, pages 14–0393.

Nayyar, G. M. L., Breman, J. G., Newton, P. N., and Herrington, J. (2012b). Poor-quality antimalarial drugs in southeast Asia and sub-saharan Africa. *Lancet Infectious Diseases*, 12(6):488–496.

Neuberger, S. and Neusüß, C. (2015). Determination of counterfeit medicines by Raman spectroscopy: Systematic study based on a large set of model tablets. *Journal of Pharmaceutical and Biomedical Analysis*, 112:70–78.

Newton, P. N., Green, M. D., and Fernández, F. M. (2010). Impact of poor-quality medicines in the "developing" world. *Trends in Pharmacological Sciences*, 31(3):99–101.

Newton, P. N., Green, M. D., Fernández, F. M., Day, N. P., and White, N. J. (2006). Counterfeit anti-infective drugs. *Lancet Infectious Diseases*, 6(9):602–613.

Newton, P. N., Green, M. D., Mildenhall, D. C., Plançon, A., Nettey, H., Nyadong, L., Hostetler, D. M., Swamidoss, I., Harris, G. A., Powell, K., Timmermans, A. E., Amin, A. A., Opuni, S. K., Barbereau, S., Faurant, C., Soong, R. C., Faure, K., Thevanayagam, J., Fernandes, P., Kaur, H., Angus, B., Stepniewska, K., Guerin, P. J., and M, F. F. (2011). Poor quality vital anti-malarials in Africa-an urgent neglected public health priority. *Malaria Journal*, 10:352.

NHS (2015). Metformin hydrochloride (metformin 500 mg tablets). `http://www.nhs.uk/medicine-guides/pages/MedicineOverview.aspx?condition=Diabetes&medicine=metformin%20hydrochloride&preparationMetformin%20500mg%20tablets`. (accessed June 29, 2015).

Osokin, D. Y. (1982). Coherent multipulse sequences in nitrogen-14 NQR. *Journal of Molecular Structure*, 83:243–252.

Osokin, D. Y. (1983). Spin-lattice relaxation of quasi-steady states in nitrogen-14 NQR multipulse experiments. *Molecular Physics*, 48(2):283–291.

Pati, R., Das, T. P., Sahoo, N., and Ray, S. N. (1998). Theory of electronic structure and nuclear quadrupole interactions in heroin. *The Journal of Physical Chemistry A*, 102(18):3209–3214.

Pencheon, D. (2012). Bbc news: Are you willing to swallow a recycled pill? `http://www.bbc.co.uk/news/health-17219584`. (accessed May 19, 2015).

Perez, S. C., Cerioni, L., Wolfenson, A. E., Faudone, S., and Cuffini, S. L. (2005). Utilization of pure nuclear quadrupole resonance spectroscopy for the study of pharmaceutical crystal forms. *International Journal of Pharmaceutics*, 298(1):143–152.

Peshkovsky, A. S., Forguez, J., Cerioni, L., and Pusiol, D. J. (2005). RF probe recovery time reduction with a novel active ringing suppression circuit. *Journal of Magnetic Resonance*, 177(1):67–73.

Petersen, G. and Bray, P. J. (1976). 14N nuclear quadrupole resonance and relaxation measurements of sodium nitrite. *Journal of Chemical Physics*, 64(2):522–530.

Prescott, D. (2010). *Nuclear Quadrupole Spin Dynamics: How Weak RF Pulses and Double Resonance Cross-Relaxation Contribute to Explosives Detection.* PhD thesis, George Mason University.

Prescott, D. W., Malone, M. W., Douglass, S. P., and Sauer, K. L. (2012). Rabi and larmor nuclear quadrupole double resonance of spin-1 nuclei. *Journal of Chemical Physics*, 137(21):214201.

Prescott, D. W., Miller, J. B., Tourigny, C., and Sauer, K. L. (2008). Nuclear quadrupole resonance single-pulse echoes. *Journal of Magnetic Resonance*, 194(1):1–7.

PSI (2014). The counterfeit medicines challenge. `http://www.psi-inc.org/incidentTrends.cfm`. (accessed July 6, 2014).

Rabbani, S. R., Caticha, N., Dos Santos, J. G., and Pusiol, D. J. (1995). Pulsed nuclear-quadrupole resonance in nonuniformly disordered systems. *Physical Review B*, 51(14):8848.

Ramamoorthy, A., Chandrakumar, N., Dubey, A. K., and Narasimhan, P. T. (1993). Analysis of the performance of NQR composite pulses. *Journal of Magnetic Resonance, Series A*, 102(3):274–286.

Ramu, L., Ramesh, K. P., Ramananda, D., and Chandramani, R. (2010). Temperature-and pressure-dependent study of 35Cl NQR frequency and spin lattice relaxation time in 2, 3-dichloroanisole. *Magnetic Resonance in Chemistry*, 48(8):593–599.

Rodionova, O. Y. and Pomerantsev, A. L. (2010). NIR-based approach to counterfeit-drug detection. *Trends Analytical Chemistry*, 29(8):795–803.

Rowe, M. D. and Smith, J. A. S. (1996). Mine detection by nuclear quadrupole resonance. In *The Detection of Abandoned Land Mines: A Humanitarian Imperative Seeking a Technical Solution, EUREL International Conference (Conf. Publ. No. 431)*, pages 62–66. IET.

Rudakov, T. N. (2012). Some aspects of the effective detection of ammonium nitrate-based explosives by pulsed NQR method. *Applied Magnetic Resonance*, 43(4):557–566.

Rudakov, T. N. (2014). Further improvement of NQR technique for detection of illicit substances. In *Magnetic Resonance Detection of Explosives and Illicit Materials*, pages 3–17. Springer.

Rudakov, T. N. and Belyakov, A. V. (1998). Modifications of the steady-state free-precession sequence for the detection of pure nuclear quadrupole resonance. *Journal of Physics D: Applied Physics*, 31(10):1251.

Rudakov, T. N. and Mikhaltsevich, V. T. (2003). Multiple NQR spin echoes in phase cycled pulse experiments. *Physics Letters A*, 309(5):465–469.

Rudakov, T. N., Mikhaltsevich, V. T., and Selchikhin, O. P. (1997). The use of multi-pulse nuclear quadrupole resonance techniques for the detection of explosives containing RDX. *Journal of Physics D: Applied Physics*, 30(9):1377.

Rudberg, T. and Jakobsson, A. (2011). Robust detection of nuclear quadrupole resonance signals in a non-shielded environment. In *Signal Processing Conference, 2011 19th European*, pages 2079–2083. IEEE.

Sacré, P. Y., Deconinck, E., De Beer, T., Courselle, P., Vancauwenberghe, R., Chiap, P., Crommen, J., and De Beer, J. O. (2010). Comparison and combination of spectroscopic techniques for the detection of counterfeit medicines. *Journal of pharmaceutical and biomedical analysis*, 53(3):445–453.

Sauer, K. L. and Klug, C. A. (2006). Spin dynamics in the pulsed spin locking of nuclear quadrupole resonance. *Physical review B*, 74(17):174410.

Sauer, K. L., Suits, B. H., Garroway, A. N., and Miller, J. B. (2001). Three-frequency nuclear quadrupole resonance of spin-1 nuclei. *Chemical Physics Letters*, 342(3):362–368.

Selcuk, K., Dincer, G., and Zararsiz, G. (2015). MVN: An R package for assessing multivariate normality. `http://cran.r-project.org/web/packages/MVN/vignettes/MVN.pdf`. (accessed November 10, 2014).

Seliger, J., Žagar, V., Blinc, R., and Milia, F. (2005). Temperature dependence of 17O and14N NQR frequencies in commercial TNT. *Applied Magnetic Resonance*, 29(4):541–548.

Seliger, J., Žagar, V., and Latosińska, J. N. (2010). 14N NQR, 1H NMR and DFT/QTAIM study of hydrogen bonding and polymorphism in selected solid 1, 3, 4-thiadiazole derivatives. *Physical Chemistry Chemical Physics*, 12(40):13007–13019.

Shapiro, S. S. and Wilk, M. B. (1965). An analysis of variance test for normality (complete samples). *Biometrika*, pages 591–611.

Shinohara, J., Kobayashi, K., Sato-Akaba, H., and Itozaki, H. (2011). Nuclear quadrupole resonance of norephedrine. *Solid State Nuclear Magnetic Resonance*, 40(3):121–125.

Shinohara, J., Sato-Akaba, H., and Itozaki, H. (2012a). Nuclear quadrupole resonance of methamphetamine hydrochloride. *Solid State Nuclear Magnetic Resonance*, 43:27–31.

Shinohara, J., Sato-Akaba, H., and Itozaki, H. (2012b). Simulation of nuclear quadrupole resonance for sensor probe optimization. *Solid State Nuclear Magnetic Resonance*, 43:22–26.

Slichter, C. P. (2013). *Principles of magnetic resonance*, volume 1. Springer Science & Business Media.

Smith, J. A. S. (1971). Nuclear quadrupole resonance spectroscopy; general principles. *Journal of Chemical Education*, 48(1):39–48.

Smith, J. A. S. (1986). Nuclear quadrupole interactions in solids. *Chemical Society Reviews*, 15(2):225–260.

Smith, J. A. S. (1995). Nitrogen-14 quadrupole resonance detection of RDX and HMX based explosives.

Smith, J. A. S., Blanz, M., Rayner, T. J., Rowe, M. D., Bedford, S., and Althoefer, K. (2011). 14N quadrupole resonance and 1H T1 dispersion in the explosive RDX. *Journal of Magnetic Resonance*, 213(1):98–106.

Smith, J. A. S., Rowe, M. D., Deas, R. M., and Gaskell, M. J. (2003). Nuclear quadrupole resonance detection of landmines. In *Conference Requirements and Technologies for the Detection, Removal and Neutralization of Landmines and UXO*, volume 2, pages 715–721.

Somasundaram, S. D. (2007). *Advanced signal processing algorithms based on novel nuclear quadrupole resonance models for the detection of explosives*. PhD thesis, King's College London.

Somasundaram, S. D., Jakobsson, A., and Butt, N. R. (2009). Countering radio frequency interference in single-sensor quadrupole resonance. *IEEE Geoscience and Remote Sensing Letters*, 6(1):62–66.

Somasundaram, S. D., Jakobsson, A., and Gudmundson, E. (2008a). Robust nuclear quadrupole resonance signal detection allowing for amplitude uncertainties. *IEEE Trans. Signal Processing*, 56(3):887–894.

Somasundaram, S. D., Jakobsson, A., Rowe, M. D., Smith, J. A., Butt, N. R., and Althoefer, K. (2008b). Detecting stochastic nuclear quadrupole resonance signals in the presence of strong radio frequency interference. In *Acoustics, Speech and Signal Processing, 2008. ICASSP 2008. IEEE International Conference on*, pages 3645–3648. IEEE.

Somasundaram, S. D., Jakobsson, A., Rowe, M. D., Smith, J. A. S., Butt, N. R., and Althoefer, K. (2008c). Robust detection of stochastic nuclear quadrupole resonance signals. *IEEE Trans. Signal Processing*, 56(9):4221–4229.

Somasundaram, S. D., Jakobsson, A., and Smith, J. A. S. (2008d). Analysis of nuclear quadrupole resonance signals from mixtures. *Signal processing*, 88(1):146–157.

Somasundaram, S. D., Jakobsson, A., Smith, J. A. S., and Althoefer, K. (2007). Exploiting spin echo decay in the detection of nuclear quadrupole resonance signals. *IEEE Trans. Geoscience and Remote Sensing*, 45(4):925–933.

Song, S. K., Kim, B. S., Noh, T. H., Park, Y. M., Jeon, I., Seo, Y. M., and Kang, K. H. (2000). NQR lineshape study of the local properties of disorder in solids.

Stoica, P. and Moses, R. L. (2005). *Spectral analysis of signals*. Pearson/Prentice Hall Upper Saddle River, NJ.

Stoica, P. and Sundin, T. (2001). Nonparametric NMR spectroscopy. *Journal of Magnetic Resonance*, 152(1):57–69.

Stoica, P., Xiong, H., Xu, L., and Li, J. (2007). Adaptive beamforming for quadrupole resonance. *Digital Signal Processing*, 17(3):634–651.

Suits, B. H. (2004). The noise immunity of gradiometer coils for14N NQR land mine detection: Practical limitations. *Applied Magnetic Resonance*, 25(3-4):371–382.

Suits, B. H. (2006). Nuclear quadrupole resonance spectroscopy. In *Handbook of Applied Solid State Spectroscopy*, pages 65–96. Springer.

Suryanarayana, C. and Norton, M. G. (2013). *X-ray diffraction: a practical approach*. Springer Science & Business Media.

Tachiki, M., He, D. F., and Itozaki, H. (2007). Sensing of chemical substances using SQUID-based nuclear quadrupole resonance. *Physica C: Superconductivity*, 463:1034–1037.

Tan, Y., Tantum, S. L., and Collins, L. M. (2004). Cramer-Rao lower bound for estimating quadrupole resonance signals in non-Gaussian noise. *IEEE Signal Processing Letters*, 11(5):490–493.

Tan, Y., Tantum, S. L., and Collins, L. M. (2005). Kalman filtering for enhanced landmine detection using quadrupole resonance. *IEEE Trans. Geoscience and Remote Sensing*, 43(7):1507–1516.

Tantum, S. L., Collins, L. M., Carin, L., Gorodnitsky, I., Hibbs, A. D., Walsh, D. O., Barrall, G. A., Gregory, D. M., Matthews, R., and Vierkotter, S. A. (1999). Signal processing for NQR discrimination of buried landmines. volume 3710, pages 474–482.

Tate, E., Althoefer, K., Barras, J., Rowe, M. D., Smith, J. A. S., Pearce, G. E. S., and Wren, S. A. C. (2009). Quantitative 35Cl nuclear quadrupole resonance in tablets of the antidiabetic medicine diabinese. *Analytical Chemistry*, 81(13):5574–5576.

Tate, E. A. K. (2007). *The application of nuclear quadrupole resonance to pharmaceutical analysis*. PhD thesis, King's College London.

The R foundation (2016). The r project for statistical computing. `https://www.r-project.org`. (accessed April 15, 2016).

Topa, H. (2011). Detection of counterfeit medicines. Master's thesis, Lund University.

Tukey, J. W. (1949). Comparing individual means in the analysis of variance. *Biometrics*, pages 99–114.

UN (2013). Translational organized crime in west Africa: a threat assessment. `https://www.unodc.org/documents/data-and-analysis/tocta/West_Africa_TOCTA_2013_EN.pdf`. (accessed August 25, 2015).

Wertheimer, A. I. and Norris, J. (2009). Safeguarding against substandard/counterfeit drugs: mitigating a macroeconomic pandemic. *Research in Social and Administrative Pharmacy*, 5(1):4–16.

WHO (2012). Medicines: spurious/falsely-labelled/falsified/counterfeit (SFFC) medicines. `http://www.who.int/mediacentre/factsheets/fs275/en/`. (accessed July 6, 2014).

WHO (2015). Model list of essential medicines. `http://www.who.int/selection_medicines/committees/expert/20/EML_2015_FINAL_amended_AUG2015.pdf?ua=1`. (accessed September 10, 2015).

Woessner, D. E. and Gutowsky, H. S. (1963). Nuclear pure quadrupole relaxation and its temperature dependence in solids. *Journal of Chemical Physics*, 39(2):440–456.

Yesinowski, J. P., Buess, M. L., Garroway, A. N., Ziegeweid, M., and Pines, A. (1995). Detection of 14N and 35Cl in cocaine base and hydrochloride using NQR, NMR, and SQUID techniques. *Analytical Chemistry*, 67(13):2256–2263.

Youlin, X. and Chahohui, Y. (1996). NQR spectroscopy of powder sample with I= 1 and 3/2 (I). *Prog. Natural Sci.*, 6:284–292.

Zhang, X., Schemm, N., Balkir, S., and Hoffman, M. W. (2014). A low-power compact NQR based explosive detection system. *Sensors Journal, IEEE*, 14(2):497–507.

Appendix A

Cramér-Rao Lower Bound

The Cramér-Rao Lower Bound (CRLB) is a lower bound on the covariance matrix of the estimated parameters [Kay, 1993]. The bound states that the variance of any unbiased estimator will satisfy the condition

$$\mathrm{cov}\{\hat{\boldsymbol{\theta}}\} \geq \mathbf{C}_{\mathrm{CRB}}(\boldsymbol{\theta}), \tag{A.1}$$

where the CRLB equals the inverse of the Fisher Information Matrix (FIM),

$$\mathbf{C}_{\mathrm{CRB}}(\boldsymbol{\theta}) = \mathbf{F}^{-1}(\boldsymbol{\theta}), \tag{A.2}$$

with $\mathbf{F}^{-1} \geq 0$ denoting the positive semi-definite FIM, for j:th and i:th matrix elements, derived from the formula in A.3, where the likelihood function is given by $f_{\mathbf{x}}(\mathbf{x};\boldsymbol{\theta})$.

$$\begin{aligned}[\mathbf{F}]_{j,i} &= -E\left\{\frac{\partial^2 \ln f_{\mathbf{x}}(\mathbf{x};\boldsymbol{\theta})}{\partial \boldsymbol{\theta_j} \partial \boldsymbol{\theta_i}}\right\} \\ &= E\left\{\frac{\partial \ln f_{\mathbf{x}}(\mathbf{x};\boldsymbol{\theta})}{\partial \boldsymbol{\theta_j}}\right\}\left\{\frac{\partial \ln f_{\mathbf{x}}(\mathbf{x};\boldsymbol{\theta})}{\partial \boldsymbol{\theta_i}}\right\}. \end{aligned} \tag{A.3}$$

Any unbiased estimator that attains the CRLB, or even achieves the lowest possible variance for all the values of the unknown parameters – i.e. being the minimum variance unbiased (MVU) estimator – is said to be statistically efficient. In practice, this outcome is crucially important as it allows one to determine how optimally the estimator performs. It should be noted that a lower bound may not be achieved, implying that no unbiased estimator exists to meet this condition and it is therefore not statistically efficient [Kay, 1993].

For the case where an unknown parameter is a function of another fundamental parameter, i.e. $\boldsymbol{\rho} = \mathbf{g}(\boldsymbol{\theta})$, with $g(\cdot)$ being a function with dimension l, then the variance of the parameter $\boldsymbol{\rho}$ is derived as [Kay, 1993]

$$\mathbf{V}(\boldsymbol{\rho}) \geq \frac{\partial \mathbf{g}(\boldsymbol{\theta})}{\partial \boldsymbol{\theta}} \mathbf{F}^{-1} \frac{\partial \mathbf{g}(\boldsymbol{\theta})}{\partial \boldsymbol{\theta}}^{T}, \tag{A.4}$$

where the Jacobian matrix of size $l \times m$ is given by

$$\frac{\partial \mathbf{g}(\boldsymbol{\theta})}{\partial \boldsymbol{\theta}} = \begin{pmatrix} \frac{\partial \mathbf{g}_1(\boldsymbol{\theta})}{\partial \boldsymbol{\theta}_1} & \frac{\partial \mathbf{g}_1(\boldsymbol{\theta})}{\partial \boldsymbol{\theta}_2} & \cdots & \frac{\partial \mathbf{g}_1(\boldsymbol{\theta})}{\partial \boldsymbol{\theta}_m} \\ \frac{\partial \mathbf{g}_2(\boldsymbol{\theta})}{\partial \boldsymbol{\theta}_1} & \frac{\partial \mathbf{g}_2(\boldsymbol{\theta})}{\partial \boldsymbol{\theta}_2} & \cdots & \frac{\partial \mathbf{g}_2(\boldsymbol{\theta})}{\partial \boldsymbol{\theta}_m} \\ \vdots & \vdots & \ddots & \vdots \\ \frac{\partial \mathbf{g}_l(\boldsymbol{\theta})}{\partial \boldsymbol{\theta}_1} & \frac{\partial \mathbf{g}_l(\boldsymbol{\theta})}{\partial \boldsymbol{\theta}_2} & \cdots & \frac{\partial \mathbf{g}_l(\boldsymbol{\theta})}{\partial \boldsymbol{\theta}_m} \end{pmatrix}. \tag{A.5}$$

Typically, statistical efficiency is achieved for linear transformations, i.e., $\boldsymbol{\rho} = \mathbf{g}(\boldsymbol{\theta}) = \mathbf{A}\boldsymbol{\theta} + \boldsymbol{\beta}$, where $\mathbf{A}$ is a $l \times m$ matrix and $\boldsymbol{\beta}$ is a $l \times 1$ vector.

Furthermore, for a normally distributed signal, $N(\mathbf{x}_{\boldsymbol{\theta}}, \sigma^2)$, one may use the Slepian-Bangs formula [Stoica and Moses, 2005; Gudmundson et al., 2012; Kay, 1993] to simplify the notation of the CRLB, being expressed as

$$\mathbf{C}_{\mathrm{CRB}}(\boldsymbol{\theta}) = \frac{\sigma^2}{2} \left[\mathrm{Re} \left\{ \left(\frac{\partial \mathbf{x}_{\boldsymbol{\theta}}}{\partial \boldsymbol{\theta}} \right)^{H} \left(\frac{\partial \mathbf{x}_{\boldsymbol{\theta}}}{\partial \boldsymbol{\theta}} \right) \right\} \right]^{-1}. \tag{A.6}$$

Appendix B

Multivariate analysis of variance

Analysis of variance (ANOVA) is a statistical technique that is used to test the heterogeneity among group means. In ANOVA, one aims to determine the effect of an independent (categorical) variable on one dependent variable. The independent variable forms the groups of observations. Multivariate analysis of variance (MANOVA) extends ANOVA to cases where there are two or more dependent variables. The purpose of MANOVA is to investigate the effect of the independent variable(s) upon the combined dependent variables and also on each of the dependent variables separately. As opposed to using a set of ANOVAs, one for each dependent variable, MANOVA provides a methodology that also accounts for the correlations between these variables, resulting in reduction of Type-I error. Given that ANOVA lies at the core of MANOVA, this appendix explicitly illustrates the ANOVA methodology.

ANOVA proceeds by separating the variability of the sample into two groups: the *within-group* variability and the *between-group* variability. The within-group sum of squares describes the variability of the observations with regards to their group means. This is expressed as

$$SS_E = \sum_{i=1}^{k} \sum_{j=1}^{n_i} (x_{ij} - \bar{x}_i)^2 \,, \tag{B.1}$$

where $\bar{x}_i$ and n_i denote the sample mean and number of observations in the i^{th} group, respectively. Moreover, x_{ij} denotes the j^{th} observation of group i and k is the total number of groups. The between-group sum of squares evaluates the

variability of each group mean from the overall mean, and this is given by

$$SS_B = \sum_{i=1}^{k} n_i \left(\bar{x}_i - \bar{x}\right)^2, \tag{B.2}$$

where $\bar{x} = \frac{1}{n}\sum_{ij} x_{ij}$ is the total mean of all observations irrespective of groups, with n denoting the total number of observations. By summing B.1 and B.2, the total amount of variability can be expressed as

$$\begin{aligned} SS_T &= SS_E + SS_B \\ &= \sum_{i=1}^{k}\sum_{j=1}^{n_i} \left(x_{ij} - \bar{x}\right)^2. \end{aligned} \tag{B.3}$$

The sums of squares are divided by their respective degrees of freedom to obtain the mean sums of squares, namely

$$MS_B = \frac{SS_B}{df_B} \tag{B.4}$$

and

$$MS_E = \frac{SS_E}{df_E}. \tag{B.5}$$

where the degrees of freedom are given by $df_B = k - 1$ and $df_E = n - k$. One can set up a hypothesis test by computing the ratio $\frac{MS_B}{MS_E}$, which is referred to as the *F-ratio*. Under the null hypothesis ($H_0 : \bar{x}_1 = \bar{x}_2 = \cdots = \bar{x}_k$), the F statistic follows an F-distribution with $k - 1$ and $n - k$ degrees of freedom. Given a significance level α, the F statistic is compared against the corresponding critical value, C, from the F table [Mayers, 2013].The null hypothesis is rejected when the F-ratio is greater than C. The result from ANOVA can either be expressed in terms of the F-ratio or its corresponding *p-value*.

MANOVA is a more complicated design than ANOVA and therefore, identifying which independent variable affects each of the dependent variables might not be straightforward. Consequently, there are some assumptions that need to be imposed. These are:

- Normality: the dependent variable should be normally distributed within the groups. Relevant tests include the Kormogorov-Smirnov [Lilliefors,

1967], Shapiro-Wilk [Shapiro and Wilk, 1965] and Anderson-Darling [Anderson and Darling, 1954] tests.

- Multivariate normality: the combination of dependent variables should follow a normal distribution. One could apply the Mardia's [Mardia, 1974] and Henze-Zirkler's tests [Henze and Zirkler, 1990].

- Homogeneity of variances: the dependent variables exhibit similar levels of variance across the groups. Levene's test is used to test this assumption [Levene, 1960].

- Homogeneity of variance-covariance: the covariances of the dependent variables are homogeneous across the groups. Box'm test is most commonly used to test this assumption [Box, 1949; Mayers, 2013].

- Moderate correlation: there should be moderate correlation between the dependent variables. Pearson's correlation can be applied to test the level of correlation [Johnson et al., 1992].

In the case where the group sizes are unequal, violations in these assumptions are particularly important. Moreover, one should check for outliers, as they may influence the significance of the statistical outcomes.

Similar to the F-ratio in ANOVA, Wilks' lambda is used in MANOVA and it directly measures the proportion of variance in the combination of the dependent variables that is accounted for by the independent variable. Under some adjustment, Wilks' lambda statistic can be transformed to a statistic which has approximately an F distribution. Wilks' lambda is commonly used when the independent variable consists of more than two groups. Alternative similar statistics can be used in MANOVA, such as the Pillai's trace, Hotelling's trace and Roy's largest root [Johnson et al., 1992]. One may select a statistic based on several factors. For instance, Pillai's trace can be used with any number of groups within the independent variable but it is also less advantageous when the assumption of homogeneity of variances is violated and unequal group sizes exist [Mayers, 2013]. On the other hand, Hotelling's trace is applied when only two groups constitute the independent variable. Roy's largest root shares similarities with Pillai's trace, but mainly focuses only on the first independent variable [Mayers, 2013]. Therefore, the choice of the test strongly relies on the MANOVA design.

Appendix C

Introduction to powder X-ray diffraction

Powder X-ray diffraction (XRD) is an analytical technique used to characterise crystalline phases and provide information on the atomic packing within the material [Suryanarayana and Norton, 2013]. This technique has been proven suitable for pharmaceutical applications, especially in quantification of polymorphic mixtures [Croker et al., 2012; Newton et al., 2011]. XRD is based on constructive interference as scattered X-rays are emitted by atoms in the crystalline sample. Generally, diffraction occurs when a beam of X-rays illuminates a material with periodic arrangement of atoms, which then scatters radiation coherently, producing constructive interference at specific angles. This interaction occurs when the Bragg's law is satisfied, i.e., when

$$2d \sin \theta = \lambda. \tag{C.1}$$

The condition relates the wavelength, λ, of the oscillating electric field of the X-ray beam to the angle of incident, θ, and the interplanar spacing, d, in the crystalline material [Suryanarayana and Norton, 2013]. Figure C.1 is a simple illustration the geometry of this effect. The result of this constructive interference is a characteristic diffraction pattern with many distinct peaks which are related to the interplanar spaces of atoms in the material. Normally, in order to assess any differences in the composition of a pharmaceutical tablet, its diffraction pattern is compared with a reference/original one [Holzgrabe and Malet-Martino, 2011]. Even though the diffraction spectrum is less detailed as compared with that

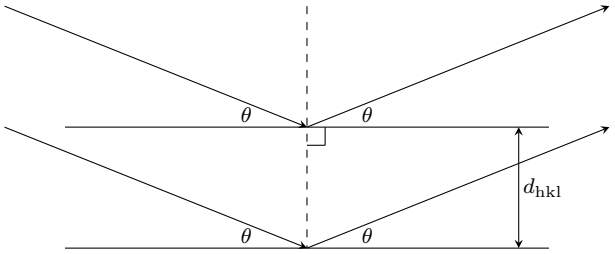

Figure C.1: Simple diagram of the constructive interference of an X-ray scattered from two planes.

from single crystals, Bragg diffractions are possible in polycrystalline substances, which are commonly used in the characterisation of crystalline structures. The planes in the crystal lattice are identified by the Miller indices (hkl), and the plane separation d_{hkl} determines the angles, $2\theta_{\mathrm{hkl}}$, at which diffraction occurs according to Bragg's law [Suryanarayana and Norton, 2013]; i.e., the positions of the diffraction peaks depend on the arrangement of the unit cell. Moreover, the relative intensities of those peaks depend on the distribution of the scattering matter. Thus, a diffraction pattern is created by plotting the relative intensities with respect to the diffraction angles, 2θ.

A typical X-ray diffractometer consists of three essential components: a source of X-rays (i.e., X-ray tube), a detector and sample holder equipment [Suryanarayana and Norton, 2013]. The X-ray tube produces a beam of electrons by heating a filament cathode, and the beam is then accelerated towards a metal anode. A small percentage of the electrons is converted to X-rays, while the energy of the rest is dissipated as heat in the anode. The X-rays are then directed on the sample, and diffraction spectra are obtained. The generated X-rays have a specific wavelength that depends on the target material; a common material is copper (Cu) with $\lambda = 0.15418$ Å[Suryanarayana and Norton, 2013]. In most powder XRD studies, a monochromatic beam of X-rays is used, generally obtained using appropriate filters that allow absorption of rays with K_α (consists of K_{α_1} and K_{α_2}) and K_β components; these components correspond to the filling of the innermost K shell of the Bohr model of the atom [Suryanarayana and Norton, 2013]. Furthermore, slits may be used to collimate the incident and scattered beam in order to obtain better resolution intensities and well-defined diffraction angles. The axial divergence of the beams is controlled with the use of Soller slits which are parallel copper plates [Suryanarayana and Norton, 2013]. A typical geometry is the Bragg-Brentano θ/θ reflection geometry, in which the X-ray tube

is kept stationary, while the material under study and the detector rotates by the angle θ° and $2\theta^{\circ}$, respectively. By scanning the material over a range of diffraction angles, 2θ (angle between the incident beam and detector), the characteristic diffraction pattern is then obtained from the spectra of the 2θ versus intensity. For powder XRD, little sample preparation is required. The material should be finely ground into powder form before placed in the sample holder.